HEINRICH HEINE
UNIVERSITÄT DÜSSELDORF

Amplification of ultra-short relativistic laser pulses by stimulated Brillouin scattering

Inaugural-Dissertation

zur Erlangung des Doktorgrades der
Mathematisch-Naturwissenschaftlichen Fakultät der
Heinrich-Heine-Universität Düsseldorf

vorgelegt von

Friedrich Schluck

geboren am 6. April 1990 in Leverkusen

Düsseldorf, den 20. Dezember 2016

aus dem Institut für Theoretische Physik I
der Heinrich-Heine-Universität Düsseldorf

Gedruckt mit der Genehmigung der
Mathematisch-Naturwissenschaftlichen Fakultät der
Heinrich-Heine-Universität Düsseldorf

Referent:
Prof. Dr. Dr. Carsten MÜLLER
Korreferent:
Prof. Dr. Alexander PUKHOV

Tag der mündlichen Prüfung:
10. Februar 2017

Zusammenfassung

Ultrakurze und ultraintensive Laserpulse finden Anwendung in vielen verschiedenen Feldern. Man kann sie zum Beispiel zur Teilchenbeschleunigung beziehungsweise zur Erzeugung sekundärer Strahlung benutzen. Die Anwendungen reichen von Laserwakefieldbeschleunigung für medizinische Verwendung bis zur Erzeugung hoher Harmonischer, Attosekundenpulse und Terahertzstrahlung. Zudem können mit solchen Pulsen ultrarelativistische beziehungsweise quantenelektrodynamische Effekte im Rahmen der Grundlagenforschung untersucht werden.

Die schnelle Entwicklung in Hochleistungslasern, welche durch die Erfindung der *Chirped Pulse Amplification* ausgelöst wurde, erreicht heute ihre Grenzen. Optische Komponenten wie Gitter und Kristalle sind im Zuge der Laserverstärkung der hochenergetischen Strahlung ausgesetzt und nah an ihrem Zerstörungslimit. Um diese Beschränkung zu überwinden ist es vorgesehen, Plasma als Verstärkermedium zu nutzen.

Der Ansatz dieser Forschung ist es, Plasmawellen als Energieüberträger zwischen zwei Laserpulsen zu benutzen. Der typischerweise lange, hochenergetische Pumppuls soll an einer solchen Plasmawelle in einen typischerweise kurzen, niederenergetischen Seedpuls streuen, wobei dieser Puls in seiner Dauer möglichst kurz bleiben soll. Die Plasmawelle kann entweder eine hochfrequente Langmuir- oder eine niederfrequente ionenakustische Oszillation sein. Im ersten Fall spricht man von Raman-Streuung, im zweiten von Brillouin-Streuung.

Insbesondere das sogenannte *strong coupling regime* hat in den letzten Jahren vermehrt neues Interesse erfahren. Hier ist die Plasmawelle eine getriebene Quasimode des Plasmas mit einer mittelhohen Frequenz. Dieser Streumechanismus besitzt einige Vorteile gegenüber Raman-Verstärkung oder herkömmlicher, *weak coupling* Brillouin-Verstärkung. Die Laserpulse müssen hier nicht gegeneinander in ihrer Frequenz verstimmt werden, der verstärkte Puls ist mit ca. 100 fs Dauer kurz, der Vorgang ist gegenüber Dichteinhomogenitäten im Plasma robust und fast die komplette Energie des Pumppulses kann auf den Seed übertragen werden.

Wir untersuchen die kinetische Dispersionsrelation für weak und strong coupling Brillouinverstärkung für Elektronen-Protonen und Elektronen-Positronen Plasmen und benennen die Limits einer Fluidbeschreibung. Anschließend studieren wir den Übergang zwischen weak und strong coupling und seine Charakteristika anhand eines neuen Dreiwellenmodells. Danach diskutieren wir den Einfluss des Chirps des Pumps auf den verstärkten Seed und die Relevanz in Bezug auf die Effizienz des Energieübertrags. Da die vorliegende Arbeit an der Schnittstelle zwischen Experiment und Theorie entstanden ist, setzen wir zuletzt die Ergebnisse in den Kontext aktueller und zukünftiger Experimente.

Abstract

Ultra-short ultra-intense laser pulses find applications in many different fields. Be it in direct usage, for example as a driver for particle acceleration, or to generate secondary radiation. Possible deployments are laser-wakefield acceleration for medical purposes and the generation of high harmonics, attosecond pulses and terahertz radiation, respectively. Furthermore, ultra-relativistic or quantumelectrodynamic effects can be investigated using these laser pulses in fundamental research.

However, the fast development in available highest peak power triggered by the invention of *Chirped Pulse Amplification* reaches its limits today. During laser amplification, optical components such as gratings and crystals are affected by the highly energetic radiation and one needs to preserve their damageless operation. To overcome the limits given by the destruction threshold of such components, plasma as an amplfication medium is proposed.

The idea is to use plasma waves as an energy transmitter between two laser pulses. The typically long, high energetic pump pulse is intended to scatter off this plasma wave into the typically short, low energetic seed pulse, while the latter ideally stays short in duration. The plasma wave can be either a high frequency Langmuir oscillation or a low frequency ion acoustic wave. The former scattering mechanism is known as Raman scattering and the latter is called Brillouin scattering.

Especially the so-called *strong coupling* regime has received increased interest in recent years. In this process, the plasma wave is a driven quasi-mode of the plasma with average frequency. This scattering mechanism bears many advantages over Raman amplification or *weak coupling* Brillouin amplification. Here, the laser pulses need no detuning, are relatively short ~ 100 fs, it is a scheme robust against density inhomogenities and almost all energy can be transmitted from the pump to the seed pulse.

We study the kinetic dispersion relation for weak and strong coupling Brillouin amplification for electron-proton and electron-positron plasmas and name the limits of the fluid description. In the next step, we investigate the transition from weak to strong coupling and its characteristics with a newly derived three wave interaction model. The influence of the pump chirp on the amplified seed and energy transmission efficiency is discussed subsequently. As this work at hand was done at the junction between experiments and theory we lastly put the analysis made into the context of current and future experiments.

Contents

1 Introduction

Light is an essential ingredient for almost all life known to mankind. Human population on earth's surface would be unimaginable without the sun in the center of our solar system, delivering heat and energy to our planet. And with light comes one of the most fundamental constants of the laws of nature, the speed of light $c = 3 \cdot 10^8$ m/s. This basic concept, first proposed by one of the most ingenious minds physics witnessed so far, Albert Einstein in 1905 [1, 2], opened a whole new field of research and understanding of physics.

Electromagnetic radiation encompasses a wide spectrum of frequencies, of which only the small portion we call *light* is visible to the human eye. Measuring wavelengths, the distance between two consecutive maxima in a wave, analog to water waves, allows us to differentiate within this wide range of electromagnetic radiation. Starting from harmful γ-Rays at $\lambda \approx 10^{-12}$ m over x- or Röntgen-rays at $\lambda \approx 10^{-11} - 10^{-9}$ m to ultraviolet radiation at $\lambda \approx 10^{-8} - 10^{-7}$ m, we finally arrive at the visible spectrum, covering the wavelength range form 400 to 700 nm, i.e. $4 \cdot 10^{-7} - 7 \cdot 10^{-7}$ m. At longer wavelengths, up to $\lambda \approx 1$ mm or 10^{-3} m we find infrared radiation, surpassed by microwaves and radio waves with wavelengths of up to 100 km.

Einstein's explanation of the photoelectric effect earned him the Nobel prize in physics in 1922. His discovery opened the field of quantum mechanics. Although Einstein himself opposed this field for his entire life, it revolutionized physics from the early 20th century onward.

One of the many important impacts his findings had was the subsequent invention of the laser, an acronym standing for ***l**ight **a**mplification by **s**timulated **e**mission of **r**adiation*. The first laser was built by Maiman in 1960 [3], based on the concept presented by Townes and Schawlow [4]. Although introducing the concept in a brief sentence does not do it justice, laser light can essentially be described as extremely coherent, precise and well defined radiation. Today its range of application is both very wide and disparate. Lasers are used in barcode scanners, disk players, printers, surgical instruments, in industrial products for welding and distance measurement, as military applications such as weapons or as a key ingredient of modern fiber-optic communication.

Lasers come in different flavors and types. The first important criterion is the mode of operation. Many of the aforementioned applications require continuous

radiation. However, operating the laser in pulsed intervals allows to deposit its energy in a very confined area over a very short duration. One goal of such ultra-short ultra-intense laser pulses is to accelerate particles, e.g. for non-invasive cancer treatment.

Back in the 1980's, the invention of chirped pulse amplification (CPA) by Strickland and Mourou [5] and its implementation [6] catalyzed rapid development in laser techniques, and consequently resulted in a huge increase in available peak power and a decrease in the shortest possible pulse duration. Today we find petawatt systems, i.e. experimental setups that can shoot laser pulses with 10^{15} W peak power. Two of the most powerful facilities are located in Osaka [7] and at the national ignition facility NIF [8]. For comparison, the whole power consumption of earth's population including fossil fuels is estimated 12.3 TW $= 1.23 \cdot 10^{13}$ W [9], thus only 1% of what is delivered by existing laser schemes. Ambitious projects as ELI beamlines aim at generating even higher peak powers up to 10 PW $= 10^{16}$ W [10], almost 10% of the power radiated on earth by the sun.

For such high power laser radiation there are many possible applications in plasma–light interaction. It can be used directly for laser induced fusion via fast ignition [11] or via wakefield excitation [12] as a driver for particle acceleration [13, 14]. State of the art experiments yielded electron energies of 4 GeV [15] up to 9 GeV [16] and ion energies of up to 160 MeV [17, 18]. A state of the art experiment [19] used laser accelerated electrons for treatment of cancer in mice. For comparison, CERN delivers proton energies in the range of TeV [20]. Another possibility is to use these high power lasers to excite secondary radiation, e.g. high harmonics [21], attosecond (1 as $= 10^{-18}$ s) pulses [22] and radiation in the range of terahertz (1 THz $= 10^{12}$ Hz) [23, 24].

However, today's laser technique is limited by the damage threshold of the optical components such as gratings [25] and crystals [26]. The idea of replacing solid state components by using plasma as the amplification medium occured already decades ago [27, 28, 29, 30, 31], eventually proposing Raman and Brillouin scattering [32, 33] to reach the Exawatt (1 EW $= 10^{18}$ W) or even Zetawatt (1 ZW $= 10^{21}$ W) regime [34, 35, 36].

The fundamental idea is that two counterpropagating lasers, one called *pump* and the other called *seed*, are aligned to overlap when radiated into plasma. Their beat wave is in resonance with a plasma mode, off which photons of the pump scatter in order to become photons of the seed. Typically, the pump is a laser pulse of long duration and of average amplitude, while the seed is a short pulse with low amplitude. Ideally, the latter will stay short but absorb all the energy transmitted by the pump and thus become a short laser pulse with high amplitude after the interaction.

One possible description of the scattering process differentiates between two

6

regimes: The linear phase and the pump depletion regime. In the former, the pump stays unchanged, as only a few photons are lost in the scattering process. Simultaneously, the seed grows exponentially. As soon as both amplitudes reach similar values the process complicates and the growth of the seed is algebraical. In an ideal setup, the pump pulse eventually diminishes and transmits almost its whole energy to the seed, wherefor this regime is called nonlinear or pump depletion regime.

Usually, the diameter of the pulses in this scenario is quite large at approximately 1 mm, in order to avoid unwanted effects such as relativistic self-channeling [37]. As a consequence, the local intensity is quite low. It is substantially below 10^{18} W/cm^2, which allows to disregard relativistic effects, but on the other hand allows laser pulse filamentation to develop faster [38, 39]. Since the radial dimensions are large compared to the longitudinal extent, one-dimensional theory is often sufficient.

For Raman scattering, the basic principles [40, 41] were further developed to propose an amplification setup [32, 33, 42, 43]. The plasma wave, off which photons scatter, is a Langmuir wave, i.e. an electrostatic plasma oscillation, in terms of quanta also referred to as plasmons. Next to simulations, there is also analytic theory available, covering the nonlinear amplification stages with a self-similarity ansatz [44, 45]. Experiments done on Raman amplification [46, 47, 48, 49] emphasize the relevance of theoretical investigations such as kinetic simulations [50, 51], however, the optimal setup remains yet to be found [52, 53].

Brillouin scattering is superficially similar to the Raman case, though very different in its details [41, 54]. The plasma mode governing the amplification is a lower frequency ion acoustic mode, or, in terms of quanta, built up by phonons. As the goal of such an amplification process is to yield short laser pulses, the so called strongly coupled regime was analyzed extensively in recent years [55, 56, 57]. Here, the plasma mode is no longer a resonant mode of the plasma itself, but a quasi-mode, i.e. only resonant in the presence of the lasers. It has a much higher frequency than an ion acoustic wave, though still lower than a Langmuir wave. As the frequency of the plasma mode defines the minimum duration of the amplified laser pulse Δt, we state that for Raman we have $\Delta t \approx 10$ fs (1 fs = 10^{-15} s), for Brillouin $\Delta t \approx 1$ ps (1 ps = 10^{-12} s) and for strongly coupled Brillouin $\Delta t \approx 100$ fs. Especially the investigation of the transition between weak and strong coupling Brillouin scattering delivers deep insights on the amplification process [58] and is discussed in this work.

Although the final duration of the laser pulse may be longer, strong coupling Brillouin amplification bears advantages over Raman. The plasma densities necessary for effective energy transmission range from $n_e = 10^{18} - 10^{20}$ cm^{-3}. Thus, pretty dense plasmas are necessary. In order to fulfill energy and momentum conservation during the scattering process, the two laser pulses used need to be detuned by a substantial amount, roughly 30 nm for 800 nm wavelength, in the case of Raman

scattering. In case of Brillouin scattering, the detuning is negligible due to the lower frequency of the plasma wave. Detuning of the central wavelength of a laser is a feat not easily managed during experiments. Effects concerning the tunability of lasers and how they affect the amplification scheme were discussed previously, e.g. for chirp [59, 53, 38, 60, 61, 62], and are shown in this work. Other advantages of Brillouin amplification over Raman amplification are that the quasi-mode is hardly affected by density inhomogenities [63], rendering strongly coupled Brillouin amplification more robust. Furthermore, the pump depletes almost completely and less energy of the pump is transferred to the density oscillation than when using Raman scattering.

Comparisons between the different processes were made repeatedly [63, 64, 65] and an amplification scheme using both Raman and strongly coupled Brillouin was proposed [66]. It was also shown, that in the relativistic regime, where laser-matter interactions change [67, 68], a unified treatment is necessary [69].

The scattering mechanisms are not limited to electron-proton plasmas, but can be used for multiple ion species, such as, possibly, positron-electron plasmas [70, 71, 72]. Similar as for Raman, it is possible to describe the linear regime with a dispersion relation [41]. Here, one differentiates between a fluid description and a more general kinetic treatment [73], both also discussed in this work. For strong coupling Brillouin, there is also a self-similarity analysis available [55, 50] treating the nonlinear regime analytically, and stressing results obtained by simulations. The first experiments [74, 75, 76] yielded promising results, although the optimal implementation remains challenging [77].

The Brillouin amplification setup is tricky in its implementation, as with plasma density, shape, ion and electron temperature, pump and seed pulse central wavelength, amplitude, shape, duration and time delay between those two, there are many parameters that need to be optimized to make feasible predictions for experiments. The goal of this work was to clear that wide parameter space and find and tackle the reasons, why theory predicts a very high energy transmission efficiency yet unreached in experiments.

The work at hand is structured as follows. In Ch. 2 we name the basics for laser plasma interaction, following explanations given in [37, 41, 78, 79, 80, 81, 82], i.e. introduce Vlasov's equation, Maxwell's equations and a fluid description. We introduce the key equations and parameters describing plasma in Sec. 2.1, ranging from a discussion about ionization in Subsec. 2.1.1 to an analysis of the dispersion of generic plasma waves in Subsec. 2.1.3. We continue with the introduction of Gaussian laser pulses and chirp in Sec. 2.2, whereafter we discuss laser plasma interaction in Sec. 2.3. Here, we derive and identify the ponderomotive force as the main force opposing electrostatic or thermal pressure in a light-plasma interaction scenario in Subsec. 2.3.1. In Subsec. 2.3.2 we introduce

parametric instabilities, such as Raman and Brillouin scattering. After deriving the models and discussing their dispersion, we summarize other instabilities in Subsec. 2.3.2 and draw a conclusion why the strong coupling regime is very relevant for Brillouin amplification, on which we will focus throughout the whole thesis.

Ch. 3 focuses on the simulation techniques and gives an overview about the most important effects regarding Brillouin amplification. We introduce the basic simulation models used in this work with the $\delta N\mathbf{A}$-model and the envelope three-wave interaction model in Sec. 3.1. Their implementation is done in C++, using the library PETSc [83, 84]. Afterwards, we show the amplification process in more detail, listing differences between weakly and strongly coupled Brillouin and discussing growth rate and frequency in both linear and nonlinear regime in Sec. 3.2.

With these basis set, the main part of this work subdivides into four main chapters.

In Ch. 4 we derive a full kinetic collisionless relativistic dispersion relation for an arbitrary ion species plasma interacting with laser light. After the derivation in Sec. 4.1, which is presented in appendix A.1 in detail, we briefly discuss Hydrogen plasma in Sec. 4.2 and consecutively specify on the electron-positron plasma case in Sec. 4.3. In the latter we note a dramatic difference from the fluid description in the weak coupling regime for Brillouin amplification, rendering the kinetic treatment crucial. However, we conclude in Sec. 4.4 that for strong coupling both fluid and kinetic description correspond, justifying the use of the former in the following chapters. This fourth chapter is solely based on an analytic treatment and builds up the manuscript [73].

Having the analytic background placed, Ch. 5 follows up discussing the transition between weak and strong coupling Brillouin amplification. We present simulations performed with the aforementioned models in Sec. 5.1, and describe at first the linear regime of interaction, where the pump stays unaffected in Sec. 5.1.1. A spectral observation leads to a criterion for the transition in the pump depletion regime given in Sec. 5.1.2, eventually depending on temperature, density and pump strength. Afterwards, we discuss the effect of a Gaussian shaped pump on the interaction in Sec. 5.3. With this we conclude in Sec. 5.4 three distinct reasons why the transitional case is important. Initially weakly coupled setups develop strong coupling due to amplification of the seed pulse. Initially strongly coupled setups develop weak coupling structures in the tail trailing the maximum due to pump depletion, which severely reduces the overall energy transmission efficiency and, lastly, we discuss longitudinally Gaussian pump beam profiles, naturally exhibiting parts where the threshold for strong coupling is exceeded and others where this is not the case. We also discuss the possibility of a self-similar treatment for the transitional case in appendix A.2. The content of this chapter was published in the following manuscript [58].

With both the analytic background and transition scenario discussed, we investigate the influence a quadratic pulse chirp has on the amplification process in Ch. 6. For this reason, we slightly expand the simulation model given in Sec. 3.1 while simultaneously neglecting other terms in Sec. 6.1. We distinguish the influence the chirp has in the linear regime in Sec. 6.2 and nonlinear regime in Sec. 6.3. Afterwards, we formulate the concept of an intrinsic chirp unique to strongly coupled Brillouin amplification in Sec. 6.4. The substance of this chapter was published in the manuscript [62].

Despite this work at hand was done theoretically, we stress its experimental relevance. Especially chapters 5 and 6 deal with problems affecting today's experiments, as they are performed in parameter regimes relevant for the transition between weak and strong coupling and actual laser pulses are always affected by chirp. Furthermore, in the course of working on this thesis, the author held multiple meetings with experimental groups, resulting in theoretical investigations and preparations for experiments. This work is summarized in Ch. 7. In Sec. 7.1 we show particle-in-cell simulations done with the code EPOCH [85, 86] for clarifying a low energy transmission efficiency due to spontaneous Raman backscattering of the pump pulse. Sec. 7.2 deals with plasma ionization and especially inverse bremsstrahlung as the major absorption mechanism, rendering an experimental setup without a mere ionization laser futile. At last in Sec. 7.3 we discuss with simulations the influence of the sign of the pump pulse chirp and its relevance for experiments.

In the end we summarize the contributions made throughout the work explained in this thesis in Ch. 8. We also give an outlook into future investigations for theory and experiment.

The author's contributions consist of the derivation of the relativistic kinetic dispersion relation in Ch. 4 and its discussion as well as comparison to the fluid model. The two envelope models used in chapters 5 and 6 were also derived and implemented by the author. The author performed the simulations shown in these two chapters and interpreted the results, as well as he tried to formulate the self-similar solution, i.e. the work presented in appendices A.1 and A.2 was performed by the author. The analytic estimate given for the transition time starting with an arbitrary weak coupling setup in Ch. 5 was formulated by the author. The simulations shown in Ch. 7 were done by the author. All images and figures used throughout this thesis are done by the author, as well as is the text.

Note that all equations given in this thesis are in Gaussian CGS-units, but whenever we calculate values, we give the dimensions in SI-units.

2 Basics of laser-plasma interaction

The following chapter introduces the basic principles, keywords and parameters for laser plasma interaction. We move from a very general description, following the explanations given in [78], more into detail when we discuss scattering of photons off plasmons or phonons, respectively, eventually introducing Brillouin amplification.

Sec. 2.1 deals with fundamental concepts of plasma physics such as ionization (Subsec. 2.1.1), plasma frequency, Debye-shielding, Maxwellian distributions and thermal velocity (Subsec. 2.1.2). Furthermore, Langmuir waves and ion acoustic modes are discussed via the plasma dispersion relation (Subsec. 2.1.3).

In Sec. 2.2 Gaussian beam parameters are introduced in order to describe ultra-short ultra-intense laser pulses. We take a note on a solution of the paraxial wave equation and explain the key parameters such as Rayleigh length and beam waist. Furthermore, we introduce the concept of chirp, later on being relevant in Ch. 6.

In Sec. 2.3 we introduce the most relevant equations for the work at hand. For the discussion of the Vlasov equation and introduction of the hydrodynamic description we mainly follow chapters 4 and 5 in [81]. We discuss Raman and Brillouin amplification, introduce the strong coupling regime and also take a note on different scattering mechanisms.

First, we give an overview over the equations used in this work and analyze their physical meaning.

The very famous Maxwell equations

$$\nabla \cdot \mathbf{E} = 4\pi\rho, \tag{2.1}$$

$$\nabla \cdot \mathbf{B} = 0, \tag{2.2}$$

$$\nabla \times \mathbf{E} = -\frac{1}{c}\frac{\partial \mathbf{B}}{\partial t}, \tag{2.3}$$

$$\nabla \times \mathbf{B} = \frac{1}{c}\left(4\pi\mathbf{j} + \frac{\partial \mathbf{E}}{\partial t}\right) \tag{2.4}$$

express the origin of electric and magnetic fields $\mathbf{E}$ and $\mathbf{B}$, respectively, and their connection. The variable $c \approx 3 \cdot 10^{10}$ cm/s denotes the speed of light and $\mathbf{j}$ the electric current, ∇ is the nabla operator $\nabla = \partial/\partial_x\hat{\mathbf{x}} + \partial/\partial_y\hat{\mathbf{y}} + \partial/\partial_z\hat{\mathbf{z}}$. In detail, the divergence operator $\nabla\cdot$ calculates wheter a vector field has sources or drains

in a specific volume. Eq. (2.1) is also known as Gauss' law or Poisson equation, stating that electric charges are the sources of electric fields, with charge density $\rho = qn$, where q is the electric charge and n the particle density. On the other hand, Eq. (2.2) does not imply that there are no sources of magnetic fields, but rather no magnetic monopoles, i.e. the sum of magnetic field lines entering and leaving a specific volume surface is zero. Eq. (2.3) is also known as Faraday's law, stating that the change in a magnetic field induces an electric field. Lastly, Eq. (2.4) is also known as Ampere's law, stating that the change in an electric field and an electric current induce a magnetic field.

In addition to expressing the electric field via a potential, we can also derive the magnetic field from a potential and define $\mathbf{B} = \nabla \times \mathbf{A}$ and $\mathbf{E} = -\nabla\phi - (1/c)\partial\mathbf{A}/\partial t$. Note that for low amplitudes $||(1/c)\partial\mathbf{A}/\partial t|| \ll ||\nabla\phi||$ one can often write $\mathbf{E} \approx -\nabla\phi$. With these potentials, we can rewrite the Maxwell equations (2.1)-(2.4) into

$$\nabla^2\phi - \frac{1}{c^2}\frac{\partial^2}{\partial t^2}\phi = -4\pi\rho, \tag{2.5}$$

$$\nabla^2\mathbf{A} - \frac{1}{c^2}\frac{\partial^2}{\partial t^2}\mathbf{A} = -4\pi\frac{\mathbf{j}}{c}, \tag{2.6}$$

two wave equations for ϕ and $\mathbf{A}$, respectively. However, these potentials are arbitrary up to a gauge that can be chosen freely. Since only $\mathbf{E}$ and $\mathbf{B}$ are physically relevant quantities, the potentials can be altered into ϕ' and $\mathbf{A}'$ via

$$\phi' = \phi - \frac{\partial\lambda}{\partial t}, \qquad\qquad \mathbf{A}' = \mathbf{A} + \nabla\lambda,$$

where λ is an arbitrary scalar function differentiable two times with respect to space and time. These changed potentials will still result in the same electromagnetic fields. The above Eqs. (2.5)-(2.6) use the so called Lorenz gauge $\nabla \cdot \mathbf{A} = -\partial\phi/\partial t$. Another widely used gauge is the Coulomb gauge $\nabla \cdot \mathbf{A} = 0$. For more information see Appendix 4 in [78].

The four Maxwell equations are sufficient to describe the propagation of radiation, induction of current and other phenomena related to electromagnetic fields. However, investigating laser-plasma interaction, we also need equations covering the particle response. We start with the also famous Vlasov equation

$$\frac{\partial}{\partial t}f_k + \mathbf{v} \cdot \nabla_\mathbf{r} f_k + q_k\left(\mathbf{E} + \frac{1}{c}\mathbf{v} \times \mathbf{B}\right) \cdot \nabla_\mathbf{p} f_k = 0, \tag{2.7}$$

with the one-particle distribution function $f_k(\mathbf{r}, \mathbf{p}, t)$ for particle species k. The variable $\mathbf{v}$ denotes the velocity, $\nabla_\mathbf{r}$ acts on the spatial coordinates $\mathbf{r}$ and $\nabla_\mathbf{p}$ on the momentum coordinates $\mathbf{p}$. This Eq. (2.7) neglects collisions between particles. Thus, changes in the distribution function only happens due to internal and external electromagnetic fields and the initial distribution. This is a valid approximation, if the number of particles in the Debye-sphere (see introduction of (2.18)) is large.

The Vlasov equation is a kinetic equation following from the Liouville equation, for more insights see e.g. chapter 4 in [81].

The Vlasov equation is the most general particle description that will be used in this work. It enables to get statistical information in the position-momentum space $(\mathbf{r}, \mathbf{v})$ at any time t. Frequently, one is not interested in the momentum distribution. Integrating over the velocity causes a loss in information, resulting in so called moments of the distribution function f_k. Note that treating momentum and velocity equivalently is only valid in the non-relativistic limit.

With this aforementioned simplification of the kinetic treatment we arrive at the hydrodynamic picture. The latter is applicable only on time scales larger than possible with kinetic treatment. We define the particle density of species k

$$n_k(\mathbf{r}, t) = \int_{-\infty}^{\infty} d\mathbf{v} \, f_k(\mathbf{r}, \mathbf{v}, t). \tag{2.8}$$

Additionally, we define the mean velocity

$$\mathbf{u}_k = \langle \mathbf{v} \rangle = \frac{\int_{-\infty}^{\infty} d\mathbf{v} \, \mathbf{v} f_k(\mathbf{r}, \mathbf{v}, t)}{\int_{-\infty}^{\infty} d\mathbf{v} f_k(\mathbf{r}, \mathbf{v}, t)}. \tag{2.9}$$

Integrating the Vlasov equation (2.7) over velocity we find

$$\frac{\partial}{\partial t} n_k + \nabla \cdot (n_k \mathbf{u}_k) = 0, \tag{2.10}$$

noting that $f_k(v \to \pm\infty) \to 0$ as there are no particles at $v \to \pm\infty$. Eq. (2.10) is know as the (particle) continuity equation. Multiplying the Vlasov equation (2.7) with $\mathbf{v}$ and integrating over the velocity delivers

$$\frac{\partial}{\partial t} \mathbf{u}_k + (\mathbf{u}_k \cdot \nabla) \mathbf{u}_k - \frac{q_k}{m_k} \left(\mathbf{E} + \frac{\mathbf{u}_k}{c} \times \mathbf{B} \right) = -\frac{1}{m_k n_k} \nabla P_k, \tag{2.11}$$

where we have used the continuity equation (2.10), for more details see chapter 5.1 in [81]. This is the momentum balance, allowing to calculate the mean velocity of particle type k, where q_k defines the charge and m_k the mass of particle of type k. Note that equivalently to Eq. (2.11) the momentum balance can be written in the form

$$\frac{\partial}{\partial t} (n_k \mathbf{u}_k) + \nabla \cdot (n_k \mathbf{u}_k \mathbf{u}_k) - \frac{q_k n_k}{m_k} (\mathbf{E} + \mathbf{u}_k \times \mathbf{B}) = -\frac{1}{m_k} \nabla P_k. \tag{2.12}$$

In principle, one finds a hierarchy of equations: The zeroth moment of the Vlasov equation, i.e. the equation describing the density (2.10), contains the mean velocity. The mean velocity is defined via the first moment of the Vlasov equation (2.11), which contains the pressure P_k. One could go on and derive an equation for the pressure term, but at one point we need to stop the hierarchy. Since all calculations in this work only base on either the Vlasov equation (2.7) or continuity equation plus momentum balance (2.10)-(2.11), we stop the derivation right here. When solving Eq. (2.11), one needs an appropriate ansatz for the pressure term P_k, e.g. the particles following isothermal ideal gas behavior. For applications, see e.g. Sec. 2.1.3.

2.1 Plasma

2.1.1 Ionization

The explanation of ionization at hand basically follows the explanations given in Ch. 2.1 in [78].

Ionization is the process where an atom loses a bound electron. A neutral atom has as many electrons as protons, i.e. an atom that has lost Z electrons is Z times ionized. We call Z the charge state or ionization state. Describing the thermodynamic state of an atom compound, we use the free energy F $[J/kg]$, depending on temperature T, volume V and number of particles N_j of charge state j.

Reaching thermodynamic equilibrium means that the free energy $F(T, V, N_j)$ is minimized. For describing the density distribution of different charge states of such an atom compound in thermodynamic equilibrium we use the Saha equations

$$\frac{n_{j+1} n_e}{n_j} = 2 \frac{U_{j+1}}{U_j} \left(\frac{2\pi m_e k_B T}{h^2} \right)^{3/2} \exp \left(-\frac{I_j - \Delta I_j}{k_B T} \right), \quad j = 1, 2, ..., (Z-1),$$

(2.13)

where $n_j = N_j/V$ is the particle density of charge state j, n_e is the electron density, U_j is the internal energy of charge state j, $m_e \approx 9.11 \cdot 10^{-31}$ kg the electron mass, $k_B \approx 1.38 \cdot 10^{-23}$ J/K is Boltzmann's constant, $h \approx 6.63 \cdot 10^{-34}$ Js is Planck's constant, I_j is the ionization energy of the ground state and ΔI_j is the reduction of the ionization potential due to local electrostatic fields.

Such a compound of atoms which is at least partially ionized can be called - under some premises following in the next sections - a plasma. The Saha equations are valid, whenever plasma is in local thermodynamic equilibrium (LTE). This means, we have parameters such as charge state, density and mean velocities following Boltzmann distributions

$$n_j \propto \exp \left(-\frac{E_j}{k_B T} \right),$$

(2.14)

where E_j is the energy level above the ground state. In local thermodynamic equilibrium all laws of thermodynamic equilibrium are valid but Planck's radiation law, i.e. the plasma can lose radiation.

2.1.2 Defining parameters

Important in many different fields in physics is the so called cross section σ of a process. It has the unit of an area and gives the probability of an event. Imagining hard spheres colliding, the cross section would be the intersection area $\sigma \approx \pi r^2$, where r is the radius.

For the deflection of a charged test particle off a fixed charge, e.g. an electron scattering of a nucleus, the calculation of the cross section becomes more complicated. The interacting force is no longer just a mechanical push but following Coulomb interaction. Hence, the cross section depends e.g. on the initial velocity. A lower speed equals a larger interaction time and therefore larger deflection or even trapping of the test particle.

With the cross section σ_{ab} of an interaction between test particle a and background particle b we define the mean free path $l_{ab} = 1/n_b\sigma_{ab}$. This is the length the test particle propagates before it undergoes the specific reaction. If the test particle velocity is v_a we can define the collision frequency $\nu_{ab} = v_a/l_{ab}$, i.e. the number of events per second.

Calculating ν_{ei} in plasma, i.e. the collision frequency of electrons and ions, is more difficult. Electrons in LTE follow a velocity distribution, namely the Maxwell distribution,

$$f(v) = A \exp\left(-\frac{v^2}{v_{the}^2}\right),$$

(2.15)

where A is the normalization factor such that the integral over f over all velocities equals 1. $v_{the} = \sqrt{k_B T_e/m_e}$ is the thermal velocity for electrons. Calculating the collision frequency now requires averaging, i.e. integrating, over the product of cross section and velocity, namely $\nu_{ei} = <\sigma_{ei}v_e>_v n_i$.

Retaining the classical description and not calculating the cross section quantum mechanically [87], one finds

$$\nu_{ei} \approx 2.9 \cdot 10^{-6} \frac{Z^2 n_i \, (cm^{-3}) \ln(\Lambda)}{(T_e(eV))^{3/2}} (s^{-1}),$$

(2.16)

also known as the Spitzer-formula [88], where $\ln(\Lambda)$ is the so called Coulomb logarithm. This is the logarithm of the ratio of the integration range when calculating the collision frequency. It is affected by uncertainty, typical values range from 5 to 15 (see e.g. [89]).

The Maxwell distribution (2.15) will play an important role in the derivation of the kinetic dispersion relation in Ch. 4. The collision frequency (2.16) is needed to estimate radiation absorption via inverse bremsstrahlung, i.e. electron-ion collisions under absorption of photons, in Ch. 7.

The Coulomb potential is an infinite-range potential, following $\phi_{\text{Coulomb}} \propto 1/r$. Thus, it decays proportionally to the distance from its center of origin. However,

since in plasma one finds many free charged particles, this behavior changes. Assuming a static positive ion, eventually it will be surrounded by negatively charged electrons. In a far-field the sum of the Coulomb potentials will cancel out. This is called screening effect or Debye-shielding [78, 81]. It leads to quasi-neutrality of the plasma on mesoscopic scales, defined by the Debye length

$$\lambda_{De} = \sqrt{\frac{k_B T_e}{4\pi e^2 n_{e0}}}, \tag{2.17}$$

where $e = 4.8 \cdot 10-10$ esu $\approx 1.6 \cdot 10^{-19}$ C is the elementary charge and n_{e0} the electron background density. With this we find [78] the altered potential

$$\phi \propto \frac{1}{r} \exp\left(-\frac{r}{\lambda_{De}}\right). \tag{2.18}$$

Eq. (2.18) implies that the long-range Coulomb potential is now shortened to an effective distance of the order of λ_{De} [78].

Considering a cold plasma $T_e = T_i = 0$ without any external electric or magnetic fields implies vanishing thermal velocities or pressure terms. Since ions are much heavier than electrons, e.g. $m_i/m_e \approx 1836$ in case of Hydrogen, they can be assumed to be static bodies in space, neutralized by the light electrons. Applying a small external force on the plasma would lead to an electron disposition, resulting in a local electric field. We consider the equations

$$\mathbf{j}_e = -n_e e \mathbf{v}_e, \tag{2.19}$$

$$\nabla \cdot \mathbf{j}_e + e\frac{\partial n_e}{\partial t} = 0, \tag{2.20}$$

$$\nabla^2 \phi = -4\pi e n_e. \tag{2.21}$$

Eq. (2.19) is defining the electric current, carried by the density n_e with velocity $\mathbf{v}_e$. Eq. (2.20) is the charge continuity equation (see Eq. (2.10) for similarity). It states that sources or drains of current must be due to charge density fluctuations. Eq. (2.21) is the Poisson equation (see Eq. (2.1)), implying that charges are sources of an electric field since $\mathbf{E} \approx -\nabla\phi$. Using Newton's equation of motion via identifying that the only force acting on electrons is due to the electric field we formulate

$$m_e \frac{\partial \mathbf{v}}{\partial t} = -e\nabla\phi. \tag{2.22}$$

Replacing the velocity with the current Eq. (2.19) we write

$$m_e \frac{\partial \mathbf{v}}{\partial t} = m_e \frac{\partial}{\partial t}\frac{-\mathbf{j}_e}{e n_e} \approx -\frac{m_e}{e n_{e0}}\frac{\partial \mathbf{j}_e}{\partial t}, \tag{2.23}$$

where we assumed small density fluctuations compared to changes in the electron velocity. Taking the divergence of Eq. (2.23) allows us to replace the left-hand-side with Eq. (2.20) and the right-hand-side with Eq. (2.21), obtaining

$$\frac{\partial^2}{\partial t^2} n_e + \frac{4\pi e^2 n_{e0}}{m_e} n_e = 0. \tag{2.24}$$

This Eq. (2.24) is an oscillator ordinary differential equation where we identify

$$\omega_{pe} = \sqrt{\frac{4\pi e^2 n_{e0}}{m_e}} \tag{2.25}$$

as the electron plasma frequency, which is a very significant parameter describing plasmas. It can be understood as the definition of the time scale with which plasma can react to external perturbations. Furthermore, we notice the very handy relation

$$\omega_{pe} = \frac{\lambda_{De}}{v_{the}}, \tag{2.26}$$

relating the time scale, length scale for quasi-neutrality and thermal motion of electrons in a plasma.

In the next subsection we introduce different waves that can exist in plasma, so called eigenmodes, especially Langmuir and ion acoustic waves. We derive their dispersion relation, i.e. the relation between frequency and wave number $\omega(k)$.

2.1.3 Dispersion

This subsection will introduce electron plasma waves and ion acoustic waves, as they can exist in plasmas and are the responsible waves later on allowing Raman and Brillouin scattering, respectively. Throughout this paragraph, we will basically follow the description used in chapter 1.5 in [41].

We use the fluid model for electrons and ions derived above, i.e. Eqs. (2.10) and (2.12). We stick to one-dimensional motion in **x**-direction, i.e. $\mathbf{u} = u$ and $\mathbf{E} = E$. Focusing on the high frequency electron wave first, we summarize

$$\frac{\partial n_e}{\partial t} + \frac{\partial}{\partial x}\left(n_e u_e\right) = 0, \tag{2.27}$$

$$\frac{\partial}{\partial t}\left(n_e u_e\right) + \frac{\partial}{\partial x}\left(n_e u_e^2\right) = -\frac{n_e e E}{m_e} - \frac{1}{m_e}\frac{\partial P_e}{\partial x}, \tag{2.28}$$

$$\frac{P_e}{n_e^3} = \text{const.}, \tag{2.29}$$

where Eq. (2.29) is the adiabatic equation of state, implying electrons moving much slower than the plasma wave phase velocity $v_{the} \ll \omega/k$. Taking the time derivative of Eq. (2.27), space derivative of Eq. (2.28) and inserting each other delivers

$$\frac{\partial^2 n_e}{\partial t^2} - \frac{\partial^2}{\partial x^2}\left(n_e u_e^2\right) - \frac{e}{m_e}\frac{\partial\left(n_e E\right)}{\partial x} - \frac{1}{m_e}\frac{\partial^2 P_e}{\partial x^2} = 0. \tag{2.30}$$

We take the Poisson equation (2.1), replacing the density on the right-hand-side with the sum over electrons and static ions

$$\frac{\partial E}{\partial x} = -4\pi e\left(n_e - Z n_{i0}\right), \tag{2.31}$$

and perturb the system of Eqs. (2.29)-(2.31) via $n_e = n_{e0} + \epsilon n_{e1}$, $u_e = u_{e0} + \epsilon u_{e1}$ with $u_{e0} = 0$, $P_e = n_{e0}k_B T_e + \epsilon P_{e1}$ and $E = E_0 + \epsilon E_1$ with $E_0 = 0$, where ϵ is a small number. Applying this gives rise to

$$P_{e1} = 3m v_{the}^2 n_{e1}, \tag{2.32}$$

$$\frac{\partial E_1}{\partial x} = -4\pi e n_{e1}, \tag{2.33}$$

$$\frac{\partial^2 n_{e1}}{\partial t^2} - \frac{n_0 e}{m_e}\frac{\partial E_1}{\partial x} - \frac{\partial^2 P_{e1}}{\partial x^2} = 0. \tag{2.34}$$

Inserting Eqs. (2.32) and (2.33) into Eq. (2.34) leads to

$$\left(\frac{\partial^2}{\partial t^2} - 3v_{the}^2\frac{\partial^2}{\partial x^2} + \omega_{pe}^2\right) n_{e1} = 0, \tag{2.35}$$

that can be Fourier transformed to obtain the dispersion relation for electron plasma waves

$$\omega^2 = \omega_{pe}^2 + 3k^2 v_{the}^2. \tag{2.36}$$

Usually, $\omega_{pe}^2 \gg 3k^2 v_{the}^2$, i.e. the frequency of that plasma wave is mainly given by the electron plasma frequency. These electron plasma waves are also known as Langmuir waves.

The other type of plasma wave, the low frequency ion acoustic waves, only exists because of contributions of both, electrons and ions. As it is low in frequency, we can neglect phenomena acting on the time-scale of ω_{pe}, i.e. neglecting electron inertia. We again stick to one-dimensional motion and model the electron pressure isothermally, i.e. $P_e = n_e k_B T_e$. Electrons are fast enough to balance thermal fluctuations. With these assumptions the momentum balance for electrons simplifies to

$$n_{e0} e E_1 = -k_B T_e \frac{\partial n_{e1}}{\partial x}. \tag{2.37}$$

For ions we formulate a similar system to the derivation of Langmuir waves by stating

$$\frac{\partial n_i}{\partial t} + \frac{\partial}{\partial x} (n_i u_i) = 0, \tag{2.38}$$

$$\frac{\partial}{\partial t} (n_i u_i) + \frac{\partial}{\partial x} (n_i u_i^2) = \frac{Ze}{m_i} n_i E - \frac{1}{m_i} \frac{\partial P_i}{\partial x}, \tag{2.39}$$

$$\frac{P_i}{n_i^3} = \text{const.}, \tag{2.40}$$

i.e. consisting of continuity equation, momentum balance and the adiabatic equation of state. The same ansatz as for Langmuir wave yields

$$\frac{\partial^2 n_i}{\partial t^2} - \frac{\partial^2}{\partial x^2} (n_i u_i^2) + \frac{Ze}{m_i} \frac{\partial}{\partial x} (n_i E) - \frac{1}{m_i} \frac{\partial^2 P_i}{\partial x^2} = 0. \tag{2.41}$$

We state that the factor between the unperturbed ion and electron density is the charge state $n_{i0} = n_{e0}/Z$. Additionally, perturbing the system similar to above via $n_i = n_{e0}/Z + \epsilon n_{i1}$, $u_i = \epsilon u_{i1}$, $P_i = P_{i0} + \epsilon 3 k_B T_i n_{i1}$ and $E = \epsilon E_1$ delivers

$$\frac{\partial^2 n_{i1}}{\partial t^2} + \frac{Z e n_{e0}}{m_i} \frac{\partial E_1}{\partial x} - \frac{3 k_B T_i}{m_i} \frac{\partial^2 n_{i1}}{\partial x^2} = 0. \tag{2.42}$$

Now we insert Eq. (2.37) into Eq. (2.42), assuming $n_{e1} \approx Z n_{i1}$, i.e. that electrons follow the low speed ions, in order to find

$$\frac{\partial^2 n_{i1}}{\partial t^2} - \frac{Z k_B T_e + 3 k_B T_i}{m_i} \frac{\partial^2 n_{i1}}{\partial x^2} = 0. \tag{2.43}$$

Again Fourier transforming Eq. (2.43) delivers the dispersion relation

$$\omega^2 = k^2 c_s^2, \tag{2.44}$$

where $c_s = \sqrt{(Z k_B T_e + 3 k_B T_i)/m_i}$ is the ion sound velocity. Note that typically $T_e \gg T_i$ and hence $c_s \approx \sqrt{Z k_B T_e / m_i}$.

We point out that different to Langmuir waves these ion acoustic waves have frequencies around $\omega \sim 0$ instead of $\omega \sim \omega_{pe}$, i.e. are indeed low frequency. They are the analogue of sound waves in neutral gases [41], that is why they are called ion acoustic waves.

2.2 Laser light

This section gives the mathematical description and explanation of what we interpret as a laser pulse. We will not give insight into the different parts of a laser system or the different possibilities to generate laser radiation, but rather describe a Gaussian beam and the principle of chirped pulse amplification.

Whenever we talk about laser pulses in this work, we assume (super-) Gaussian pulses, i.e. temporally restrained TEM_{00} modes of a laser fulfilling the paraxial wave equation (see e.g. [90])

$$
\begin{aligned}
\mathbf{E}(\mathbf{r}, z, t) =& E_0 \mathbf{x} \frac{w_0}{w(z)} \exp\left(-\frac{r^2}{w(z)^2}\right) \exp\left(i\left[\omega t - kz - k\frac{r^2}{2R(z)} + \psi(z)\right]\right) \\
& \exp\left(-\frac{(z + z_0 - v_g t)^n}{\sigma^n}\right),
\end{aligned} \tag{2.45}
$$

moving into z-direction, where $\mathbf{r}$ is the transverse space direction using cylindrical coordinates. The electric field is polarized in x-direction. Here, E_0 denotes the amplitude and $\mathbf{x}$ the unit vector in x-direction, i.e. the direction of polarization. The beam waist w_0 marks the lowest radius the laser pulse can have, while $w(z)$ is the radius at position z in propagation direction, i.e. $w(0) = w_0$. Note that the radius is defined by a drop in field amplitude by a factor of $1/e$, where e denotes the Euler constant. The radial distance is given by r, the curvature of the wavefronts at position z is given by $R(z)$. The Gouy phase at z is given by $\psi(z)$, ω denotes the frequency, while k stands for the wavenumber. We note, that this form is the complex representation of a plane wave. By transforming the basis, one could also rewrite the complex expression of the electric field into a real term consisting of sin or cos functions. The group velocity $v_g = \partial\omega/\partial k$ depends on the medium the pulse propagates in, as the dependency $\omega(k)$ is given by the dispersion relation. For vacuum one finds $\omega = ck$, for plasma we have $\omega^2 = c^2 k^2 + \omega_{pe}^2$. Lastly, σ denotes the length of the laser pulse.

Let us have a closer look at the different terms in Eq. (2.45). The polarization in $\mathbf{x}$ direction is known as linear polarization, defining in which direction the $\mathbf{E}$-field vector points. In electromagnetic radiation, the magnetic field is perpendicular on the electric field, i.e. in this example $\mathbf{B}$ points into $\mathbf{y}$ direction. There is also the possibility of circular polarization: Here, $\mathbf{E}$ and $\mathbf{B}$ do not oscillate but stay constant in amplitude and rotate transversely to the propagation direction.

The term $\exp\left(-r^2/w(z)^2\right)$ defines the transverse profile (envelope) of the pulse.

The spot size parameter $w(z)$ is given via

$$w(z) = w_0 \sqrt{1 + \left(\frac{z}{z_R}\right)^2}, \qquad \text{with} \qquad (2.46)$$

$$z_R = \frac{\pi w_0^2}{\lambda_0}, \qquad (2.47)$$

where z_R is called the Rayleigh length. The value $\sqrt{2\log(2)}w(z)$ defines the full width at half maximum (FWHM) at position z, i.e. the radial laser width at which the amplitude has dropped to 50% at both ends. The Rayleigh length, depending on the beam waist and central wavelength λ_0, is the range z at which the width $w(z)$ is $\sqrt{2}$ times larger than in focus, where it is w_0.

Similarly, the term $\exp\left(-\left(z + z_0 - v_g t\right)^n / \sigma^n\right)$ describes the longitudinal profile or envelope. Quite often, we consider super-Gaussian pulses with steep longitudinal edges, where $n \gg 2$. In the limit of a Gaussian profile, $n = 2$. z_0 is the initial displacement such that after the focusing time $t = t_{\text{focus}}$ we have $v_g t_{\text{focus}} = z_0$, i.e. the pulse is in focus. Here, the value $(2\log(2))^{1/n}\sigma$ defines the full width at half maximum in longitudinal direction.

The term $\exp(i\phi)$ defines the phase, i.e. the rapidly oscillating part of the electric field, opposite to the envelope parts mentioned above. The two parameters, radius of curvature and Gouy phase, are given by

$$R(z) = z\left(1 + \left(\frac{z_R}{z}\right)^2\right), \qquad \psi(z) = \arctan\left(\frac{z}{z_R}\right), \qquad (2.48)$$

i.e. again depending on the Rayleigh length z_R. The former describes the wavefront curvature in distance z, the latter causes an apparent wavelength change close to focus, however it is only relevant for higher order modes and neglected for Gaussian pulses discussed in this work.

Fig. 2.1 incorporates the parameters described above. The pulse starts at the left-hand-side, focuses down to the beam waist w_0 and consecutively defocuses again. The temporal profile is hinted as the blue gradient.
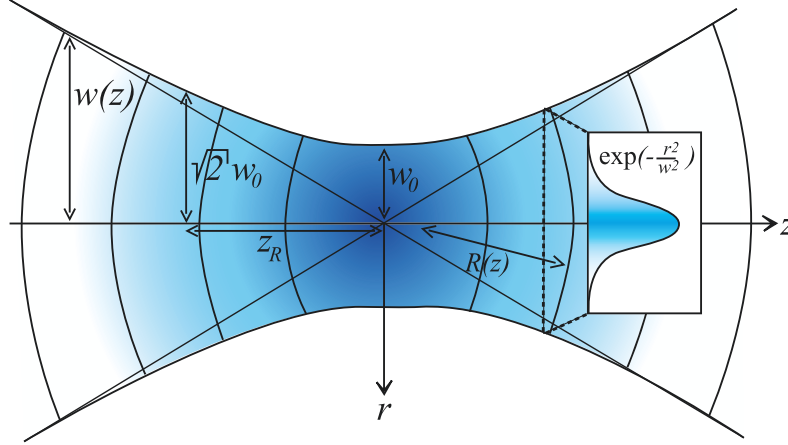
Figure 2.1: Gaussian laser pulse with key parameters as defined in text. The pulse focuses to the beam waist w_0 and defocuses afterwards. The plot inset depicts the transverse profile, the gradient color the temporal, longitudinal profile.

From basic Fourier theory we know that a Gaussian pulse in real space is also a Gaussian in Fourier space. This means a pulse limited in time consists of a range of wavelengths, rather than just one. However, there is still one distinguished wavelength at which the power spectrum has the largest magnitude. It is called the central wavelength λ_0. Furthermore, taking the time-frequency domain, we can define a bandwidth. This bandwidth is the full width at half maximum of a laser pulse Δt and $\Delta \omega$ for time- and frequency-domain, respectively. Note that Δt can also be referred to as the duration. The frequency bandwidth can be translated into a wavelength bandwidth via $\Delta \omega = 2\pi c \Delta \lambda / \lambda_0^2$. Having a Gaussian with a linear phase, i.e. constant frequency, translates into the following time-bandwidth product (TBP) [79]

$$\Delta t \Delta \omega \gtrsim 8 \log (2) \tag{2.49}$$

If the former inequality (2.49) becomes an equality, the laser pulse duration is called bandwidth limited.

Ultrashort laser pulse systems usually provide a fixed bandwidth of typically $\Delta \lambda \sim 1 - 100$ nm [49, 74, 75] due to how they are built. The bandwidth of a laser can only be stretched with nonlinear effects. However, they can release laser pulses of longer duration than what is fixed by the TBP in Eq. (2.49). This is done via application of a so called frequency chirp, i.e. varying the central frequency in time. If the frequency gets modulated linearly $\omega = \omega_0 \pm 2\alpha t$, the chirp is quadratic, as this results in a phase $\phi = \omega t \pm \alpha t^2$ quadratic in time. We call α the chirp-rate, which has the unit $[\alpha] = s^{-2}$. This is the type of chirp introduced here and used throughout the thesis.
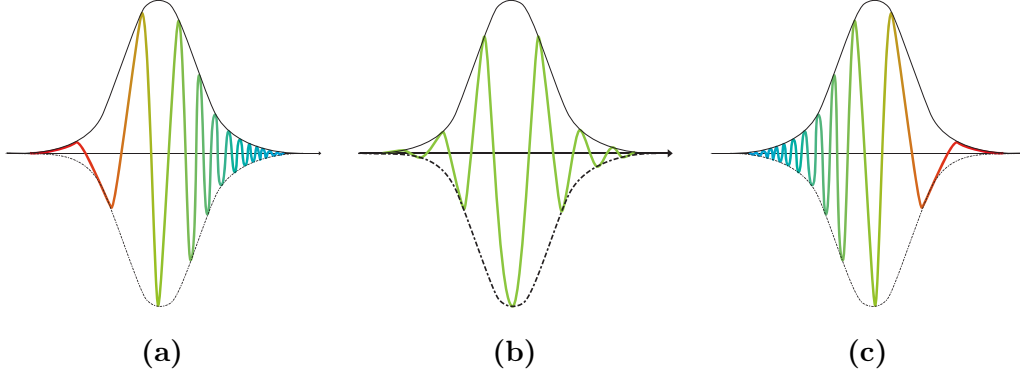
(a)   **(b)**   **(c)**

Figure 2.2: Three different kind of chirps, (a) negative $\alpha < 0$ (from high to low frequency in propagation direction), (b) zero, and (c) positive $\alpha > 0$ chirp (from low to high frequency).

Figuratively, chirping a laser pulse not only stretches it in time, but separates the front and back of it into parts with higher and lower frequency or vice versa, depending on the sign of α. This is illustrated in Fig. 2.2, where pulses propagate from left-to-right. In Fig. 2.2a one sees a negative chirp, where the head (front in propagation direction) has a higher frequency than the tail. The opposite is shown in Fig. 2.2c. The case where no chirp is applied is visible in the center in Fig. 2.2b.

The relation between chirp-rate α and the duration of the pulse can be calculated via

$$\alpha = \frac{\sqrt{\Delta\omega^2 \Delta t^2 - 64 \log{(2)}^2}}{2\Delta t^2}, \tag{2.50}$$

which means for a short duration slightly larger than the bandwidth limit, a large chirp is necessary. For longer durations the chirp-rate is lower. Note that in experimental physics, chirp is often defined in Fourier space, i.e. the opposite is true (large chirp $\rightarrow$ long duration). However, Eq. (2.50) is the definition of the chirp we stick to, especially in Ch. 6. Fig. 2.3 shows the relation between the pump duration Δt and the attributive chirp-rate α in Eq. (2.50). A conventional, constant laser bandwidth of $\Delta\lambda = 18$ nm was used.
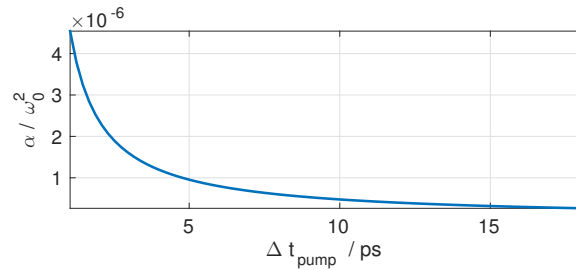

Figure 2.3: Chirp-rate of the pump α vs. attributive duration Δt for constant bandwidth $\Delta\lambda = 18$ nm.

2.3 Laser-plasma interaction

This section gives an overview about how laser light propagates in plasma. Furthermore, we introduce the critical density and discuss so called parametric instabilities, i.e. scattering of photons off quantized plasma oscillations. For example Raman and Brillouin scattering. In that course we basically follow the scheme given in [41] in Chs. 3, 7 and 8.

Knowing the vacuum dispersion of light $\omega = ck$, we derive light dispersion in plasma. Considering a one-dimensional electric field $\mathbf{E} = \mathbf{E}(\mathbf{x})\exp\left(-\mathrm{i}\omega t\right)$ with a rapidly oscillating phase $\omega \gtrsim \omega_{pe}$ exceeding the plasma frequency, we can again treat ions as neutralizing background charges $n_{i0} = Zn_{e0}$. The reason is that phenomena caused by this field will directly affect only the light electrons. Furthermore, we neglect the terms $\mathbf{u}_e \cdot \nabla \mathbf{u}_e$ and $\mathbf{u}_e \times \mathbf{B}$ in the electron momentum balance Eq. (2.11) and obtain

$$\frac{\partial \mathbf{u}_e}{\partial t} = -\frac{e}{m_e}\mathbf{E}(x)\exp\left(-\mathrm{i}\omega t\right) \tag{2.51}$$

as the equation describing the momentum change in electrons. Under consideration of Eq. (2.51), the electric current $\mathbf{j}_e = -n_{e0}e\mathbf{u}_e$ translates into

$$\frac{\partial \mathbf{j}_e}{\partial t} = \frac{\omega_{pe}^2}{4\pi}\mathbf{E}, \tag{2.52}$$

and via integration in time we find

$$\mathbf{j}_e = \frac{\mathrm{i}\omega_{pe}^2}{4\pi\omega}\mathbf{E}. \tag{2.53}$$

Considering the two Maxwell equations (2.3) and (2.4) and inserting Eqs. (2.51) and (2.53) we find

$$\nabla \times \mathbf{E} = \frac{\mathrm{i}\omega}{c}\mathbf{B}, \tag{2.54}$$

$$\nabla \times \mathbf{B} = -\frac{\mathrm{i}\omega}{c}\left(1 - \frac{\omega_{pe}^2}{\omega^2}\right)\mathbf{E}, \tag{2.55}$$

where $\epsilon \equiv 1 - \omega_{pe}^2/\omega^2$ is known as the dielectric function. Taking the curl of Eq. (2.55) and subsequently inserting Eq. (2.54) delivers

$$\nabla^2\mathbf{E} - \nabla\left(\nabla \cdot \mathbf{E}\right) + \frac{\omega^2}{c^2}\epsilon\mathbf{E} = 0. \tag{2.56}$$

Assuming a uniform density gives $\nabla \cdot \mathbf{E} = 0$, Fourier transforming Eq. (2.56) then gives the dispersion relation for light in plasma

$$\omega^2 = \omega_{pe}^2 + c^2 k^2. \tag{2.57}$$

Note that Eq. (2.57) implies that the lowest frequency light in plasma can have is ω_{pe}. This means that incident light with lower frequency would lead to an imaginary wavenumber k in order to fulfill Eq. (2.57). Hence, lasers with frequency $\omega < \omega_{pe}$ are forbidden to penetrate plasma. This can be understood via recalling that electron motion in plasma happens on time scales given by ω_{pe}. If an incident perturbation, e.g. laser light, occurs on slower time scales, the electrons are quick enough to rebalance any outer forces. Thus, light penetration into the medium is prevented.

In addition, the condition for light to enter plasma $\omega \gtrsim \omega_{pe}$ allows us to define the so called critical density n_c. It is the maximum density plasma can have such that light with a fixed frequency ω can still penetrate. In a mathematical form we write this

$$n_c = \frac{m_e \omega^2}{4\pi e^2} \tag{2.58}$$

as the critical density.

2.3.1 Ponderomotive force

In this subsection we derive the ponderomotive force. This is the force causing displacement of electrons in plasma due to light pressure, opening up the possibility for parametric instabilities. In the course we cover chapter 6.2 in [41].

We start with a homogeneous plasma in which a high frequency light wave propagates, similar to the previous consideration in Sec. 2.3. We change the basis to write the electric field as $\mathbf{E} = \mathbf{E}(x)\sin(\omega t)$, while $\omega \gtrsim \omega_{pe}$. Neglecting the electron pressure, the momentum balance Eq. (2.11) changes into

$$\frac{\partial \mathbf{u}_e}{\partial t} + (\mathbf{u}_e \cdot \nabla)\,\mathbf{u}_e = -\frac{e}{m_e}\mathbf{E}(x)\sin(\omega t)\,. \tag{2.59}$$

We split the electron velocity into two parts of different frequency $\mathbf{u}_e = \mathbf{u}_e^l + \mathbf{u}_e^h$. Next, we state that the change in the high frequency part $\partial \mathbf{u}_e^h/\partial t$ is only due to the rapidly oscillating electric field. With these two assumptions we can neglect the second term in Eq. (2.59) and integrate in time, yielding

$$\mathbf{u}_e^h = \frac{e\mathbf{E}}{m_e\omega}\cos(\omega t)\,, \tag{2.60}$$

i.e. a rapid oscillation by the electrons, phase shifted with respect to the laser field. Multiplying Eq. (2.59) with the electron mass m_e and averaging over the high frequency oscillation $\langle...\rangle_t$ delivers

$$m_e \frac{\partial \langle \mathbf{u}_e \rangle_t}{\partial t} = -e\langle \mathbf{E} \rangle_t - \frac{m_e}{2}\langle \nabla\left(\mathbf{u}_e^h \cdot \mathbf{u}_e^h\right)\rangle_t. \tag{2.61}$$

Inserting Eq. (2.60) changes Eq. (2.61) into

$$m_e \frac{\partial \langle \mathbf{u}_e \rangle_t}{\partial t} = -e\langle \mathbf{E} \rangle_t - \frac{1}{4}\frac{e^2}{m_e\omega^2}\nabla \mathbf{E}^2(x), \tag{2.62}$$

where we identify

$$\mathbf{F}_{\text{ponderomotive}} = -\frac{1}{4}\frac{e^2}{m_e\omega^2}\nabla \mathbf{E}^2(x) \tag{2.63}$$

as the ponderomotive force. This force proportional to the gradient of the electric field envelope squared pushes away the electrons from regions of high laser fields.

In the following we will discuss parametric instabilities, phenomena where laser light scatters off plasma oscillations. We remark that this laser light applies ponderomotive pressure which can get rebalanced by electron pressure. With the ponderomotive force, a plasma oscillation can be excited and if it is an eigenmode (see electron plasma oscillation and ion acoustic modes in Sec. 2.1.3) it can be amplified.

2.3.2 Parametric instabilities

Parametric instabilities are described by equations of parametric oscillators. The equation of such an oscillator is given by

$$\left(\frac{\partial^2}{\partial t^2} + \delta(t)\frac{\partial}{\partial t} + \omega^2(t) \right) f = 0, \tag{2.64}$$

i.e. a normal oscillator equation but with time dependent damping $\delta(t)$ and frequency $\omega(t)$. By this, the amplitude of the solution to Eq. (2.64) varies in time, i.e. can increase or decrease.

In the following two subsections we will derive equations for an incident photon decaying into a quantized oscillation in plasma plus a scattered photon. We describe both Raman scattering, where the plasma oscillation is a Langmuir wave, and Brillouin scattering. In the latter, we have ion acoustic waves.

This scattering mechanism can be harnessed as an amplification setup: We use two lasers counter-propagating each other. The experiment is manipulated in a way that all photons of the first laser become photons of the second laser under scattering via the parametric instability. This is the concept of laser amplification in plasma.

First, we always consider energy and momentum balance via

$$\omega_0 = \omega + \omega_1, \tag{2.65}$$
$$\mathbf{k}_0 = \mathbf{k} + \mathbf{k}_1, \tag{2.66}$$

where the index 0 denotes frequency and wavenumber of the incident photon, the index 1 marks the scattered photon and no index signals plasma quanta. Multiplying Eq. (2.65) by $\hbar$, i.e. Planck's constant, we can interpret the equation as conservation of energy. The same is true for Eq. (2.66) but for momentum.

In the derivation of plasma instabilities we always look for growth rates Γ defining the growth of the plasma wave and, thus, also the amplification factor. Considering a plane wave $\exp(-\mathrm{i}\omega t)$, if ω becomes complex $\omega = \omega_{\Re} + \mathrm{i}\Gamma$, we can rewrite it as $\exp(\Gamma t)\exp(-\mathrm{i}\omega_{\Re}t)$. This equals a wave that oscillates with frequency $\omega_{\Re}$ and grows exponentially in time with the growth rate Γ.

The pursuit of the following two subsections is to find these complex frequencies and hence the growth rates for Raman and Brillouin scattering, where we will follow chapters 7 and 8 in [41].

Raman scattering

Raman scattering is the inelastic decay of a light wave into a scattered light wave and a Langmuir wave. From Eq. (2.36) we know that the minimum frequency a

Langmuir wave can have is ω_{pe}. This means ω_0 must be larger than $2\omega_{pe}$, because if not, the scattered light wave with frequency ω_{pe} would not be allowed to propagate in plasma. This directly translates to the condition $n_0/n_c \lesssim 0.25$, i.e. Raman scattering can only occur in plasmas below quarter critical density.

In the following we derive the equations describing Raman scattering and derive the dispersion relation. We prove that indeed the Langmuir wave is the plasma oscillation necessary for the instability. In the end we discuss the growth rate and frequency of Raman scattering.

The wave equation for the vector potential $\mathbf{A}$ (2.6) in Coulomb-gauge $\nabla \cdot \mathbf{A} = 0$ is

$$\frac{\partial^2}{\partial t^2}\mathbf{A} - c^2\nabla^2\mathbf{A} = 4\pi c\mathbf{j} - c\frac{\partial}{\partial t}\nabla\phi, \tag{2.67}$$

where we separate the current into a longitudinal and transverse part $\mathbf{j} = \mathbf{j}_l + \mathbf{j}_t$. We connect the Poisson equation (2.21) with the charge continuity equation (2.20), stating that $\nabla \cdot \mathbf{j}_t = 0$, in order to find

$$\frac{\partial}{\partial t}\nabla\phi = 4\pi\mathbf{j}_l. \tag{2.68}$$

Inserting Eq. (2.68) into Eq. (2.67) we have

$$\left(\frac{\partial^2}{\partial t^2} - c^2\nabla^2\right)\mathbf{A} = 4\pi c\mathbf{j}_t. \tag{2.69}$$

We recall $\mathbf{j}_t = -n_e e\mathbf{u}_t$, i.e. the transverse current is carried by the transverse velocity of electrons oscillating in the laser field. The transverse part of the momentum balance leads to $\mathbf{u}_t = e\mathbf{A}/m_e c$ if $|\mathbf{u}_t| \ll c$. Inserting into Eq. (2.69) gives us an equation handling light propagation in plasma as

$$\left(\frac{\partial^2}{\partial t^2} - c^2\nabla^2\right)\mathbf{A} = -\frac{4\pi e^2 n_e}{m_e}\mathbf{A}, \tag{2.70}$$

where we will apply the perturbation ansatz $\mathbf{A} = \mathbf{A}_0 + \epsilon\mathbf{A}_1$ and $n_e = n_0 + \epsilon n_{e1}$, yielding the first order in ϵ equation

$$\left(\frac{\partial^2}{\partial t^2} - c^2\nabla^2 + \omega_{pe}^2\right)\mathbf{A}_1 = -\frac{4\pi e^2}{m_e}n_{e1}\mathbf{A}_0. \tag{2.71}$$

We note that the left-hand-side bracket applied on a plane wave would already give us the dispersion relation for light in plasma (2.57).

For the electrons we again take continuity equation (2.10) and momentum balance (2.11), separate the velocity $\mathbf{u}_e$ into longitudinal and transverse part $\mathbf{u}_e = \mathbf{u}_l + e\mathbf{A}/m_e c$ and find

$$\frac{\partial\mathbf{u}_l}{\partial t} = \frac{e}{m_e}\nabla\phi - \frac{1}{2}\nabla\left(\mathbf{u}_l + \frac{e\mathbf{A}}{m_e c}\right)^2 - \frac{1}{n_e m_e}\nabla P_e. \tag{2.72}$$

Note that the second term on the right-hand-side builds the ponderomotive force given by Eq. (2.63). Analog to the procedure in Sec. 2.1.3, we expand the perturbation ansatz by stating $\mathbf{u}_l = \mathbf{u}_0 + \epsilon\mathbf{u}_1$ and $\phi = \phi_0 + \epsilon\phi_1$, where $\mathbf{u}_0 = 0, \phi_0 = 0$. Hence, to first order in ϵ, continuity equation and momentum balance (2.72) read

$$\frac{\partial n_{e1}}{\partial t} + n_0 \nabla \cdot \mathbf{u}_1 = 0, \tag{2.73}$$

$$\frac{\partial u_1}{\partial t} = \frac{e}{m_e}\nabla\phi_1 - \frac{e^2}{m_e^2 c^2}\nabla(\mathbf{A}_0 \cdot \mathbf{A}_1) - \frac{3v_{the}^2}{n_0}\nabla n_{e1}, \tag{2.74}$$

where we have used again the adiabatic pressure assumption $P_e/n_e^3 = \text{const.}$ and v_{the} is the thermal velocity for electrons. Differentiation of Eq. (2.73) with respect to time and taking the divergence of Eq. (2.74) delivers

$$\left(\frac{\partial^2}{\partial t^2} + \omega_{pe}^2 - 3v_{the}^2\nabla^2\right)n_{e1} = \frac{n_0 e^2}{m_e^2 c^2}\nabla^2(\mathbf{A}_0 \cdot \mathbf{A}_1). \tag{2.75}$$

We note that the left-hand-side bracket applied on a plane wave would already give us the Langmuir dispersion relation (2.36).

Commenting on the system Eqs. (2.71) and (2.75), we can Fourier transform them in space and rewrite them as

$$\left[\frac{\partial^2}{\partial t^2} + \begin{pmatrix} \omega_1^2 & r_1 \\ r_2 & \omega_2^2 \end{pmatrix}\right]\mathcal{B} = 0, \tag{2.76}$$

where $\mathcal{B} = (\mathbf{A}_1, n_{e1})$, $\omega_1^2 = \omega_{pe}^2 + c^2 k^2$, $\omega_2^2 = \omega_{pe}^2 + 3v_{the}^2 k^2$ and r_1 and r_2 are the right-hand-sides including $\mathbf{A}_0$ in Eqs. (2.71) and (2.75), respectively. In this form we directly see the analogy to the parametric oscillator equation (2.64). The frequency term $\omega^2(t)$ is now replaced with the matrix having all components filled, thus delivering a time dependent frequency.

Eqs. (2.71) and (2.75) with a plane wave ansatz $\mathbf{A}_0 = \tilde{\mathbf{A}}_0 \cos(\mathbf{k}_0 \cdot \mathbf{x} - \omega_0 t)$ in Fourier space read

$$\left(\omega^2 - c^2 k^2 - \omega_{pe}^2\right)\mathbf{A}_1(\mathbf{k}, \omega) =$$
$$\frac{4\pi e^2}{2m_e}\tilde{\mathbf{A}}_0\left[n_{e1}(\mathbf{k} - \mathbf{k}_0, \omega - \omega_0) + n_{e1}(\mathbf{k} + \mathbf{k}_0, \omega + \omega_0)\right], \tag{2.77}$$

$$\left(\omega^2 - 3v_{the}^2 k^2 - \omega_{pe}^2\right)n_{e1}(\mathbf{k}, \omega) =$$
$$\frac{k^2 e^2 n_0}{2m_e^2 c^2}\tilde{\mathbf{A}}_0 \cdot \left[\mathbf{A}_1(\mathbf{k} - \mathbf{k}_0, \omega - \omega_0) + \mathbf{A}_1(\mathbf{k} + \mathbf{k}_0, \omega + \omega_0)\right]. \tag{2.78}$$

Inserting Eq. (2.77) into Eq. (2.78) we find the dispersion relation

$$\omega^2 - 3v_{the}^2 k^2 - \omega_{pe}^2 = \frac{\omega_{pe}^2 c^2 k^2}{4}\frac{e^2 \tilde{\mathbf{A}}_0^2}{m_e^2 c^4}\left(\frac{1}{D_-} + \frac{1}{D_+}\right), \tag{2.79}$$

where contributions $n_{e1} \left(\mathbf{k} \pm 2\mathbf{k}_0, \omega \pm 2\omega_0 \right)$ are neglected as nonresonant and $D_{\pm} = \left(\omega \pm \omega_0 \right)^2 - c^2 \left(\mathbf{k} \pm \mathbf{k}_0 \right)^2 - \omega_{pe}^2$. We note that the left-hand-side of Eq. (2.79) is the dispersion relation of Langmuir waves (2.35). D_+ and D_- are the dispersion relations for light waves in plasma upshifted and downshifted, respectively, in frequency and wavenumber. The term $e\tilde{\mathbf{A}}_0/m_e c^2$ is often abbreviated via

$$a_0 = \frac{e|\tilde{\mathbf{A}}_0|}{m_e c^2}, \tag{2.80}$$

the dimensionless pump amplitude. Throughout the work at hand we will often refer to this value a_0 as it is a crucial parameter for laser plasma interaction. Recalling the transverse component of the momentum balance leading to $\mathbf{u}_t = e\mathbf{A}/m_e c$, $a_0 = |\mathbf{u}_t|/c$ can be interpreted as the fraction of the speed of light with which electrons oscillate. However, the last two statements only hold true in the nonrelativistic case $|\mathbf{u}_t| \ll c$, as a_0 can be larger than 1 since it only defines the laser amplitude. The dimensionless value a_0 has the same value as the dimensionless electric field amplitude $E_0/m_e c\omega_0$, hence it is a very useful parameter. One usually distinguishes three regimes: $a_0 \ll 1$ defines the nonrelativistic regime, $a_0 \lesssim 1$ is called weakly relativistic and for $a_0 \gtrsim 1$ a full relativistic treatment becomes necessary.

In this work, we mostly stick to nonrelativistic laser amplitudes, as the diameter of pulses used for Brillouin amplification is typically large, i.e. the local amplitude low. This way one mitigates unwanted relativistic effects, e.g. self-focusing, see Sec. 2.3.2. Sometimes we operate in the weakly relativistic regime, where the relativistic Lorentz factor can be approximated via its Taylor expansion in the first two terms.

Coming back to the Raman scattering dispersion relation Eq. (2.79), we want to find the wavenumber, where maximum growth occurs. We can neglect the upshifted wave as nonresonant and downshifted as highly resonant [41], i.e. $D_- \approx 0$, which lets us write

$$D_- \left(\omega^2 - \omega_L^2 \right) = \frac{\omega_{pe}^2 c^2 k^2 a_0^2}{4}, \tag{2.81}$$

where we have introduced $\omega_L^2 = 3v_{the}^2 k^2 + \omega_{pe}^2$ for convenience. We state $\omega = \omega_L + \Delta\omega$ with $\Delta\omega \ll \omega_L$, i.e. the scattered plasma wave is a slightly changed Langmuir wave assumed to be resonant $\left(\omega_L - \omega_0 \right)^2 \approx c^2 \left(\mathbf{k} - \mathbf{k}_0 \right)^2 + \omega_{pe}^2$. Hence, we find $D_- \approx 2\Delta\omega \left(\omega_L - \omega_0 \right)$. Solving Eq. (2.81) for $\Delta\omega$, keeping in mind that it is small, we have

$$\Delta\omega \approx \frac{\omega_{pe} c k a_0}{4} \sqrt{\frac{1}{\omega_L \left(\omega_L - \omega_0 \right)}}. \tag{2.82}$$

We note $\omega_L \ll \omega_0$, i.e. a negative radicant in Eq. (2.82). Finally, we rewrite

$\Delta\omega = i\Gamma$ and constitute

$$\Gamma_{\text{Raman}} \approx \frac{\omega_{pe} c k a_0}{4} \sqrt{\frac{1}{\omega_L (\omega_0 - \omega_L)}} \tag{2.83}$$

as the growth rate for Raman backscattering. We note that it scales linearly with a_0. Solving the resonance condition for the scattered plasma wave, we find

$$k_{\text{Raman}} \approx k_0 + \frac{\omega_0}{c} \sqrt{1 - 2\frac{\omega_{pe}}{\omega_0}} \tag{2.84}$$

as the wavenumber at which maximum growth occurs. We note $k_{\text{Raman}} \approx 2k_0$ for $n_0/n_c \ll 0.25$ and $k_{\text{Raman}} \approx k_0$ for $n_0/n_c \approx 0.25$ as the two limits.

Brillouin scattering

Brillouin scattering is the decay of a photon into a different photon and an ion acoustic phonon. Also for this process, energy and momentum conservation (Eqs. (2.65) and (2.66)) hold true. Since the ion acoustic frequency is much lower than the laser frequency $kc_s \ll \omega_0$, the process can occur for every plasma density $n_0 \leq n_c$. It also implies that almost all energy of the incident photon will be transferred to the scattered photon.

Deriving the model for Brillouin scattering we follow a similar approach as in the previous section, i.e. considering homogeneous plasma radiated by a strong laser field. In fact, Eq. (2.71) holds true also in the case of Brillouin scattering, neglecting the ion contribution on the right-hand-side as they are much heavier. The search for the equation describing the density oscillation is analog to what was presented in Sec. 2.1.3. We again separate the electron velocity into longitudinal and transverse part via $\mathbf{u} = \mathbf{u}_l + \mathbf{u}_t$. With $\mathbf{u}_t = e\mathbf{A}/m_e c$, following from the transverse part of the momentum balance, we find again Eq. (2.72). Now we assume the electrons to follow isothermal behavior $P_e = n_e k_B T_e$ and linearize $n_e = n_0 + \epsilon n_{e1}$ $\mathbf{A} = \mathbf{A}_0 + \epsilon \mathbf{A}_1$ and $\phi = \epsilon\phi_1$ to obtain to first order in ϵ

$$\frac{e}{m_e}\nabla\phi_1 = \frac{e^2}{m_e^2 c^2}\nabla(\mathbf{A}_0 \cdot \mathbf{A}_1) + \frac{v_{the}^2}{n_0}\nabla n_{e1}. \qquad (2.85)$$

Defining $n_i = n_{i0} + \epsilon n_{i1}$, $\mathbf{u}_i = \epsilon\mathbf{u}_{i1}$ and $\phi = \epsilon\phi_1$, continuity equation (2.10) and momentum balance (2.11) for ions become

$$\frac{\partial n_{i1}}{\partial t} + n_{i0}\nabla \cdot \mathbf{u}_{i1} = 0, \qquad (2.86)$$

$$\frac{\partial \mathbf{u}_{i1}}{\partial t} = -\frac{Ze}{m_i}\nabla\phi_1, \qquad (2.87)$$

again to first order in ϵ. Deriving Eq. (2.86) with respect to time and taking the divergence $\nabla\cdot$ of Eq. (2.87) we find

$$\frac{\partial^2 n_{i1}}{\partial t^2} - \frac{Zen_{i0}}{m_i}\nabla^2\phi_1 = 0. \qquad (2.88)$$

Considering $Zn_{i0} = n_0$ and $Zn_{i1} \approx n_{e1}$ for the same arguments as in Sec. 2.1.3, plugging Eq. (2.88) into Eq. (2.85) results in

$$\left(\frac{\partial^2}{\partial t^2} - c_s^2\nabla^2\right)n_{e1}^2 = \frac{Ze^2 n_0}{m_e m_i c^2}\nabla^2(\mathbf{A}_0 \cdot \mathbf{A}_1). \qquad (2.89)$$

Thus, the coupled system of equations describing Brillouin scattering consists of Eqs. (2.71) and (2.89). Note that again these equations also represent a parametric oscillator as it was discussed for Raman scattering above.

Deriving the dispersion relation we follow an approach analog to the Raman case, considering a plane wave $\mathbf{A}_0 = \tilde{\mathbf{A}}_0 \cos (\mathbf{k}_0 \cdot \mathbf{x} - \omega_0 t)$ and Fourier transform Eqs. (2.71) and (2.89) to find

$$
\left(\omega^2 - c^2 k^2 - \omega_{pe}^2\right) \mathbf{A}_1 (k, \omega) =
$$
$$
\frac{4\pi e^2 \tilde{\mathbf{A}}_0}{2m_e} \left[n_{e1} (k - k_0, \omega - \omega_0) + n_{e1} (k + k_0, \omega + \omega_0)\right], \qquad (2.90)
$$
$$
\left(\omega^2 - c_s^2 k^2\right) n_{e1} (k, \omega) =
$$
$$
\frac{Z n_0 e^2 k^2 \tilde{\mathbf{A}}_0}{2 m_e m_i c^2} \cdot \left[\mathbf{A}_1 (k - k_0, \omega - \omega_0) + \mathbf{A}_1 (k + k_0, \omega + \omega_0)\right]. \qquad (2.91)
$$

Again neglecting non resonant terms and recalling $\omega \ll \omega_0$ we combine Eqs. (2.90) and (2.91) to the Brillouin dispersion relation

$$
\omega^2 - c_s^2 k^2 = \frac{c^2 k^2 a_0^2 \omega_{pi}^2}{4} \left(\frac{1}{D_-} + \frac{1}{D_+}\right), \qquad (2.92)
$$

where $\omega_{pi} = \sqrt{Z m_e / m_i} \, \omega_{pe}$ is the ion plasma frequency.

Similar to Raman scattering, we note resonance with the downshifted wave $D_- \approx 0$, i.e. rewriting Eq. (2.92) into

$$
\left(\omega^2 - c_s^2 k^2\right) \left(\omega^2 - 2\omega \omega_0 + 2c^2 \mathbf{k}_0 \cdot \mathbf{k} - c^2 \mathbf{k}^2\right) = \frac{c^2 k^2 a_0^2}{4} \omega_{pi}^2. \qquad (2.93)
$$

Stating $\omega = k c_s + i\Gamma$, where $\Gamma \ll k c_s$ and assuming resonance in the plasma wave we find

$$
\Gamma_{\text{Brillouin}} = \frac{1}{2\sqrt{2}} \frac{c k_0 a_0 \omega_{pi}}{\sqrt{c_s k_0 \omega_0}}, \qquad (2.94)
$$

as the maximum growth rate, which resides at wavenumber

$$
k_{\text{Brillouin}} = 2k_0 - 2\frac{\omega_0 c_s}{c^2}. \qquad (2.95)
$$

We remark that the Brillouin instability growth rate is proportional to the dimensionless vector amplitude $\Gamma_{\text{Brillouin}} \propto a_0$ and the wavenumber is given by $k_{\text{Brillouin}} \approx 2k_0$. Recalling momentum conservation Eq. (2.66), the latter implies $k_0 \approx -k_1$, i.e. the absolute wavenumbers of incident and scattered light wave are almost the same. The value $2\omega_0 c_s / c^2$ is sometimes defined as δk_{wc} and will play an important role in Ch. 5.

Strong coupling regime

The strong coupling regime is defined through the light amplitude a_0. If the ponderomotive pressure due to the laser exceeds the electrostatic (Raman) or thermal (Brillouin) pressure by far, we find a frequency $|\omega| \gg \omega_\Re$. In particular, $|\omega| \gg \omega_{pe}$ for Raman and $|\omega| \gg c_s k$ for Brillouin scattering. This means that we expect a much higher frequency than what is given by a Langmuir or ion acoustic mode, respectively. Therefore, the plasma mode off which light scatters is no longer an eigenmode of the plasma, but a driven quasi-mode which only exists in the presence of the laser. In this part we will derive the strong coupling limit for Brillouin scattering, as here it is relevant and for Raman it is not, as we will show in the subsequent section.

Considering $\omega_0 \gg |\omega| \gg c_s k$ and assuming $k \approx 2k_0$, Eq. (2.93) becomes

$$\omega^3 \approx -\frac{c^2 k_0^2 a_0^2}{2} \frac{\omega_{pi}^2}{\omega_0}. \tag{2.96}$$

Looking for the solution of Eq. (2.96) with the largest imaginary part, we find

$$\omega \approx \left(\frac{c^2 k_0^2 a_0^2}{2} \frac{\omega_{pi}^2}{\omega_0} \right)^{1/3} \left(\frac{1}{2} + \mathrm{i} \frac{\sqrt{3}}{2} \right). \tag{2.97}$$

Via $\omega = \omega_\Re + \mathrm{i}\Gamma$ we distinguish the growth rate to be

$$\Gamma_{\mathrm{Brillouin}}^{\mathrm{sc}} = \frac{\sqrt{3}}{2} \left(\frac{c^2 k_0^2 a_0^2}{2} \frac{\omega_{pi}^2}{\omega_0} \right)^{1/3}, \tag{2.98}$$

i.e. proportional to $a_0^{2/3}$.

Comparing the strong coupling growth rate to the weak coupling one, we find that the latter scales linearly in a_0, thus has preferable dependence. However, the condition for entering strong coupling $|\omega| \gg c_s k$ is linked to the vector amplitude a_0 and thus to the laser intensity via

$$I_{14} \gg 0.44 \sqrt{\frac{Z}{A} \frac{n_c}{n_0}} \sqrt{1 - \frac{n_0}{n_c}} \left(T_e/\mathrm{keV} \right)^{3/2} \left(\lambda/\mu\mathrm{m} \right)^{-2}, \ \text{or} \ a_0 \gg \sqrt{\frac{16\omega_0^2 c_s^3}{\omega_{pi}^2 c^3}}. \tag{2.99}$$

Here, I_{14} is the intensity in units of 10^{14} W/cm^2 and A is the atomic number. The intensity and dimensionless vector amplitude are related via $I/\left(\mathrm{W/cm}^2 \right) \equiv a_0^2/\left(7.3 \cdot 10^{-19} \left(\lambda/\mu\mathrm{m} \right)^2 \right)$ [54, 58, 63]. By the choice of the laser-plasma parameters one chooses the regime in which the interaction takes place. Ch. 5 is devoted to the analysis of both different regimes and in particular the transition between the two.

In the next subsection we sum up the aforementioned Raman and Brillouin scattering and additionally focus on different scattering mechanisms altering the amplification scheme.

Different scattering mechanisms

In the previous Subsecs. we derived the dispersion relations and growth rates for Raman, Brillouin and strongly coupled Brillouin scattering. If a_0 is strong enough it does not trigger an eigenmode but a quasi-mode of the plasma with higher frequency. We have $|\omega|^2 \gg \omega_{pe}^2 + 3k^2 v_{th,e}^2$ in case of Raman or $|\omega| \gg kc_s$ in case of Brillouin scattering. This is the case when the ponderomotive potential exceeds the electrostatic or thermal pressure, respectively. These are the forces counteracting each other for Raman and Brillouin.

This regime is referred to as strongly coupled and in order to reach it the pump amplitude needs to exceed the thresholds $a_0 \gg 8^{1/2}(n_e/n_c)^{1/4}$ for Raman [40] or $a_0 \gg (16\omega_0^2 c_s^3/(\omega_{pi}^2 c^3))^{1/2}$ for Brillouin [41]. The latter condition is equivalent to Eq. (2.99). For a higher density the electrostatic potential is higher, it is thus more difficult to enter strongly coupled Raman. Simultaneously, the current induced by the ponderomotive force is higher, which is why strongly coupled Brillouin is accessed.

When the interaction is strongly coupled the frequency and growth rate Γ of the plasma wave depend only on the pump strength a_0 and no longer on the electron temperature T_e.

If both laser amplitudes are sufficiently large, such that electron motion is no longer determined by the space charge electric field of the plasma wave but directly by the ponderomotive force, we speak of *superradiant amplification* (SRA). This regime is accessible if $a_0 a_1 > n_e/4n_c$ [91], where a_1 denotes the dimensionless seed strength.

If the respective plasma wave is driven too strongly it can break which may prevent or at least completely alter the amplification. For Langmuir waves we expect *wave breaking* (WB) if we pump above $a_0 > (n_e/n_c)^{3/4}/4$ [32] while for ion acoustic waves the threshold is given via $a_0 > (\sqrt{m_i/m_e} v_{th,e} n_e/(4cn_c))^{1/2}$.

Fig. 2.4 shows the thresholds of a_0 above which one of the three different regimes dominates the interaction in dependency of n_e/n_c. The SRA threshold is calculated for a fixed seed strength a_1. In Subfig. 2.4a one finds the limits for Raman, in Subfig. 2.4b for Brillouin amplification. Below the thresholds we expect weakly coupled amplification.

For the chosen seed amplitude of $a_1 = 0.3$ either SRA (red dashed) or Langmuir WB (green dotted) is the dominant process that alters the usual Raman scattering off electrostatic Langmuir waves above a certain pump strength. Additionally, one finds that strongly coupled stimulated Raman scattering (scSRS) cannot be reached directly from weak coupling. In Subfig. 2.4b we see that for Brillouin with

$a_1 = 0.02$ all three regimes are accessible depending on the chosen density. This is a strong evidence that strongly coupled stimulated Brillouin scattering (scSBS) is an important mechanism which deserves interest. However, the thresholds presented are only valid for a transition from weak coupling to a different regime. For a transition from e.g. wave breaking into strong coupling the threshold may vary.

In conclusion, we find strong coupling being one of the very relevant effects for Brillouin amplification and playing a negligible role for Raman scattering.
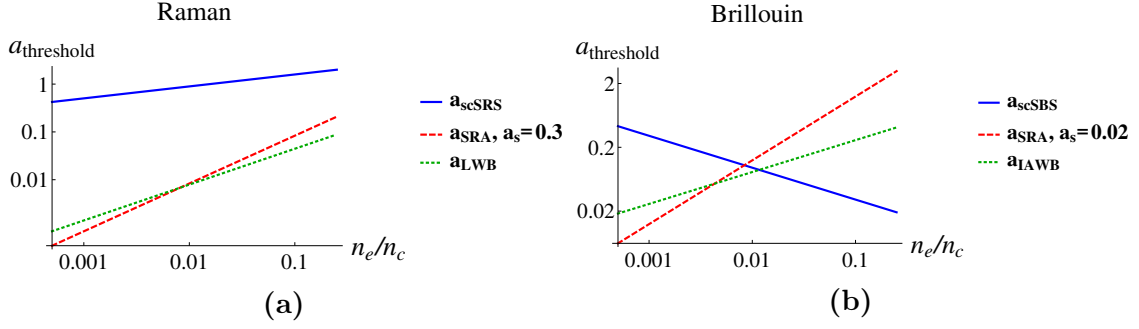
Figure 2.4: Threshold values for dimensionless pump strength a_0 above which strongly coupled Raman/Brillouin (blue), super radiant amplification (dashed red) or wave breaking (dotted green) set in vs. electron density in units of the critical density. The SRA regime can be reached if a_1 exceeds a_0, here a_1 was chosen as specified in the legends. Below the lines we expect weak coupling.

3 Simulation tools and principles of Brillouin amplification

In this chapter we introduce the simulation techniques used throughout the thesis. Even though it might not seem so, the choice of the theoretical model best suited for simulation is a difficult one. The obvious choice would be to simulate Maxwell's equations (2.1)-(2.4) for all free particles. Considering in plasmas we have to deal with roughly 10^{20} particles, this idea can quickly be dropped, as none of todays supercomputers could handle that vast amount of calculus. On the other hand, if one distinguished process is studied it may not even be proper to incorporate all other effects coexisting with the one investigated.

As the choice of the model is crucial, it is also fundamental for theory to question itself. One possible way to underline results obtained from simulation is to back them up with analytic models or further simulations with different codes. The best way possible is of course to have experiments confirming theoretical predictions.

The flavors of codes typically used in laser-plasma interaction underly a hierarchy, we will very briefly introduce them. One of the most general codes relies on solving Maxwell's equations and the Vlasov equation (2.7) [50, 51]. A bit more general and noise affected are so called PIC (particle in cell) models: here, many particles are treated as one large particle compound. Maxwell's equations are solved on a grid and these simulation schemes are most widely spread. In Ch. 7 we use the PIC code EPOCH [85, 86]. It is also possible to incorporate collisions, relativistic and quantum mechanical processes in these models, furtherly complicating them.

More specific codes are the ones used in this thesis. In the next Sec. 3.1 we introduce two different kinds, being derived from continuity equation (2.10), momentum balance (2.11) and Maxwell's equations (2.5), implemented in a self-written C++ code using the PETSc library [83, 84].

To give the reader a deeper understanding of the amplification process, we exemplarily show simulation results in Sec. 3.2. Here, we highlight the differences between weakly and strongly coupled Brillouin scattering and discuss growth in both the linear and the pump depletion regime.

3.1 $\delta N\mathbf{A}$- and envelope model

It is a general goal of theory to find fast and reliable simulation tools including as many physical effects as necessary to resolve complex dynamics. In this section we derive the major two plasma models used throughout the thesis. The first, quite general one, is the $\delta N\mathbf{A}$-model, consisting of continuity equation (2.10), momentum balance (2.11) and the Maxwell equation in potential form (2.6). A further simplification leads to the slowly-varying-envelope approximation, i.e. making use of the rapidly oscillating electric field varying much faster than the pulse envelope. In the latter scenario we find three wave interaction models.

For performance reasons we want to find simulation models that are less noisy and faster than PIC and still deliver correct predictions. Possible candidates are envelope models which do not resolve the rapidly oscillating electric field. They are widely used and have delivered promising results, e.g. [50]. However, so far these envelope models were only able to cover either weak or strong coupling Brillouin amplification but not both. We derive a more general envelope model which we benchmark with Maxwell-Fluid, hence $\delta N\mathbf{A}$ simulations. Since in experiments the beam diameters are large in order to evade relativistic effects, we can stick to the one-dimensional case and the peak intensities are rather low.

We consider the Maxwell equation in Lorenz gauge (2.6)

$$\left(\frac{1}{c^2}\frac{\partial^2}{\partial t^2} - \nabla^2\right)\mathbf{A} = \frac{4\pi}{c}\mathbf{j}, \tag{3.1}$$

with $\mathbf{j} \approx -n_e e\mathbf{p}/m_e$ being the current with the electron density n_e, the elementary charge and electron rest mass e and m_e and the electron momentum $\mathbf{p}$, where $\mathbf{p}_\perp \gg \mathbf{p}_\parallel$ is assumed. c denotes the speed of light and $\mathbf{A}$ the electromagnetic vector potential. A solution to the transverse part of the electron momentum balance is $\mathbf{p}_\perp = e\mathbf{A}/c$. By introducing $n_e = n_0 + \delta n$, where n_0 is the unperturbed background density and δn a small deviation we arrive at

$$\left(\frac{\partial^2}{\partial t^2} - c^2\nabla^2\right)\mathbf{A} = -\omega_{pe}^2\left(1 + \frac{\delta n}{n_0}\right)\mathbf{A}. \tag{3.2}$$

We assume low frequency electrons driving the ions isothermally $n_e \approx n_i$ which is a legitimate approximation when investigating Brillouin scattering [51]. Here, we imply $Z = 1$, i.e. a Hydrogen plasma. When we combine the continuity equation with the longitudinal part of the electron momentum balance we find the density wave equation

$$\left(\frac{\partial^2}{\partial t^2} - c_s^2\nabla^2\right)\frac{\delta n}{n_0} = \frac{Ze^2}{2m_e m_i c^2}\nabla^2\mathbf{A}^2. \tag{3.3}$$

Introducing the new variable $\delta N = \delta n/n_0$ and the new units $[t] = 1/\omega_{pe}$, $[x] = c/\omega_{pe}$ and $[\mathbf{A}] = m_e c^2/e$ delivers the $\delta N\mathbf{A}$-model. We used one-dimensional geometry with $\mathbf{A} = \mathbf{A}(x,t)$ and $\delta N = \delta N(x,t)$.

$$\left(\frac{\partial^2}{\partial t^2} - \frac{\partial^2}{\partial x^2}\right)\mathbf{A} = -\left(1 + \delta N\right)\mathbf{A}, \tag{3.4}$$

$$\left(\frac{\partial^2}{\partial t^2} - \frac{c_s^2}{c^2}\frac{\partial^2}{\partial x^2}\right)\delta N = \nu\frac{\partial^2}{\partial x^2}\mathbf{A}^2, \tag{3.5}$$

where $\nu = Zm_e/(2m_i)$ is the residual coupling coefficient. We remark that Eqs. (3.4)-(3.5) is in dimensionless form.

When looking for a three-wave model we first split $\mathbf{A} = \mathbf{A}_0 + \mathbf{A}_1$, just like we did in Sec. 2.3.2 and assume three waves

$$\mathbf{A}_0 = \frac{1}{2}\left(a_0 e^{i\phi_0} + a_0^* e^{-i\phi_0}\right)\mathbf{y}, \qquad \phi_0 = \frac{ck_0}{\omega_{pe}}x - \frac{\omega_0}{\omega_{pe}}t, \tag{3.6}$$

$$\mathbf{A}_1 = \frac{1}{2}\left(a_1 e^{i\phi_1} + a_1^* e^{-i\phi_1}\right)\mathbf{y}, \qquad \phi_1 = -\frac{ck_1}{\omega_{pe}}x - \frac{\omega_1}{\omega_{pe}}t, \tag{3.7}$$

$$\delta N = \frac{1}{2}\left(n e^{i\phi_2} + n^* e^{-i\phi_2}\right), \qquad \phi_2 = \frac{ck_2}{\omega_{pe}}x - \frac{\omega_2}{\omega_{pe}}t, \tag{3.8}$$

in dimensionless units, where $\mathbf{y}$ is the unit vector in y-direction, $a_{0,1}$ and n complex envelopes in which additional phase information is stored. $\phi_{0,1,2}$ are the (fixed) rapid oscillations with wavenumbers $k_{0,1}$ of pump and seed, respectively, in plasma. Thus, the pump pulse is propagating from left to right and the seed vice versa. We choose energy and momentum balance such that $\phi_0 = \phi_1 + \phi_2$, thus $\omega_0 = \omega_1 + \omega_2$ and $k_0 + k_1 = k_2$ and only consider resonant terms. Hence, from Eq. (3.4) we can derive an equation for a_0 and a_1 each. The model then reads

$$\left(\frac{\partial^2}{\partial t^2} - 2i\frac{\omega_0}{\omega_{pe}}\frac{\partial}{\partial t} - \frac{\omega_0^2}{\omega_{pe}^2} - \frac{\partial^2}{\partial x^2} - 2i\frac{ck_0}{\omega_{pe}}\frac{\partial}{\partial x} + \frac{c^2 k_0^{p2}}{\omega_{pe}^2} + 1\right)a_0 = -\frac{1}{2}a_1 n, \tag{3.9}$$

$$\left(\frac{\partial^2}{\partial t^2} - 2i\frac{\omega_1}{\omega_{pe}}\frac{\partial}{\partial t} - \frac{\omega_1^2}{\omega_{pe}^2} - \frac{\partial^2}{\partial x^2} + 2i\frac{ck_1}{\omega_{pe}}\frac{\partial}{\partial x} + \frac{c^2 k_1^{p2}}{\omega_{pe}^2} + 1\right)a_1 = -\frac{1}{2}a_0 n^*, \tag{3.10}$$

$$\left(\frac{\partial^2}{\partial t^2} - 2i\frac{\omega_2}{\omega_{pe}}\frac{\partial}{\partial t} - \frac{\omega_2^2}{\omega_{pe}^2} - \frac{c_s^2}{c^2}\frac{\partial^2}{\partial x^2} - 2i\frac{c_s^2 k_2}{c\omega_{pe}}\frac{\partial}{\partial x} + \frac{c_s^2 k_2^2}{\omega_{pe}^2}\right)n =$$
$$-\frac{Zm_e c^2\left(k_0^p + k_1^p\right)^2}{2m_i\omega_{pe}^2}a_0 a_1^*, \tag{3.11}$$

where we assumed the second derivative with respect to x on the right-hand-side of Eq. (3.5) being much larger applied to the rapid phase $e^{i\phi_2}$ than to the amplitudes $a_0 a_1^*$. We state that the dispersion relations for light in plasma $\omega_{0,1}^2 = c^2 k_{0,1}^2 + \omega_{pe}^2$ and ion acoustic waves $\omega_2 = c_s k_2$ hold. Subsequently, we make the slowly varying

envelope approximation for the two light waves $||\partial_t|| \ll ||2\omega_{0,1}/\omega_{pe}||$ and $||\partial_x|| \ll ||2ck_{0,1}/\omega_{pe}||$ in order to arrive at

$$\left(\frac{\partial}{\partial t} + \frac{ck_0}{\omega_0}\frac{\partial}{\partial x}\right) a_0 = -\mathrm{i}\frac{\omega_{pe}}{4\omega_0}a_1 n, \tag{3.12}$$

$$\left(\frac{\partial}{\partial t} - \frac{ck_1}{\omega_1}\frac{\partial}{\partial x}\right) a_1 = -\mathrm{i}\frac{\omega_{pe}}{4\omega_1}a_0 n^*, \tag{3.13}$$

$$\left(\frac{\partial^2}{\partial t^2} - 2\mathrm{i}\frac{\omega_2}{\omega_{pe}}\frac{\partial}{\partial t} - \frac{c_s^2}{c^2}\frac{\partial^2}{\partial x^2} - 2\mathrm{i}\frac{c_s^2 k_2}{c\omega_{pe}}\frac{\partial}{\partial x}\right) n = -\frac{Zm_e c^2 k_2^2}{2m_i\omega_{pe}^2}a_0 a_1^*, \tag{3.14}$$

which is the three-wave model in the same units as the $\delta N\mathbf{A}$-model (3.4)-(3.5). We now introduce new units in order to arrive at the same scaling as Guzdar et. al [54].

We transform into the new units $[t]_2 = 1/\gamma_0$, where $\gamma_0 = \sqrt{3}/2 \left(k_0^2 a_0^2 c^2 \omega_{pi}^2/(2\omega_0)\right)^{1/3}$ is the strongly coupled growth rate (see Sec. 2.3.2), $[x]_2 = [t]_2\, c^2 k_0/\omega_0$, rewrite $a_{0,1} = E_{0,1}\,[E_{0,1}]\,e/(m_e c\omega_0)$ with $[E_1] = 2\sqrt{2\omega_0^3\omega_2 m_e m_i c^2\gamma_0^2/\left(c^2 k_2^2\omega_{pe}^2 Ze^2\right)}$ and $[E_0] = \sqrt{\omega_1/\omega_0}\,[E_1]$, respectively and scale the density wave via $n = 4\sqrt{\omega_0\omega_1}\gamma_0/\omega_{pe}^2 N$.

In order to arrive at the new system we therefore change $\partial_t \to \gamma_0/\omega_{pe}\partial_t$, $\partial_x \to \gamma_0\omega_0/(ck_0\omega_{pe})\partial_x$, $n \to 4\sqrt{\omega_0\omega_1}\gamma_0/\omega_{pe}^2 N$, $a_1 \to 2\sqrt{2\omega_0\omega_2\gamma_0^2 m_i/\left(Zc^2 k_2^2\omega_{pe}^2 m_e\right)}E_1$ and $a_0 \to 2\sqrt{2\omega_1\omega_2\gamma_0^2 m_i/\left(Zc^2 k_2^2\omega_{pe}^2 m_e\right)}E_0$ in Eqs. (3.12)-(3.14) and find

$$\left(\frac{\partial}{\partial t} + \frac{\partial}{\partial x}\right) E_0 = -\mathrm{i}N E_1, \tag{3.15}$$

$$\left(\frac{\partial}{\partial t} - \theta\frac{\partial}{\partial x}\right) E_1 = -\mathrm{i}N^* E_0, \tag{3.16}$$

$$\left(\epsilon\frac{\partial^2}{\partial t^2} - 2\mathrm{i}\frac{\partial}{\partial t}\right) N = -E_0 E_1^*, \tag{3.17}$$

where we neglected the derivatives with respect to x in Eq. (3.17), θ being the phase velocity ratio $\theta = |v_{ph,0}|/|v_{ph,1}| \approx 1$ and the coefficient

$$\epsilon = \gamma_0/\omega_2, \tag{3.18}$$

where ω_2 is still a free parameter we choose to be $\omega_2 = 2k_0 c_s$. We note that $\epsilon = \epsilon(a_0)$ depends on the local pump amplitude a_0, however, for simulations we ignore the change of a_0 and set $\epsilon \neq \epsilon(a_0)$ constant with the initial pump amplitude a_0^0. Furthermore, we note that ϵ is the crucial factor if we compare the model (3.15)-(3.17) to previous ones [69]. It determines whether we are in the weak coupling $\epsilon \approx 0$, strong coupling $\epsilon \gg 1$ or the transition regime $\epsilon \approx 1$. It is the ratio of the strongly coupled growth rate $\gamma_0 \approx \omega_{sc}$ to the weakly coupled frequency $\omega_2 \approx \omega_{wc}$, as they were derived in Sec. 2.3.2.

3.2 Characteristics of weakly and strongly coupled Brillouin amplification

In this section we show some characteristics of weakly and strongly coupled Brillouin amplification to ease the reader's understanding throughout the following, more specialized chapters. As the latter regime is more relevant in today's research, we focus on this, however, many basics are similar between the two. A deeper comparison, including the transition of one regime to the other, is done in Ch. 5. In Sec. 2.3.2 we already mentioned that the pump strength a_0 determines whether the interaction takes place weakly or strongly coupled. For now we only assume local intensities high enough that we are always in the strong coupling regime and shift back a more detailed distinction to Ch. 5.

From many other publications [50, 61, 62] we know that via omitting the first derivative with respect to time in Eq. (3.17), the model Eqs. (3.15)-(3.17) solely describes strongly coupled Brillouin amplification and vice versa. As already mentioned before, one distinguishes between different regimes depending on how long the amplification process takes place.

In a first phase, where the high energetic pump is still much larger in amplitude than the seed, the former will stay unaffected by its loss of photons and the seed will grow exponentially. We call this the linear regime, as effectively Eq. (3.15) can be neglected because the pump is unchanged. Here, the growth rates derived in Sec. (2.3.2) are applicable.

After some time, when the amplitudes of both seed and pump are of comparable size, we can no longer neglect the loss of photons of the pump. This implies that we have to incorporate Eq. (3.15) in our model. As the main energy flow still continues from pump to seed, the pump eventually depletes. That is the reason why we call this the pump depletion or nonlinear regime. Hereby, the seed envelope shape develops oscillations and peak amplitude growth continues in a polynomial way instead of exponential. There is also an analytic way to describe the seed envelope in this regime, because it follows self-similar behavior. For more details on self-similarity, see e.g. [44, 45] for Raman or [50, 55] for Brillouin amplification. The appendix A.2 is completely dedicated to investigate a more general self-similar solution applicable for both weakly and strongly coupled regime. However, the above cited solutions are able to predict growth and form of the seed in the nonlinear regime quantitatively which was not possible with the general solution in appendix A.2. Here, the arguments drawn are of qualitative nature.

Fig. 3.1 exemplarily shows the different stages of an amplified seed in a plasma with one percent critical density $n_e = 0.01 n_c$, corresponding to $n_e \approx 1.7 \cdot 10^{19}$ cm^{-3} being pumped by a constant intensity $I_0 = 10^{16}$ W/cm^2, corresponding to $E_0 \approx 0.07$, being well above the threshold for strong coupling as $E_{\text{thresh}} \approx 0.01$ at wavelength $\lambda_0 = 800$ nm. We discuss two different Gaussian seeds, carrying

the same total energy but differ in duration. In solid black we show a seed of 50 fs duration and $I_1 = 10^{14}$ W/cm^2 peak intensity, in dashed black a seed of 1 ps duration (both FWHM) and $I_1 = 5 \cdot 10^{12}$ W/cm^2.
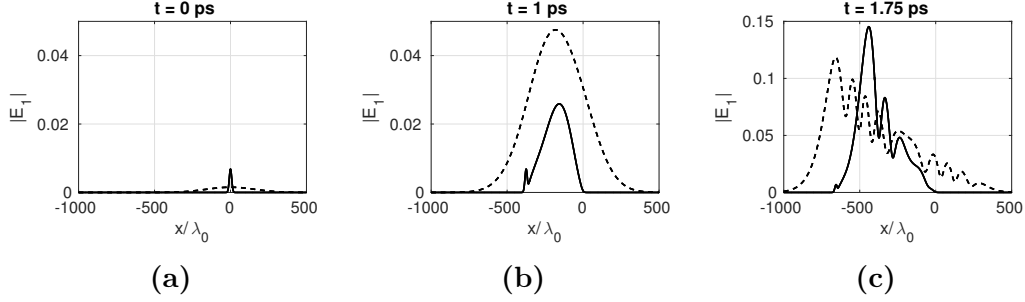

Figure 3.1: Simulation results for model (3.15)-(3.17) for two different seed pulses (long in dashed black, short in solid black) carrying the same energy in a setup with parameters described in text. First, the initial seeds are shown in (a), then after the linear regime (b) and eventually in pump depletion (c). Explanations of pulse shape and peak amplitude are given in the text.

Subfig. 3.1a shows the initial setups of the two seeds described above, traveling from right-to-left. Note that the duration mentioned above directly translates to the spatial width presented here. Furthermore, we remark the aforementioned dependence $I \propto E^2$. The y-axis in Fig. 3.1 shows E_1 instead of I_1, i.e. the factor of 20 in peak intensity between the two seeds translates to a factor of $\sqrt{20} \approx 4.5$ in peak amplitude.

In Subfig. 3.1b the seed pulses approach the pump amplitude $E_0 \approx 0.07$, but until here, the pump (not shown) is almost unchanged. This is the situation after 1 ps of constant pumping at the end of the linear regime. We note that the two different pulses have not only moved, but got amplified differently: The initially short pulse has drawn a tail which then got amplified, the initially long pulse got directly amplified to a higher peak amplitude than its counterpart.

Note that in Subfig. 3.1c the y-axis scaling has changed, here, the seed amplitude has surpassed the pumping limit after 1.75 ps. Both seed pulses follow self-similar behavior and develop characteristic oscillations in their envelope trailing a leading maximum. We find these oscillations in the envelope not going down to zero, the explanation is adjourned to Ch. 6.

Notably, the pulse shown in solid black, which was at the end of the linear regime less amplified than the one shown in dashed black, has now surpassed its counterpart in peak amplitude.

We summarize that at the end of the linear regime, the initially long pulse has a higher peak amplitude than the initially short. In the pump depletion regime the

situation is reversed.

The explanation of this requires a look on the situation in Fourier space. The initially short seed pulse will be broader than its counterpart in Fourier space. However, the strongly coupled Brillouin instability also has a certain bandwidth, as is shown in Fig. 3.2 in red.

In case of the long pulse in Subfig. 3.2a, the whole pulse fits into the instability, i.e. all of it gets amplified. In case of the short pulse in Subfig. 3.2b, only the central part of its Fourier transform fits into the instability. That is why it draws a tail at first, as its wings will not experience amplification. This was already explained in [92].
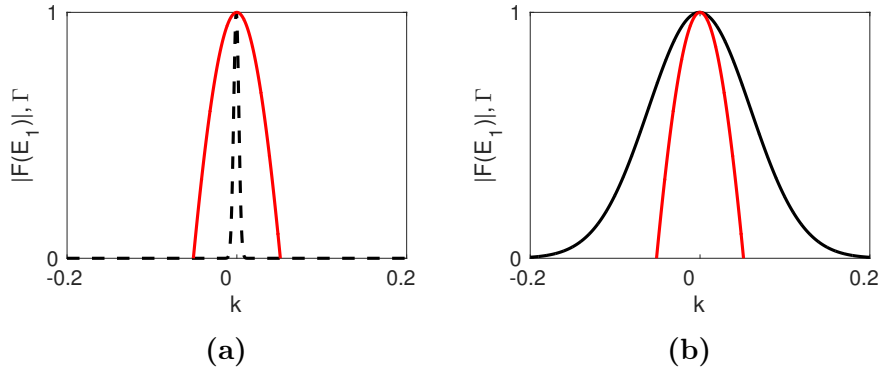
Figure 3.2: Normalized spectra $|F(E_1)|$ of the initial seeds shown in Fig. 3.1a, the short one in solid black in (a) and the long one in dashed black in (b) in k-space. In solid red the normalized bandwidth of the instability is sketched.

Fig. 3.3 shows the peak amplitude of both seed pulses over time, in solid black for the initially short pulse and in dashed black for the initially long seed. The horizontal solid blue line marks the pump amplitude, the dashed vertical blue line roughly separates the two different growth regimes: to its left we see exponential growth of both initial seeds in the linear regime, to the right we see polynomial or algebraic growth in the nonlinear regime.

The dashed-dotted red line is a fit, describing a $\propto t^{3/4}$ behavior. Apparently, the initially short pulse grows in peak amplitude with this behavior. This can be understood with the self-similar analysis [50, 55], where this growth is predicted. For comparison, in weak coupling Brillouin or Raman (not shown), the growth in the nonlinear regime is predicted to be $\propto t$. The initially long pulse apparently has weaker growth in the nonlinear regime.
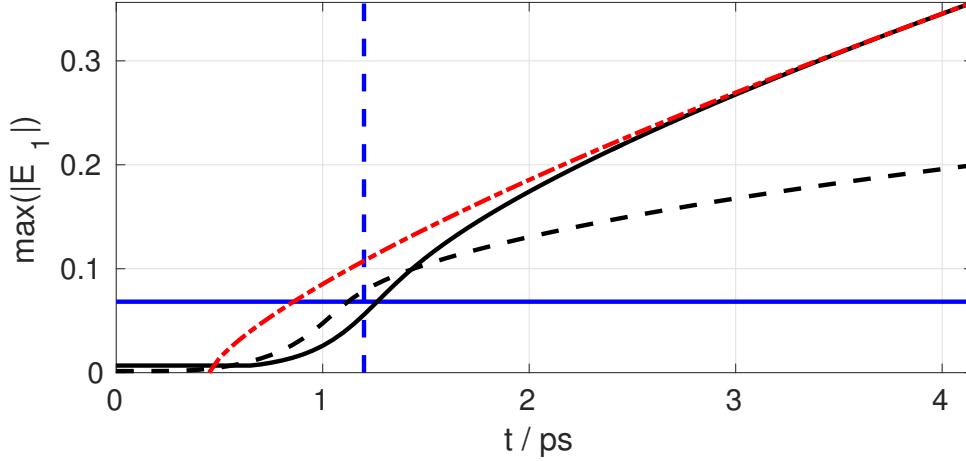
Figure 3.3: Peak amplitude growth for two different seed pulses depicted in Fig.
3.1. In solid black is shown an initially short seed, in dashed black an
initially long seed. The horizontal solid blue line is the pump amplitude,
the vertical dashed blue line separates linear regime (to the left) from
pump depletion regime (to the right). The dashed-dotted red line is
a fit $\propto t^{3/4}$, apparently describing growth of the initially short seed in
the nonlinear regime.

To clarify the qualitative difference between weak and strong coupling besides
the aforementioned different time and length scales, we show Fig. 3.4. Here,
we present simulation results from both the $\delta N\mathbf{A}$-model (in solid-dotted green)
(3.4)-(3.5) and the three wave model (in solid red) (3.15)-(3.17). The parameters
are $n_e = 0.05 n_c$, i.e. $n_e \approx 9 \cdot 10^{19}$ cm^{-3} for the density, an electron temperature
of $T_e = 200$ eV. The seed with $E_s = 0.001$ and a duration of 100 fs is pumped by
either $I_0 \approx 10^{12}$ W/cm^2 in Subfig. 3.4a or $I_0 \approx 10^{16}$ W/cm^2 in Subfig. 3.4b.

(a)

(b)
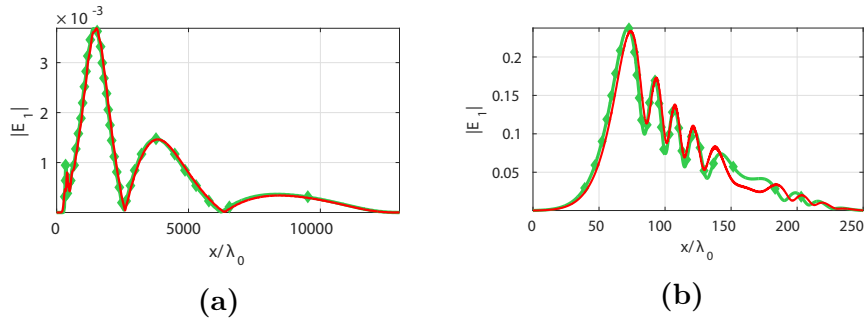
Figure 3.4: Simulation of Eqs. (3.4)-(3.5) (solid-dotted green) and (3.15)-(3.17)
(solid red), respectively, for parameters as specified in text. In (a) the
interaction is weakly coupled, in (b) it is strongly coupled. In both
cases, the two models show good agreement.

In Subfig. 3.4a we see a snapshot of the weakly coupled Brillouin amplification in the pump depletion regime after 60 ps of interaction. The envelope oscillation trailing the leading spike is a deviation from the result shown in Subfig. 3.4b, where a snapshot is shown after 1 ps of interaction in the nonlinear regime of strongly coupled Brillouin amplification. Weakly coupled Brillouin scattering has the characteristic that these oscillations go down to zero. Raman scattering shares this trait. The reason for that is given in Chs. 5 and 6.

In summary, we have illustrated the basic mechanisms and phases of the amplification scenario. We showed the influence of short or long seed pulse durations on the amplification and gave an explanation. Furthermore, we presented the evolution of the amplitude of the leading spike in the interaction. Lastly, we explained the differences between weak and strong coupling to be the final pulse duration, growth behavior in the pump depletion regime and shape of the amplified pulse envelope in the nonlinear regime.

4 Kinetic dispersion for parametric instabilities

The fluid description presented in the previous chapter in Sec. 2.3.2 is one possible way to treat Brillouin scattering in plasma. However, the equations at the basis are not the most general ones. We have seen right in the beginning of Ch. 2, that continuity and momentum equation are a consequence of the Vlasov equation. We showed that in the derivation of Raman and (strong coupling) Brillouin scattering there are assumptions made about the electron and ion fluid, e.g. isothermal and adiabatic equations of state.

The work by Edwards et al. [72] included a fluid description of Brillouin amplification in electron-positron plasmas. Here, they claimed to observe enhanced Brillouin growth. However, the simulations presented showed less growth than what was estimated with analytic models. The terminology *enhanced* is somehow irritating. It is enhanced in comparison to Raman growth, but in fact reduced compared to the electron-proton plasma case, which is only properly possible to investigate if the interaction is treated kinetically.

The goal of this chapter at hand is to derive a dispersion relation for Brillouin amplification, valid in both weak and strong coupling. We consider weakly relativistic amplitudes $a_0 \leq 1$ and arbitrary ion species in a single charge state. With this we can handle both the Hydrogen plasma case that is assumed throughout the course of this thesis and also clarify the disagreement in growth rates between simulation and fluid description in the electron positron case in [72].

Electron-positron plasmas seem a bit an artificial consideration. However, it was shown [93] that these plasmas can be produced in the lab via a laser drive with relatively high density and existence duration.

We proof that for the heavier ion case $m_i/m_e \gtrsim 1836$, where equality is reached in case of electron-proton plasma, the fluid description is valid in the linear regime. It allows us to stick to the easier description throughout this thesis.

Furthermore, we show that in the electron-positron case $m_i/m_e = 1$ the fluid and kinetic descriptions agree again, but only in the strong coupling regime. This renders the investigations made in Ch. 6 about chirping the pump pulse in the strong coupling regime valid for any ion species. In weak coupling the plasma

mode is damped.

However, the dispersion relation derived here is even more powerful, as it covers the case of weakly relativistic laser amplitudes. This implies that it can be analyzed and investigated in regimes exceeding the investigations made throughout this work.

This chapter is organized as follows. We give a brief description of the derivation of the kinetic dispersion relation. A detailed version is given in appendix A.1 in Sec. 4.1, basically following [71] for the more general case of arbitrary ion species with arbitrary temperature ratio between ions and electrons. Afterwards, we discuss the electron-proton case in Sec. 4.2 and remark the similarity to the fluid description given by Eq. (2.92) in Sec. 2.3.2. Subsequently, we discuss the differences occuring for electron-positron plasmas in Sec. 4.3. We find the laser strength dependence of the growth rate $\Gamma \propto a_0^2$ stated in [70]. Lastly, we sum up the results in Sec. 4.4. The content of this chapter is part of the manuscript [73].

4.1 Weakly relativistic kinetic dispersion relation for an arbitrary homogeneous plasma

Similar to [71] we start with Maxwell's equations in potential form Eqs. (2.5) and (2.6) and the Vlasov equation (2.7)

$$\left(\nabla^2 - \frac{1}{c^2}\frac{\partial^2}{\partial t^2}\right)\mathbf{A} = -\frac{4\pi}{c}\mathbf{j}_\perp, \tag{4.1}$$

$$\nabla^2\phi = -4\pi e\left(n_i - n_e\right), \tag{4.2}$$

$$0 = \frac{\partial}{\partial t}f_k + \mathbf{v}\cdot\nabla_{\mathbf{r}}f_k + q_k\left(\mathbf{E} + \frac{1}{c}\mathbf{v}\times\mathbf{B}\right)\cdot\nabla_{\mathbf{p}}f_k, \tag{4.3}$$

with the vector potential $\mathbf{A}$, the electrostatic potential ϕ, the distribution function f_k, speed of light c, perpendicular current $\mathbf{j}_\perp$, elementary charge e and particle charge q_k, density n_k, velocity $\mathbf{v}$, electric field $\mathbf{E}$ and magnetic field $\mathbf{B}$. The index k denotes the species $k = e, i$, hence electron or ion, and $\mathbf{B} = \nabla\times\mathbf{A}$.

We assume the distribution function f_k only depending on the laser propagation direction z and find

$$f_k\left(z, \mathbf{p}, t\right) = n_{k0}g_k\left(z, p_z, t\right)\delta\left(p_x + \frac{q_k A_x}{c}\right)\delta\left(p_y + \frac{q_k A_y}{c}\right), \tag{4.4}$$

where δ denotes the δ distribution. We assume $n_{i0} = n_{e0} \equiv n_0$ and write

$$n_k\left(z, t\right) = n_0\int_{-\infty}^{+\infty}dp_z\left[g_k\left(z, p_z, t\right)\right], \tag{4.5}$$

$$\mathbf{j}_\perp\left(z, t\right) = -\frac{e^2 n_0}{c}\mathbf{A}\left(z, t\right)\int_{-\infty}^{+\infty}dp_z\left[\frac{g_i}{m_i\gamma_i} + \frac{g_e}{m_e\gamma_e}\right],$$

$$= -\frac{e^2 n_0}{m_e c}\mathbf{A}\left(z, t\right)\int_{-\infty}^{+\infty}dp_z\left[\beta\frac{g_i}{\gamma_i} + \frac{g_e}{\gamma_e}\right], \tag{4.6}$$

where $\beta = m_e/m_i$ denotes the mass ratio. The Lorentz factor γ_k is given as

$$\gamma_e = \sqrt{1 + \left(\frac{p_z}{m_e c}\right)^2 + \left(\frac{e\mathbf{A}\left(z, t\right)}{m_e c^2}\right)^2}, \tag{4.7}$$

$$\gamma_i = \sqrt{1 + \beta^2\left(\frac{p_z}{m_e c}\right)^2 + \beta^2\left(\frac{e\mathbf{A}\left(z, t\right)}{m_e c^2}\right)^2}, \tag{4.8}$$

Inserting Eqs. (4.4)-(4.8) into the initial system (4.1)-(4.3) we find

$$\left(\frac{\partial^2}{\partial z^2} - \frac{1}{c^2}\frac{\partial^2}{\partial t^2}\right)\mathbf{A} = \frac{\omega_{pe}^2}{c^2}\mathbf{A}\int_{-\infty}^{+\infty}dp_z\left[\beta\frac{g_i}{\gamma_i} + \frac{g_e}{\gamma_e}\right], \tag{4.9}$$

$$\frac{\partial^2}{\partial z^2}\phi = -4\pi e n_0 \int_{-\infty}^{+\infty}dp_z\left[g_i - g_e\right], \tag{4.10}$$

$$0 = \frac{\partial}{\partial t}g_k + v_z\frac{\partial}{\partial z}g_k + \left[-q_k\frac{\partial}{\partial z}\phi - \frac{m_k}{2}\left(\frac{e}{m_k c}\right)^2\frac{1}{\gamma_k}\frac{\partial}{\partial z}\mathbf{A}^2\right]\frac{\partial}{\partial p_z}g_k. \tag{4.11}$$

Perturbing the system (4.9)-(4.11) via

$$\phi = \phi_0 + \epsilon\phi_1, \quad \mathbf{A} = \mathbf{A}_0 + \epsilon\mathbf{A}_1, \quad g_k = g_{k0} + \epsilon g_{k1},$$

$$\phi_0 = 0, \quad \mathbf{A}_0 = A_{0\perp} = A_{0x} + iA_{0y} = A\exp\left(i(k_0 z - \omega_0 t)\right), A \in \mathfrak{R},$$

$$\phi_1 = \tilde{\phi}\exp\left(i(kz - \omega t)\right) + \tilde{\phi}^*\exp\left(-i(k^* z - \omega^* t)\right),$$

$$g_{k1} = \tilde{g}_k\exp\left(i(kz - \omega t)\right) + \tilde{g}_k^*\exp\left(i(k^* z - \omega^* t)\right),$$

$$A_{1\perp} = A_+\exp\left(i(k_+ z - \omega_+ t)\right) + A_-\exp\left(i(k_- z - \omega_- t)\right),$$

with $k_+ = k_0 + k$, $k_- = k_0 - k^*$, introducing $a_0 = eA_\perp/mc^2$, selecting first-order and only resonant terms yields the weakly relativistic kinetic dispersion relation for arbitrary ion species

$$D_+ D_- = \frac{\omega_{pe}^2 a_0^2}{4}(D_+ + D_-)\left[I_4 - m_e c^2 k\left(F + I_3\right)\right], \tag{4.12}$$

with

$$I_n = \beta^{n-1}I_{in} + I_{en},$$

$$I_{kn} = \int_{-\infty}^{+\infty}dp_z\left[\frac{1}{\gamma_{k0}^{n-1}}\frac{\partial g_{k0}/\partial p_z}{v_z k - \omega}\right], \quad n = 1, 2, 3,$$

$$I_{k4} = \int_{-\infty}^{+\infty}dp_z\left[\frac{g_{k0}}{\gamma_{k0}^3}\right],$$

$$D_+ = -\omega_+^2 + c^2 k_+^2 + \omega_{pe}^2\int_{-\infty}^{+\infty}dp_z\left[\frac{\beta}{\gamma_{i0}}g_{i0} + \frac{1}{\gamma_{e0}}g_{e0}\right],$$

$$D_- = -\omega_-^{*\,2} + c^2 k_-^{*\,2} + \omega_{pe}^2\int_{-\infty}^{+\infty}dp_z\left[\frac{\beta}{\gamma_{i0}}g_{i0} + \frac{1}{\gamma_{e0}}g_{e0}\right],$$

$$F = \frac{4\pi e^2 n_0 I_2^2}{k - 4\pi e^2 n_0 I_1}.$$

Non-relativistic limit

In the non-relativistic limit we have $\gamma_{k0} \approx 1$, $I_{k4} \approx 0$ and we take the 1D-distribution function to be Maxwellian

$$g_{k0} = \frac{1}{m_k v_{thk} \sqrt{\pi}} \exp\left(-v_z^2/v_{thk}^2\right), \quad v_{thk} = \sqrt{\frac{k_B T_k}{m_k}}. \tag{4.13}$$

We notice that we can identify the Integrals I_{kn} with the electric susceptibilities (see e.g. [81]) via

$$I_{kn} = -\frac{1}{k m_k v_{thk}^2}\left[1 + \frac{\omega}{\sqrt{2} m_k v_{thk}} Z\left(\frac{\omega}{\sqrt{2} m_k v_{thk}}\right)\right] = -\frac{k}{m_e \omega_{pe}^2} \chi_k, \tag{4.14}$$

where Z denotes the complex plasma Z-function, discussed in various literature, e.g. [41]. It is given by

$$Z(\zeta) = \frac{1}{\sqrt{2}} \int_{-\infty}^{\infty} \frac{e^{-t^2}}{t - \zeta} dt. \tag{4.15}$$

We expect larger growth for the downshifted light wave, thus $D_- \approx 0$. Inserting into Eq. (4.12) delivers

$$\frac{a_0^2 c^2 k^2}{4 D_-} = \frac{1 + \chi_i + \chi_e}{\chi_e \left[1 + (1 + \beta^2) \chi_i\right] + \beta^2 \chi_i}, \tag{4.16}$$

with $D_- = -\omega^2 + c^2 k^2 + (1 + \beta) \omega_{pe}^2$. We note $\chi_k \gg 1$ and can therefore approximate

$$(1 + \beta)^2 \frac{a_0^2 c^2 k^2}{4 D_-} \approx \frac{1}{\chi_e} + \frac{1}{\chi_i}. \tag{4.17}$$

We write

$$\chi_e^{\text{kin}} = \frac{1 + \zeta_e Z(\zeta_e)}{k^2 \lambda_{De}^2}, \qquad \chi_i^{\text{kin}} = \alpha \frac{1 + \sqrt{\alpha/\beta} \zeta_e Z(\sqrt{\alpha/\beta} \zeta_e)}{k^2 \lambda_{De}^2}, \tag{4.18}$$

$$\chi_e^{\text{flu}} = \frac{1}{k^2 \lambda_{De}^2}, \qquad \chi_i^{\text{flu}} = -\frac{\omega_{pi}^2}{\omega^2}, \tag{4.19}$$

where χ_j^{kin} denotes the kinetic and χ_j^{flu} the fluid susceptibilities, where $\alpha = T_e/T_i$ is the temperature ratio and $\zeta_e = \omega/\sqrt{2} m_e k v_{the}$. Eq. (4.17) is the non-relativistic kinetic dispersion relation for arbitrary ion species. Note that in the limit $\beta \to 1$, thus in the electron-positron case, we arrive at the dispersion relation given by Shukla *et al.* [70], while $a_{\text{Shukla}} = a/2$.

Fig. 4.1 describes how Eq. (4.17) is solved. For a fixed wavenumber k we evaluate the dispersion relation in real part $\Re(\omega)$ and imaginary part $\Im(\omega)$. In Fig. 4.1, we measure ω in units of $\omega_{pe}/\sqrt{2} k \lambda_{De}$, where λ_{De} is the Debye-length

of electrons. We draw the lines where Eq. (4.17) is fulfilled. In more detail, this means that in Fig. 4.1 the blue surface marks the area where $\Re(\text{RHS}) > \Re(\text{LHS})$. The red area is assigned to $\Im(\text{RHS}) > \Im(\text{LHS})$, where RHS and LHS denote the right- or left-hand-side, respectively, of Eq. (4.17). This is necessary because evaluation of the Z-function is very complicated. If the two borders of the surfaces cross, Eq. (4.17) is fulfilled.

Fig. 4.1 consists of three different cases, differing in pump strength a_0. For the first case $a_0 = 0.005$ we find the cut at $\Re(\omega) \approx 0.02$ and $\Im(\omega) \approx 0.005$. For $a_0 = 0.01$ we have $\Re(\omega) \approx 0.03$ and $\Im(\omega) \approx 0.02$ as a solution of Eq. (4.17). In case of $a_0 = 0.05$ the search of the crossing point complicates even further. Here, instead of one distinct point we find a full crossing line. The point chosen for evaluating the growth rate Γ is assumed to be the crossing point closest to origin, i.e. roughly at $\Re(\omega) \approx 0.06$ and $\Im(\omega) \approx 0.06$.

We always have these hard-to-find growth rates Γ if the pump strength a_0 is strong enough such that the interaction is strongly coupled.

The evaluation is done automatically using a scripted language, e.g. Mathematica.
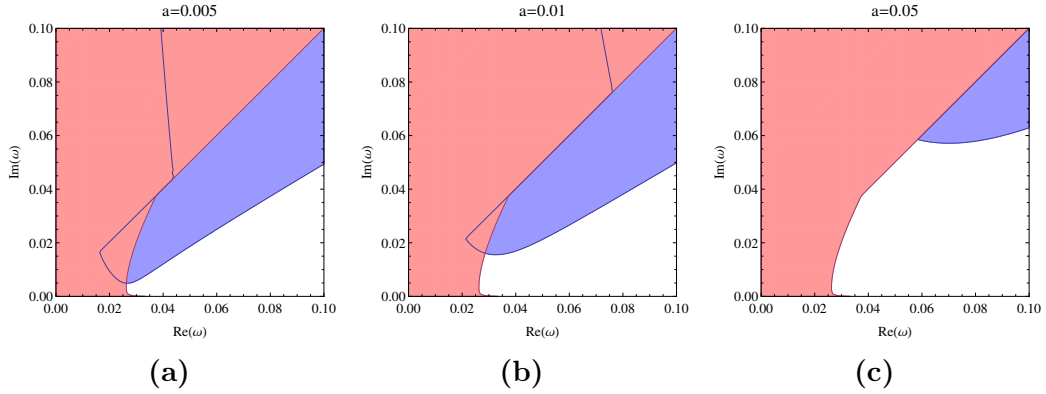
Figure 4.1: Solving the kinetic dispersion relation Eq. (4.17) via the method explained in text. Evaluation of the complex Z-function requires the comparison of real and imaginary part of right-hand-side with left-hand-side, Eq. (4.17) is fulfilled where both surface borders cross.

4.2 Dispersion in Hydrogen plasmas

We first consider the dispersion relation Eq. (4.17) in the electron-proton limit $\beta = 1/1836$, $\alpha \gg 1$ with kinetic (4.18) and fluid (4.19) description and compare it to the solution of Eq. (2.92).

In Fig. 4.2 we solved the three equations mentioned above for $a_0 = 0.005$. On the x-axis one finds the wavenumber of the plasma oscillation k in units of the laser wavenumber k_0, and on the y-axis the growth rate Γ or the frequency ω in Fig. 4.2a or 4.2b, respectively. In solid black is the solution obtained by solving Eq. (4.17) with kinetic susceptibilities, in dashed blue the solution with fluid description of the susceptibilities and in dotted red the solution of Eq. (2.92), i.e. the dispersion relation derived in Sec. 2.3.2.
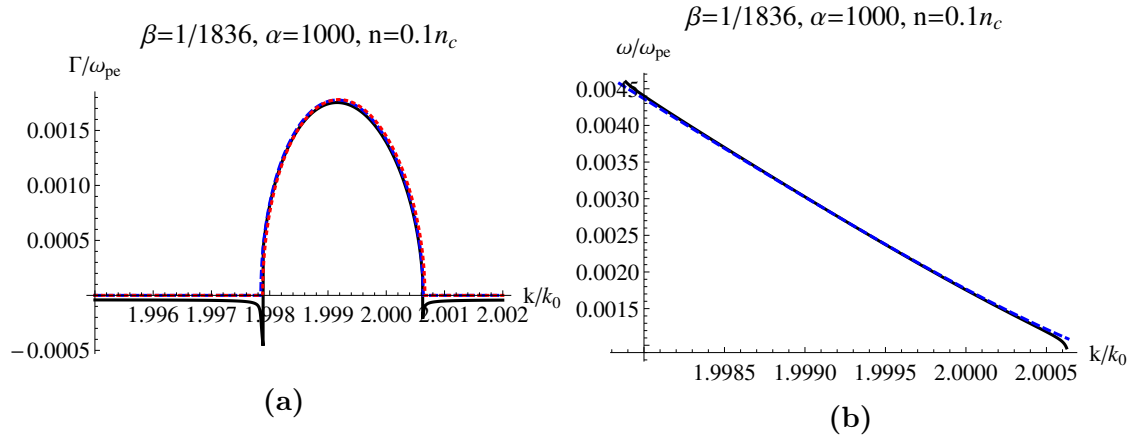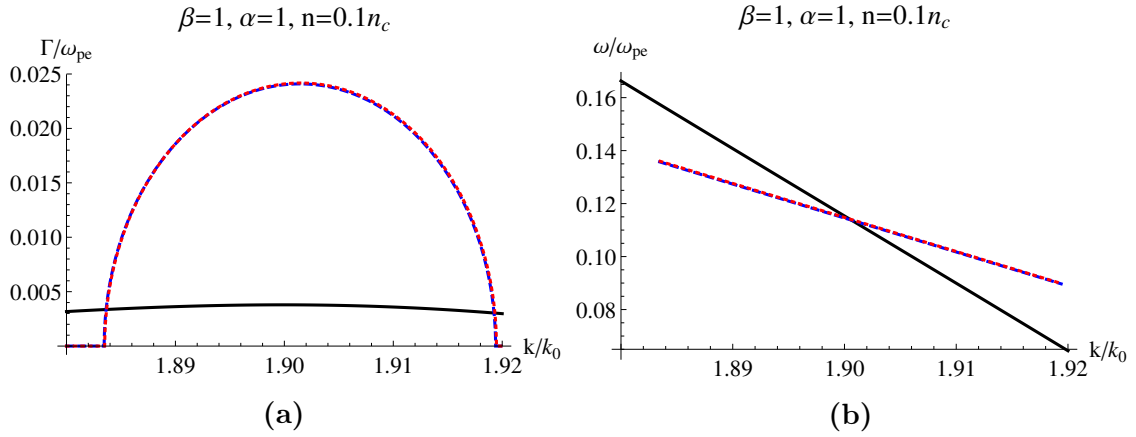

Figure 4.2: Growth rate Γ and real frequency ω over k for $a_0 = 0.005$ obtained from solving Eq. (4.17) with kinetic susceptibilities Eq. (4.18) (solid black), fluid susceptibilities Eq. (4.19) (dashed blue) and from solving Eq. (2.92) (dotted red).

As can be seen, the three different results agree perfectly. The only difference is that the kinetic dispersion relation exhibits areas where $\Gamma < 0$, i.e. where damping of the wave occurs. However, maximum growth rate and its distribution over k as well as the frequency agree.

In Fig. 4.3 we present the results by solving the same equations in the same color format but now pump strength resolved, i.e. on the x-axis is a_0 and on the y-axis one finds the maximum growth rate Γ and frequency ω, respectively.

Again, we find perfect agreement for all pump amplitudes a_0. In both, Subfigs. 4.3a and 4.3b we find two different regions of dependence of a_0. At $a_0 \gtrsim 0.1$ growth changes, as does the frequency. Closer evaluation gives that for $a_0 < 0.1$ we find $\Gamma \propto a_0$ and for $a_0 \gtrsim 0.1$ we have $\Gamma \propto a_0^{2/3}$ and $\Gamma \approx \omega$, as was already discussed in Sec.2.3.2 in Eqs. (2.94) and (2.98).
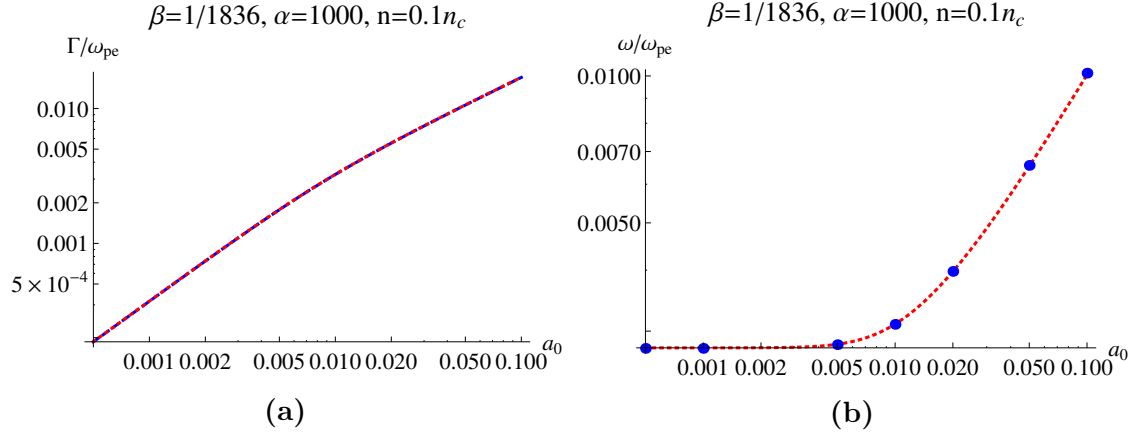
Figure 4.3: Maximum growth rate Γ and its associated real frequency ω vs. pump amplitude a_0 obtained from solving Eq. (4.17) with kinetic susceptibilities Eq. (4.18) (solid black), fluid susceptibilities Eq. (4.19) (dashed blue) and from solving Eq. (2.92) (dotted red).

In summary, all three different evaluations deliver the same results,. This means that for electron-ion plasmas, kinetic treatment is not necessary, neither in the weak, nor in the strong coupling regime. We appreciate this result as the evaluation of Eq. (2.92) is much easier than of Eq. (4.17), as was explained with Fig. 4.1.

4.3 Dispersion in Electron-Positron plasmas

In the electron-positron limit $\beta = 1$, $\alpha = 1$ we get the same results for Eq. (4.17) in fluid description (4.19) as Edwards *et al.* [72], with $a_{\text{Edwards}} = \sqrt{2}a_0$, but not if we consider full kinetic treatment.

We consider an electron-positron plasma with $\beta = 1$, $\alpha = 1$, $n = 0.1n_c$ and $T = 200$ eV. We compare the full kinetic treatment via Eq. (4.17) with (4.18) and (4.19) to the dispersion relation given by Edwards *et al.*, i.e. Eq. (42) of the supplemental material of [72].

Fig. 4.4 shows the evaluation of the three different equations mentioned above for fixed $a_0 = 0.005$. The solution of Eq. (4.17) is shown in solid black (with Eq. (4.18)) and dashed blue for fluid treatment of the susceptibilities following Eq. (4.19). The solution of Eq. (42) of [72] is shown in red dotted lines.

In Subfig. 4.4a we directly find that the fluid treatment highly overestimates the growth rate for this given pump strength. Not only this, but also the range of the instability in k is highly underestimated. For the real frequency ω we also see strong disagreement.

Figure 4.4: Growth rate Γ and real frequency ω over k for $a_0 = 0.005$ obtained from solving Eq. (4.17) with kinetic susceptibilities Eq. (4.18) (solid black), fluid susceptibilities Eq. (4.19) (dashed blue) and from solving Eq. (42) in [72] (dotted red). The left side of the black curve follows $\Gamma \propto a_0^2$ behavior.

Fig. 4.5 shows the growth rate Γ for different pump strengths a_0 taken from fluid description [72] (dotted red) and kinetic description (4.17) (solid black). In solid red we show

$$\Gamma = \frac{cka_0}{\sqrt{2}2} \sqrt{\frac{2\omega_{pe}^2}{kC_e\left(\omega_0 - kC_e\right)}}, \tag{4.20}$$

the growth rate given by [72]. We note that the growth rate calculated from the fluid dispersion deviates from the analytic prediction Eq. (4.20). We also note that the a_0 above which the deviation occurs is the same the frequency ω becomes larger than kv_{th}, as Fig. 4.6 shows. This hints that also here strong coupling sets in, where growth occurs with the usual $\propto a_0^{2/3}$ behavior.

Fig. 4.7a shows the ratio of growth rates obtained from full kinetic and fluid description. One observes for low a_0 that there is a large factor between these two. As one approaches the strong coupling regime, the two results converge towards each other. This means for strong coupling Brillouin amplification in electron positron plasmas the fluid description is valid and applicable.

Fig. 4.7b shows the ratio of frequency obtained from full kinetic and fluid description. For each pump strength a_0 we observe a significant blueshift in frequency of roughly 10%, once the dispersion is treated kinetically.
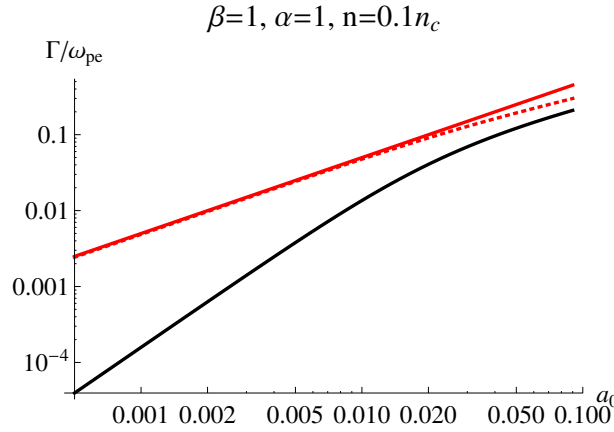
Figure 4.5: Growth rate Γ for different pump strengths a_0 from fluid description (dotted red) and kinetic dispersion (solid black). The solid red line is calculated from (4.20). The position $a_0 \approx 0.02$ seperates weak and strong coupling. In the latter regime, the two results are much closer to each other than in the former regime.
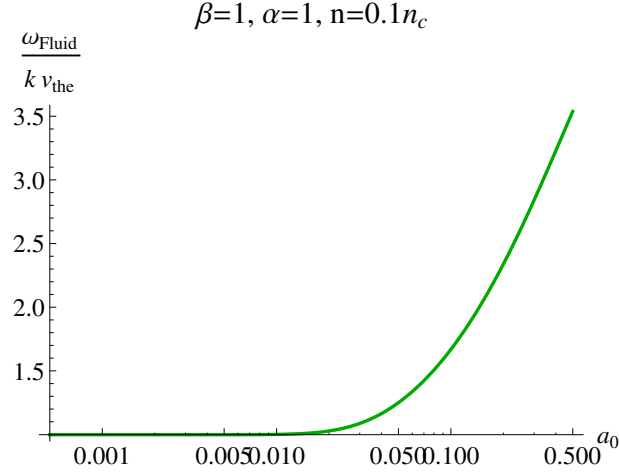
Figure 4.6: Ratio of ω_{Fluid} and kv_{th}. For low values of a_0 it is unity, for larger values it gets much larger, hence a quasi-mode is amplified.
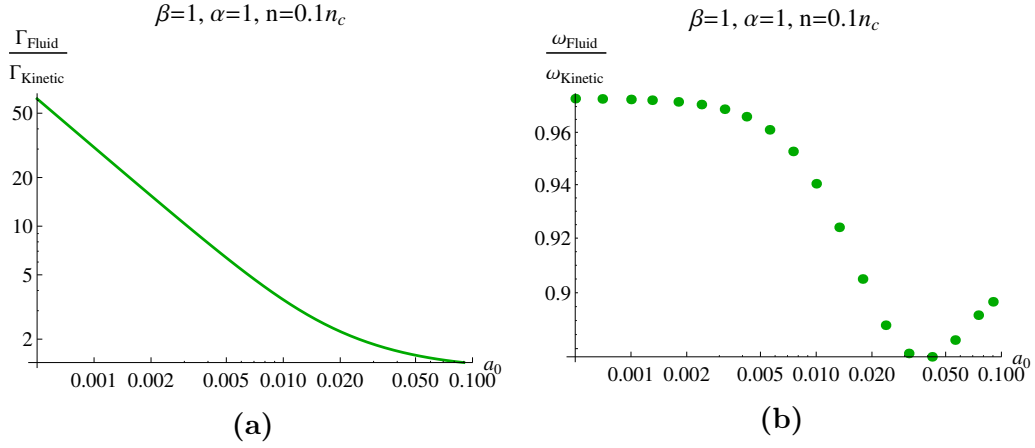
Figure 4.7: Ratio of growth rate Γ (a) and ω (b) between fluid and kinetic treatment. For low amplitudes a_0, there is a grave difference, for larger a_0, i.e. strong coupling, $\Gamma_{\text{Fluid}}/\Gamma_{\text{Kinetic}}$ approaches 1. For ω, kinetic treatment gives a significant blueshift compared to what is obtained by fluid description.

4.4 Conclusion

We have derived a weakly relativistic kinetic dispersion relation for Brillouin amplification in homogeneous plasmas in a single charge state for an arbitrary ion mass m_i and arbitrary temperature ratio T_e/T_i in Eq. (4.12). We remark that this is a powerful equation with its range of application exceeding the needs of the work at hand. Therefore, subsequently, we assumed non-relativistic pump amplitudes and derived the dispersion relation (4.17), with which we investigated the cases of Hydrogen plasma, as well as electron-positron plasma, and discussed the weak and strong coupling regimes.

Although similar to former equations, for the first time such a dispersion relation was derived, filling the picture of understanding.

With the dispersion relation (4.17) we have shown that we can replace the susceptibilities χ either in kinetic description Eq. (4.18), where we need to solve the complex Z- or plasma dispersion function. Or we insert fluid susceptibilities Eq. (4.19) to find a dispersion relation delivering the same results as Eq. (2.92), directly derived from fluid equations.

For an electron-proton plasma, i.e. ionized Hydrogen, we have shown that we obtain the same growth rates and frequencies from kinetic and fluid description, respectively, rendering the former as not necessary for these plasmas. Apparently, the latter is sufficient in describing Brillouin amplification.

In case of electron-positron plasmas, we tackled the message of [72] that here, Brillouin amplification is strongly enhanced, and showed that when treating the interaction more generally, i.e. kinetically, the growth rates actually decrease dramatically. Although Raman growth rates might be reduced even more, to speak of strong enhancement is quite deluding. Additionally, we have shown a significant blueshift in frequency of approximately 10% when treated kinetically in comparison to fluid results.

Furthermore, we have shown that also the fluid description in [72] is not complete as it ignores the differences occurring when entering strong coupling.

5 Transition from weakly to strongly coupled Brillouin amplification

In the following chapter we investigate the transition regime between weakly and strongly coupled Brillouin amplification. Both scattering mechanisms exhibit different characteristics in peak amplitude growth, time- and length-scales as well as duration and self-similarity of the seed pulse. In weak coupling the beat of pump and seed pulse drives an ion acoustic wave with frequency $\omega = kc_s$ and a growth rate $\gamma \ll \omega$. For sufficiently strong pump waves the interaction becomes a quasi-mode of the plasma with $\omega \gg kc_s$ and $\gamma \approx \omega$. Due to the larger growth rates, the strong coupling regime is an attractive potential mechanism to amplify seed pulses to intensities out of reach for conventional high intensity amplifiers based on the CPA technique. The distinction between these two regimes is possible by the parameters of the laser-plasma setup. It is found that today's experiments take place with parameters in the transition regime.

Furthermore, setups initially triggering weak coupling Brillouin scattering will enter strong coupling as soon as the seed pulse exceeds the critical amplitude. On the other hand, starting in strong coupling and entering the nonlinear pump depletion regime will decrease the pump amplitude trailing the leading intensity spike. Thus, it will drop below the critical amplitude which leads to a significant decrease in the overall energy transmission efficiency.

We present a unified treatment for all scenarios, hence covering weak, strong coupling and their transition in a reduced envelope model and see differences to previously used models which were derived for only one asymptotic regime. Furthermore, we give an analytic expression for the time it takes for an arbitrary interaction setup to enter the strong coupling regime and confirm it by simulations.

5.1 Simulations of $\delta N\mathbf{A}$- and envelope models

In this section we investigate the two different models derived in Ch. 3, namely the $\delta N\mathbf{A}$- and ϵ-model Eqs. (3.4)-(3.5) and (3.15)-(3.17), respectively. Once again we clarify characteristics of weakly and strongly coupled Brillouin amplification, as schematically already introduced in Sec. 3.2. Here, we expand the picture of understanding with the transitional case.

We choose typical parameters in experiments with a Hydrogen plasma with an electron temperature $T_e = 200$ eV, background density $n_0 = 0.05 n_c \approx 9 \cdot 10^{19}$ cm^{-3}, where $n_c = \omega_0^2 m_e / (4\pi e^2)$ is the critical density. The central laser wavelength of both pump and seed is $\lambda_0 = 800$ nm and the initial seed amplitude is small at $E_s^0 = a_s = 10^{-3}$ with a duration of 100 fs. The threshold value for a_0 which determines the regime is calculated via $a_{\text{threshold}} = \sqrt{16\omega_0^2 c_s^3 / (\omega_{pi}^2 c^3)}$ (see Eq. (2.99)) and for parameters specified as above we find $a_{\text{threshold}} \approx 0.0075$.

The simulation results of the $\delta N\mathbf{A}$- and ϵ-model, (3.4)-(3.5) and (3.15)-(3.17), respectively, are presented in Fig. 5.1. Parameters are chosen as described above. Results obtained by simulating the $\delta N\mathbf{A}$ model are presented in solid magenta. ϵ-model results are represented with dashed-crossed black lines. For the strong coupling limit we find self-similar behavior [50] in the pulse envelope shape 5.1a as we observe characteristic oscillations behind the leading maximum. The oscillations behind the leading maximum drop down to zero. Functions following this trait are named π-pulse solutions. For the weak coupling limit 5.1c we also find self-similar behavior [92, 62] (described for Raman amplification, which is analog).

For $a_0 = 0.1$ ($\to I_0 \approx 10^{16}$ W/cm^2, Subfig. 5.1a) we have $\epsilon \approx 4.9$ and simulated for 1.1 ps. For $a_0 = 0.01$ ($\to I_0 \approx 10^{14}$ W/cm^2, Subfig. 5.1b) $\epsilon \approx 1$ and an interaction time of 8 ps. For Subfig. 5.1c we observed amplification during 58 ps and $a_0 = 0.001$ ($\to I_0 \approx 10^{12}$ W/cm^2) $\epsilon \approx 0.2$. Thus both limiting regimes and the transition should be covered. The respective interaction time is chosen such that characteristic appearance can be discussed.

For the transition case 5.1b we see the front amplified according to strong coupling theory but the back is in beat with another frequency. From the very complicated seed envelope, which changes substantially in time and space, one can deduce that formulating a self-similar solution which covers the whole interaction spectrum might be difficult. However, we give it a try in Apx. A.2 and came to results at least qualitatively agreeing. We were able to reproduce the shown envelopes. Still, self-similar solutions usually predict growth of the leading maximum, which we failed to achieve with our solution.

The lower row of Fig. 5.1 shows the respective density profiles. In 5.1d we find

the characteristic density slab for strong coupling with a quadratic slope. In Subfig. 5.1e we see many of these slabs. Subfig. 5.1f shows the characteristic density plateau for weak coupling. Remarkably, we notice very good agreement between the two models. Apparently an initially fixed ϵ (see Eq. (3.18)), which determines whether strong or weak coupling is the dominant process still gives access to the transition regime (see Subfig 5.1b). This is an interesting feature from a physical point of view but also in practical terms since simulating the envelope model is computationally much less demanding.

(a) $a_0 = 0.1$ **(b)** $a_0 = 0.01$ **(c)** $a_0 = 0.001$

(d) **(e)** **(f)**
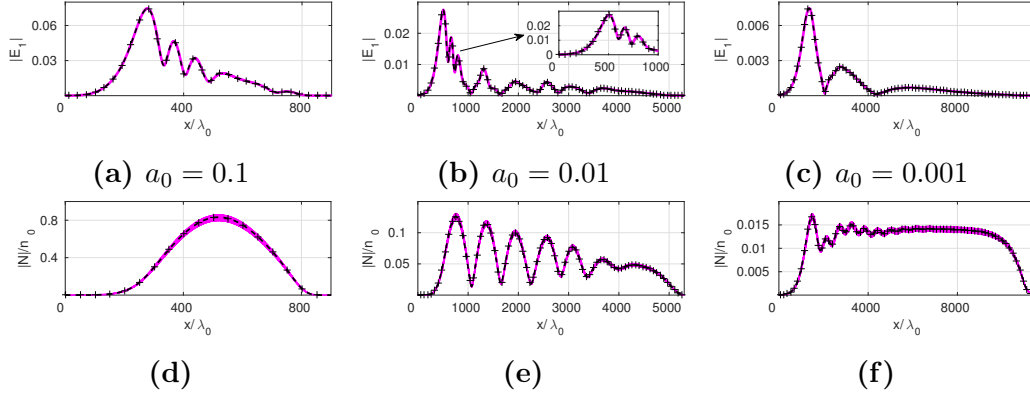
Figure 5.1: Simulation results for model (3.4)-(3.5) (solid magenta) and (3.15)-(3.17) (dashed-crossed black) for parameters as specified in text. Shown are amplified seed pulse envelopes (upper row) and density waves (lower row). For the limit regimes (a) strong coupling and (c) weak coupling, self-similar behavior is found in the pulse shape. In the transition regime (b) we find the front to follow strongly coupled behavior but the back part is in beat with a second frequency. Also shown in [58].

However, although we start with a pump amplitude around the threshold $a_0 \sim a_{\text{threshold}}$ we end up in the strong coupling regime. This is due to the fact that during amplification the seed eventually surpasses the threshold limit and therefore the interaction in the front part will be strongly coupled. This is a crucial observation as in the front most of the pulse energy is stored. So in principle no matter how small the initial amplitudes are chosen, if the interaction lasts for a sufficiently long time it will end up strongly coupled.

Besides seeing the transition from weak to strong coupling in the envelope shape we also find evidence in the spectra and growth of the seed maximum in time. For the results obtained by simulating either the $\delta N\mathbf{A}$- or ϵ-model are the same, we stick with the latter. Fig. 5.2 shows a simulation for $a_0 = 0.005$ ($\to I_0 = 2.5 \cdot 10^{13}$ W/cm^2), thus well below the threshold, over 20 ps for the same seed and plasma parameters as before. On top we see the normalized seed spectrum in k over time t. Subfig. 5.2a was obtained by simulating $\epsilon = 0$ which gives us the pure weak coupling model. Subfig. 5.2b assumes the actual $\epsilon \approx 2/3$. In Subfig. 5.2c we see

the maximum growth over time as the blue line corresponds to $\epsilon = 0$ with the blue circles representing linear growth, which is expected for weak coupling. The red line corresponds to $\epsilon \approx 2/3$, thus no neglect of the second derivative with respect to t in the density equation. The red circles represent growth proportional to $t^{3/4}$, which is expected for strong coupling.
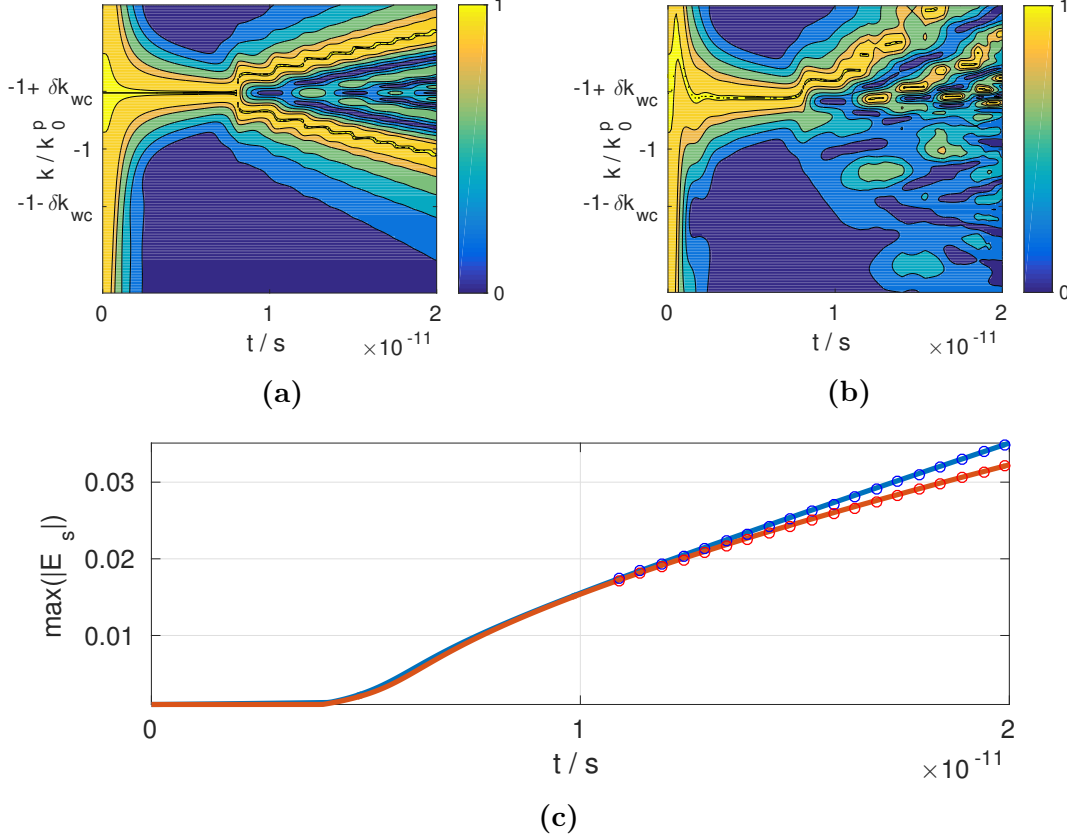

Figure 5.2: Simulation results for model (3.15)-(3.17) for parameters as specified in text. Shown are normalized seed spectra (upper row) and the maximum growth (lower row) for $\epsilon = 0$ ((a), blue line) and $\epsilon \approx 2/3$ ((b), red line). The circles in (c) correspond to growth $\propto t$ (weakly coupled) or $\propto t^{3/4}$ (strongly coupled).

Note that sometimes we use $E_0 \equiv E_p$ and $E_1 \equiv E_s$ equivalently. For pure weakly coupled treatment $\epsilon = 0$ the seed spectrum broadens symmetrically around $-1 + \delta k_{\mathrm{wc}}$ in the nonlinear regime and the maximum grows linearly as the fit shows. $\delta k_{\mathrm{wc}} = 2\omega_0 c_s/c^2$ is the value given by Kruer [41] for the deviation of the plasma wave number from $2k_0^p$ at which the mode with the highest growth rate γ is located in weak coupling, as it was introduced in Eq. (2.95) in Sec. 2.3.2. For the chosen parameters we find $\delta k_{\mathrm{wc}} \approx 0.001 k_0^p$. For that reason δk is also the detuning that applies itself to the two laser pulses, although initially they are not detuned. For the full model $\epsilon \approx 2/3$ we note asymmetric amplification and faster spectral

broadening, as it is typical for strong coupling, as soon as the seed exceeds the threshold after $t \approx 11$ ps.

5.1.1 Linear regime

In the following we investigate the linear regime by analyzing the ϵ model. The linear regime is characterized by a large pump in comparison to seed which does not lose energy and thus stays uniform, hence we can assume E_p as constant. The remaining Eqs. (3.16)-(3.17) can be Fourier transformed in space $x \to k$ and Laplace transformed in time $t \to p$ in order to find

$$E_s(p,k) = \frac{1}{p - \mathrm{i}\alpha k - \frac{\mathrm{i}|E_p|^2}{\epsilon p^2 + 2\mathrm{i}p}} E_s(t=0,k), \tag{5.1}$$

$$\to E_s(t,k) = A(t,k) E_s(t=0,k), \tag{5.2}$$

where A is the Laplace backtransformation of the fraction in Eq. (5.1) which can be calculated numerically and in the following is referred to as the amplification function. Eq. (5.2) describes how an initial signal $E_s(t=0,k)$ evolves in time in the linear regime.

We note that this analysis has been done before (see e.g. [50]) but always with different models, distinctly derived for either weak or strong coupling. Already for weak coupling amplification in the linear regime we noted differences between results obtained by numerical simulation of the ϵ-model versus reduced models and also by analytics.

Fig. 5.3 shows $\log|A|$ in dependence of k_1, i.e. the wavenumber of the seed, evaluated for $a_0 = 10^{-1}$, 10^{-2} and 10^{-3}, in order to keep consistency with Fig. 5.1, at $t = 4$ (corresponding to 0.4 ps, 1.8 ps and 8.4 ps, respectively). We remark that the mode at $k_1 = -(k_0 + \delta k)$ is oscillating in time between 1 and 0 while the mode at $k_1 = -(k_0 - \delta k)$ is growing. This can be seen e.g. for $a_0 = 0.001$, i.e. the solid red line, where the dip marks the lower wavenumber and vice versa. After a large time $t \gg 4$ we would no longer see the beat frequency of $2\delta k$ in density and seed but the solution converges to the one obtained by simulating more reduced models.

When analyzing the amplification function $|A|$, we find the separation of the oscillating part at $k_1 = -(k_0 + \delta k)$ and the growing part at $k_1 = -(k_0 - \delta k)$. This is consistent to what we find in simulations.
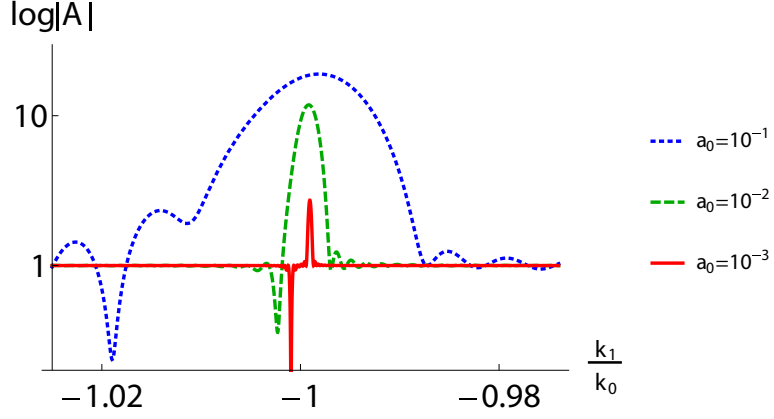
Figure 5.3: Amplification function $|A|$ for $a_0 = 10^{-1}$ (dotted blue), 10^{-2} (dashed green) and 10^{-3} (solid red) after $t = 4$ (for corresponding durations in units see text). On the x-axis we show the wavenumber of the seed.

As mentioned before, δk is the detuning between pump and seed that the system applies on itself during the interaction. The analytic limit $\delta k_{\mathrm{wc}} = 2\omega_0 c_s / c^2$ only holds for low pump strength $a_0 \ll 1$ as is suggested by Fig. 6.10. Here, we obtain δk by solving the full dispersion relation (see eg. [41]) and finding the wavenumber with the highest growth rate. For large $a_0 \rightarrow 1$ the ratio converges to zero, $\delta k / \delta k_{\mathrm{wc}} \rightarrow 0$.
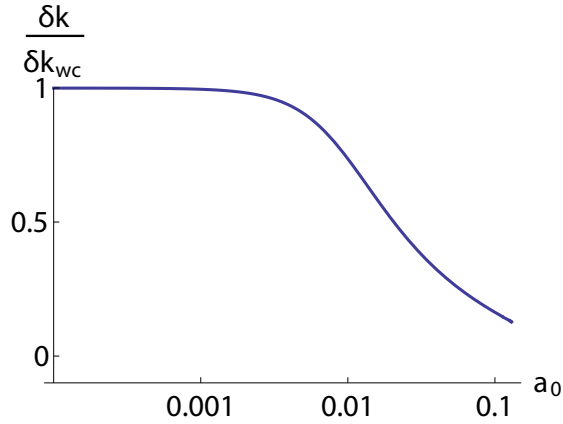
Figure 5.4: Ratio of detuning δk to analytic limit δk_{wc} over pump strength a_0. For large $a_0 \rightarrow 1$ the ratio converges to zero, thus no detuning between pump and seed establishes in the strong coupling regime.

5.1.2 Nonlinear regime

We first analyze whether the detuning derived from linear theory remains true in the nonlinear phase. We simulate the same parameters and setups as in Sec. 5.1, thus $a_0 = 0.1, 0.01, 0.001$ but now for a much longer interaction time. The resulting detuning ratio is $\delta k/\delta k_{\mathrm{wc}} \approx 0, 0.75, 1$.

Fig. 5.5 shows the final seed envelopes and the normalized density spectra over time. The upper row (Subfigs. 5.5a-5.5c) shows the final seeds for $a_0 = 0.1$ after 5 ps, $a_0 = 0.01$ after 25 ps and $a_0 = 0.001$ after 230 ps. We note that all three cases are structurally similar: there is an "envelope of the envelope" which shows weak coupling characteristics, while in between and especially in the leading front we find oscillations not going down to zero. The latter is an indication for strong coupling behavior. Only the final seed amplitudes and both time and space scales change with pump strength.

(a) (b) (c)

(d) (e) (f)
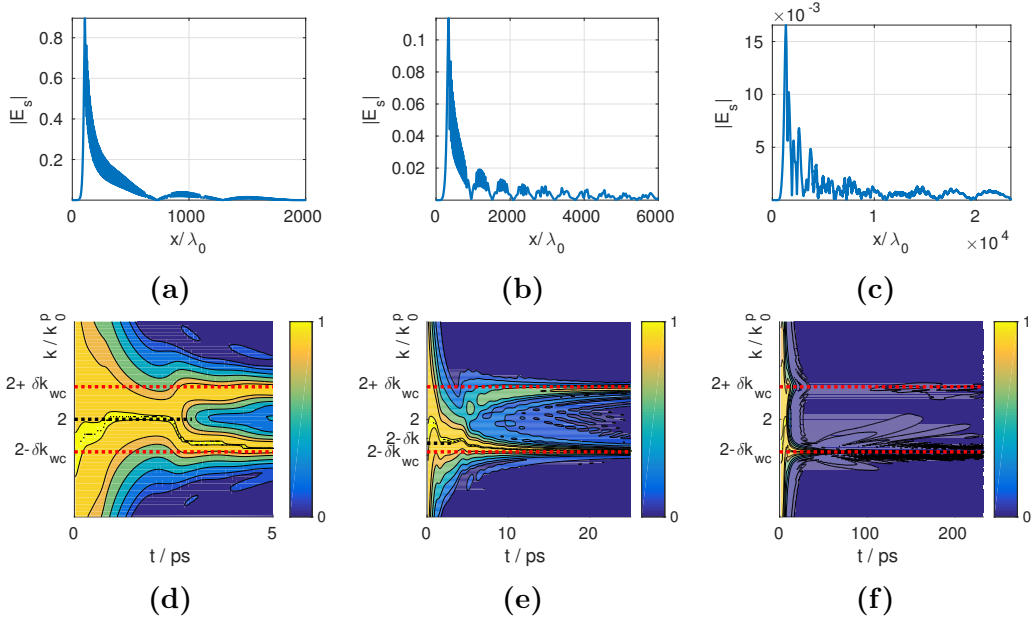
Figure 5.5: Seed envelopes for $a_0 = 0.1$ at 5 ps (a), $a_0 = 0.01$, 25 ps (b), $a_0 = 0.001$, 230 ps (c) and the corresponding density spectra over time (d)-(f).

In the density spectra we note that the maximum growth occurs for the respective $k = 2k_0^p - \delta k$ as expected from linear theory. It is highlighted by the black dashed line. For $a_0 = 0.1$ (Subfig. 5.5d) we see that up to $t \approx 3$ ps the maximum of the spectrum is at $k \approx 2k_0^p$. Consecutively, there are two maximum branches eventually converging to $2k_0^p \pm \delta k_{\mathrm{wc}}$. Consequently, this is visible in the density envelope, as it develops oscillations precisely as shown in Fig. 5.1e. These oscillations are then imprinted on the seed envelope, resulting in that "envelope of the envelope". We estimate the time it takes for the system to develop such oscillations by noting

that, as soon as two wavelengths of the beat fit inside the driven density, these two branches will develop,

$$t_{\text{split}} v_g = 2\frac{2\pi}{2\delta k_{\text{wc}}}, \qquad \Rightarrow \qquad t_{\text{split}} = \frac{\pi}{c_s k_0^p}, \qquad (5.3)$$

where v_g is the group velocity of the seed. For the chosen parameters we calculate $t_{\text{split}} \approx 3$ ps. The length of the black dotted line in Subfigs. 5.5d-5.5f corresponds to the calculated t_{split} and for $a_0 = 0.1$ we find very good agreement between the estimate and the actual time it takes for the density to split into two branches.

For $a_0 = 0.01$ (Subfig. 5.5e) we observe that in the initial stage for roughly 5 ps the maximum of the density spectrum is found at $2k_0^p - \delta k$, where $\delta k \approx 3/4\delta k_{\text{wc}}$, as expected from linear theory. We also note that it takes the system longer (around 5 ps) to develop the splitting at $2k_0^p \pm \delta k_{\text{wc}}$. For $a_0 = 0.001$ (Subfig. 5.5f) it takes even longer (around 150 ps).

For $a_0 = 0.1$ we start the interaction in strong coupling and the instability is broad, i.e. covers a large interval in k. As soon as their beat fits inside the driven density oscillation, both modes at $2k_0^p \pm \delta k_{\text{wc}}$ can and will be amplified. The seed envelope then develops a second envelope looking like originating from weak coupling. For both $a_0 = 0.01$ and 0.001 we do not clearly start in the strong coupling regime. The width of the instability increases with the pump strength. This means that although the beat of $2\delta k_{\text{wc}}$ would fit inside the driven density wave we cannot see amplification at both modes $2k_0^p \pm \delta k_{\text{wc}}$ because it does not amplify this broad spectrum yet. When the seed grows and exceeds the pump, it gradually increases the unstable spectrum until eventually both density modes are covered and consequently amplified.

This gives rise to a second time scale t for which the seed has to be amplified so that afterwards the splitting into the two density modes can happen. From massive simulation data we found that the seed spectral broadening goes with $\tilde{k}_{\text{shift}} \approx \epsilon \tilde{t}$ in dimensionless units, translating into

$$k_{\text{shift}} \approx \frac{3\sqrt{3}}{32}\frac{a_0^2 \omega_{pi}^2}{c_s}t, \qquad (5.4)$$

when reintroducing dimensions. Furthermore, we noticed that the amplification time necessary for the system to develop both density modes coincides with the amplification duration necessary for the seed to surpass the strong coupling threshold. Therefore we call the time duration $t_{\text{wc}\rightarrow\text{sc}}$. When $\delta k \approx \delta k_{\text{wc}}$ a broadening by $k_{\text{shift}} \approx 2\delta k_{\text{wc}}$ is required, so we find

$$t_{\text{wc}\rightarrow\text{sc}} \approx \frac{128}{\sqrt{27}}\frac{c_s^2}{c^2}\frac{\omega_0}{\omega_{pe}^2}\frac{1}{a_0^2}. \qquad (5.5)$$

We note that both durations t_{split} and $t_{\text{wc}\to\text{sc}}$ must be exceeded before we observe growth of both density modes. The former typically limits an interaction starting in strong coupling, as the instability is already broad here. Whereas the latter is the limiting duration when starting in weak coupling, as the instability is not yet broad but the driven density wave is. We note that $t_{\text{wc}\to\text{sc}} \propto T_e n^{-1} a_0^{-2}$ which we investigate further in the following chapter.

5.2 Weak-to-strong coupling transition

In the following chapter, we vary one parameter while holding the other two constant in order to validate the $\propto T_e n^{-1} a_0^{-2}$ dependency in $t_{\text{wc}\to\text{sc}}$ given by Eq. (5.5).

For Fig. 5.6 we hold $n = 0.05n_c$ and $T_e = 200$ eV constant and vary $a_0 = 0.01$, $0.01/\sqrt{2}$ or 0.005. In the upper row one finds the seed spectra over time. The horizontal dotted red lines highlight $k = -1 \pm \delta k_{\text{wc}}$. Since for the chosen pump strengths $\delta k \approx \delta k_{\text{wc}}$ holds, we find the seed maximum in the linear regime at approximately $-1 + \delta k_{\text{wc}}$. After the amplification enters pump depletion, the seed spectrum rapidly broadens. The green dashed lines correspond to the spectral broadening over time k_{shift} introduced in Eq. (5.4). The white line and text correspond to the time $t_{\text{wc}\to\text{sc}}$ given by Eq. (5.5). It marks the point in time where the second density mode grows and the seed front is subject to strongly coupled amplification.
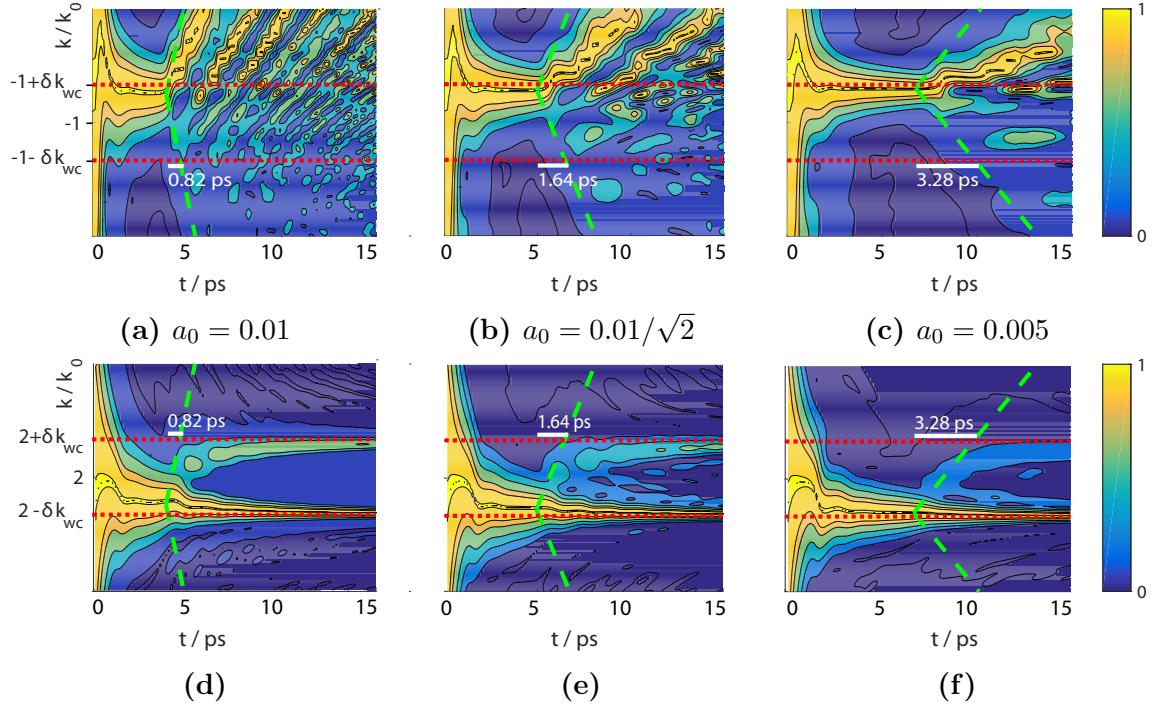
Figure 5.6: Seed (a)-(c) and density spectra (d)-(f) for different pump strengths a_0 at fixed temperature $T_e = 200$ eV and density $n = 0.05n_c$. The horizontal dotted red lines highlight $-1 \pm \delta k_{\text{wc}}$ or $2 \pm \delta k_{\text{wc}}$, respectively. Green dashed is the spectral broadening in the nonlinear regime according to Eq. (5.4). The white line and text gives the duration it takes for the system to transit from weak to strong coupling and develop the two density branches according to Eq. (5.5).

In each case Subfigs. 5.6a-5.6c we find good agreement between the predicted spectral broadening k_{shift} and the actual one. Also the transition duration $t_{\mathrm{wc}\to\mathrm{sc}}$ agrees with the time it takes for the density spectra to develop the second mode in the nonlinear regime Subfigs. 5.6d-5.6f. Furthermore, the three simulations confirm the $\propto a_0^{-2}$ proportionality of the transition time $t_{\mathrm{wc}\to\mathrm{sc}}$.

Figs. 5.7 and 5.8 are constructed in the same way as Fig. 5.6. Fig. 5.7 is to investigate the temperature dependence of Eq. (5.5). It fulfills the prediction $t_{\mathrm{wc}\to\mathrm{sc}} \propto T_e$. In Fig. 5.8 we varied the density and we again find good agreement to analytic expressions. For both, spectral broadening k_{shift} and transition duration, we could confirm the proportionality $t_{\mathrm{wc}\to\mathrm{sc}} \propto T_e n^{-1} a_0^{-2}$.
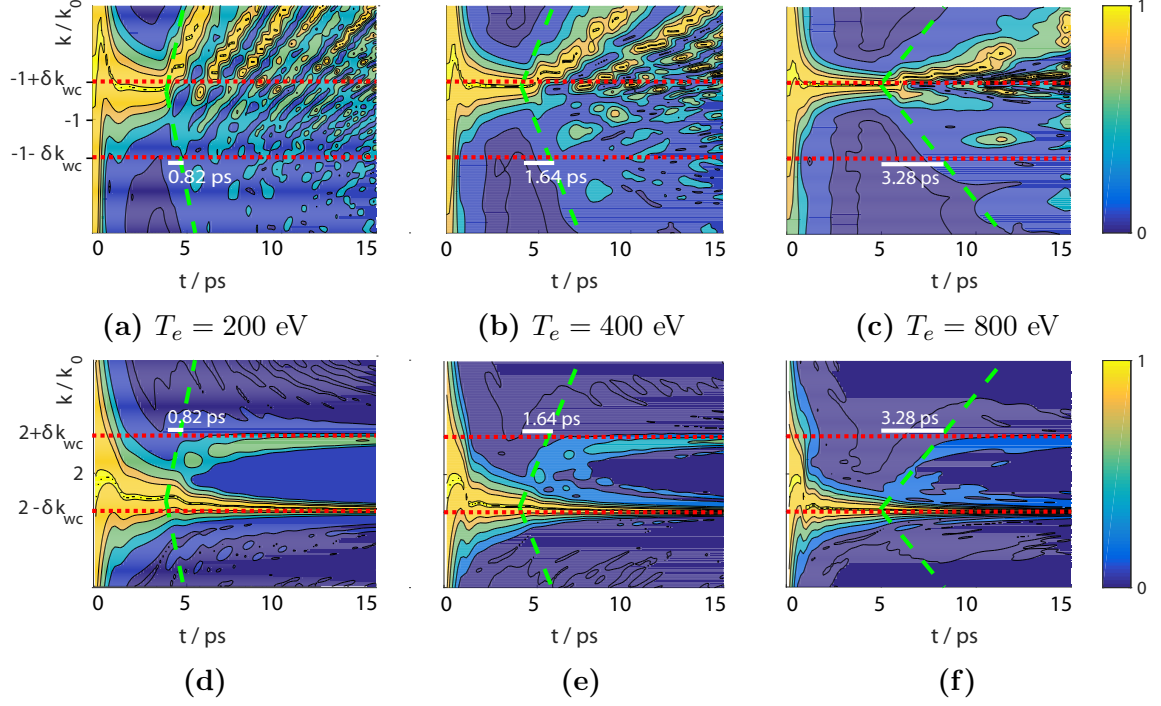
Figure 5.7: Same as Fig. 5.6 but for constant pump strength $a_0 = 0.01$ and density $n = 0.05n_c$ with varying temperature T_e.
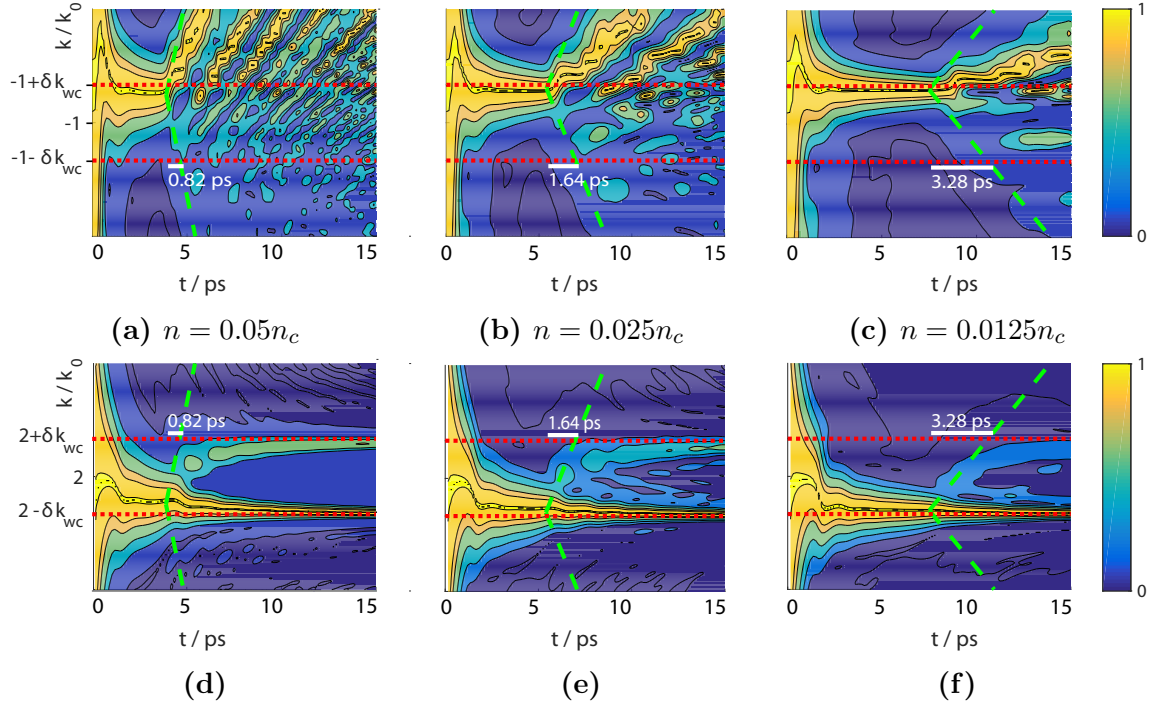
Figure 5.8: Same as Fig. 5.6 but for constant pump strength $a_0 = 0.01$ and temperature $T_e = 200$ eV with varying density n.

5.3 Gaussian shaped pump pulse

We investigated the duration necessary for an arbitrary initially weak coupling setup to enter the strongly coupled regime. Additionally, we have shown that every initially strong coupling setup exhibits weak coupling characteristics in the seed envelope shape. Now we have a look at experimentally relevant Gaussian envelopes for the pump pulse.

We consider the setup described in Fig. 5.9 with the same plasma parameters as in Sec. 5.1.1 with $n = 0.05 n_c$ and $T_e = 200$ eV. In Subfig. 5.9a the pump pulse with peak amplitude $E_0 = 0.03$ and 2.2 ps duration is shown in dashed black. The gray area marks the parts of the pump where it exceeds the strong coupling threshold of $E_{\text{threshold}} = 0.0075$. Apparently, most parts of the pump are above threshold and only in the wings the amplitude is lower. The counterpropagating, lower amplitude seed with $E_1 = 0.001$ and 200 fs duration is shown in magenta.
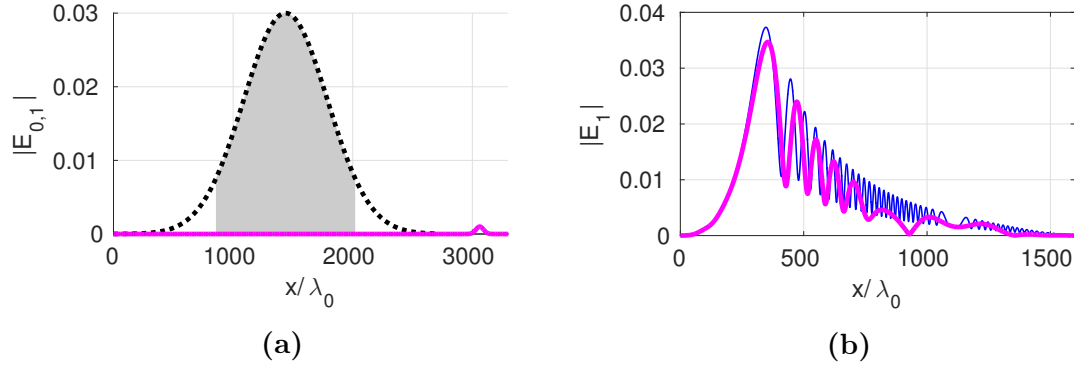
Figure 5.9: Simulation results for model (3.15)-(3.17) for parameters as specified in text. In (a) the initial setup is shown, with the pump in dashed black and the seed in magenta. The gray area marks the parts of the pump exceeding the strong coupling threshold. In (b) the seed is shown after amplification in magenta. For comparison, the blue line is obtained from simulating the same parameters with the same equations, only omitting the first derivative with respect to time in Eq. (3.17). Also published in [58].

Subfig. 5.9b shows the seed after amplification in magenta. For comparison, the simulation result of Eqs. (3.15)-(3.17) under neglect of the first derivative with respect to time in Eq. (3.17), i.e. omitting weakly coupled effects, is plotted in blue.

In a setup described in Fig. 5.9, one would usually assume that weak coupling effects can be neglected as the peak amplitude of the pump exceeds the strong coupling threshold by far. However, this is not quite true. Not considering the full term in Eq. (3.17) overestimates the final peak amplitude of the seed and, in fact, highly overestimates the overall energy transmission efficiency. Evaluation of the

latter has shown that by simulating the full model Eqs. (3.15)-(3.17), the overall energy in the final seed is approx. 25% lower than in case of simulating only the strongly coupled model.

5.4 Conclusion

We studied stimulated Brillouin scattering in weak and strong coupling and during the transition, while focusing on the latter. We used the general $\delta N \mathbf{A}$-model (3.4)-(3.5) and the envelope model (3.15)-(3.17) introduced in Ch. 3. We investigated the two limit regimes weak and strong coupling and especially the transition. Surprisingly, we found remarkable agreement in all simulations performed with both models, although for the simpler model we assumed $\epsilon(a_0)$ to be constant and not changing with varying pump strength a_0.

Simulations of long interaction durations have shown that eventually every initial setup will develop strong as well as weak coupling characteristics. A difference from more reduced models solely treating strong or weak coupling is the growth of two density modes at $2 \pm \delta k_{\mathrm{wc}}$. This will either occur as soon as two wavelengths of the beat $2\delta k_{\mathrm{wc}}$ fit into the driven density slab when the interaction starts strongly coupled. Or when the seed spectrum exceeds a broadness of $2\delta k_{\mathrm{wc}}$ and thus can amplify both density modes when the interaction starts weakly coupled. For both time durations we gave analytic expressions (5.3) and (5.5) and confirmed them by simulations.

This implies that no matter how far away from the strong coupling threshold the initial setup starts, if we hold up the amplification long enough the seed front, while growing in amplitude, will eventually trigger and enter the strong coupling regime. Furthermore, the upcoming density modulation with length scales on the order of hundreds of the laser wavelength should be detectable in experiments.

Lastly, we investigated the amplification with a Gaussian shaped pump pulse. Here, we have shown that even though its peak amplitude might be well above the strong coupling threshold and only the wings of the pulse exhibit amplitudes below the threshold, the full model Eqs. (3.15)-(3.17) needs to be taken into consideration. This means, the assumption to neglect weak coupling effects by omitting the first derivative with respect to time in Eq. (3.17) might deliver results describing the leading seed spike quite well, but highly overestimate the overall energy transmission efficiency. This is another potential reason why theory and experiment still vary very much in the predicted and measured efficiencies for Brillouin amplification.

6 Influence of pump chirp

In this chapter we investigate the influence chirping the pump has on the strongly coupled Brillouin amplification scheme. As introduced in Sec. 2.2, chirping a laser pulse with constant bandwidth in frequency or wavelength, alters its duration. This chapter has high experimental relevance, as in a Brillouin amplification setup, the two lasers usually originate from the same laser system. This implies, that a fixed bandwidth is given and in order to create the pump pulse, the formerly very short seed is stretched in time, and, thus, affected by chirp.

We investigate the influence of the sign of the chirp (see Sec. 2.2), as we can go from red-to-blue or from blue-to-red wavelengths. We show that the outcome highly depends on the sign of the chirp.

Furthermore, in this chapter we take note on the intrinsic chirp developing in a strongly coupled Brillouin amplification setup. This will eventually explain the form of the seed envelope undergone amplification, different from the weakly coupled or Raman scenario.

The chapter is organized as follows. In Sec. 6.1 we derive the three wave interaction model and explain in detail the differences from the basic one derived in Sec. 3.1. Afterwards, we draw conclusions on both the linear (Sec. 6.2) and pump depletion regime (Sec. 6.3). Then we discuss the formalism of the intrinsic chirp in Sec. 6.4 and comment on the choice of chirp rates according to real parameters available in experiments in Sec. 6.5. Afterwards, we summarize the results obtained in Sec. 6.6.

The content of this chapter was published in [62].

6.1 Multi-dimensional three-wave interaction model including chirp

We derive a three wave interaction model, extending Eqs. (3.15)-(3.17) by the chirp, simultaneously dropping the first derivative with respect to time in (3.17), as here we are only interested in the strong coupling regime.

We take the same initial Eqs. as in Sec. 3.1, but consider the three waves to be

$$\mathbf{a}_0 = \frac{1}{2}\left(A_0\left(x,y,t\right)\exp\left(\mathrm{i}\phi_0 + \mathrm{i}\alpha\phi_0^2\right) + c.c.\right)\hat{\mathbf{y}}, \qquad \phi_0 = \omega_0 t - k_0 x, \qquad (6.1)$$

$$\mathbf{a}_1 = \frac{1}{2}\left(A_1\left(x,y,t\right)\exp\left(\mathrm{i}\phi_1\right) + c.c.\right)\hat{\mathbf{y}}, \qquad \phi_1 = \omega_1 t + k_1 x, \qquad (6.2)$$

$$\frac{\delta n}{n_0} = \frac{1}{2}\left(n\left(x,y,t\right)\exp\left(\mathrm{i}\phi_2\right) + c.c.\right), \qquad \phi_2 = \omega_2 t - k_2 x, \qquad (6.3)$$

with complex envelopes $A_{0,1}$ and n, phases $\phi_{0,1,2}$ and a linear frequency chirp α instead of Eqs. (3.6)-(3.8). We consider the wave equation in weakly relativistic approximation, momentum balance and continuity equation. Afterwards, we apply some algebra, namely neglect of non-resonant contributions, slowly-varying envelope approximation and phase-matching $\phi_0 = \phi_1 + \phi_2$. For consistency with the former model Eqs. (3.15)-(3.17), we introduce new variables $n \to 2N$, $A_{0,1} \to -cE_{0,1}/\omega_0$ and $v_{g0,1} = c^2 k_{0,1}/\omega_{0,1}$. The three-wave interaction model then reads

$$\left[\frac{\partial}{\partial t} + v_{g0}\frac{\partial}{\partial x} - \frac{\mathrm{i}}{2}\frac{v_{g0}}{k_0}\frac{\partial^2}{\partial y^2} - \frac{\mathrm{i}}{2}\frac{c^2}{\omega_0^3}\frac{\partial^2}{\partial x^2} - \frac{3\mathrm{i}\omega_{pe}^2 e^2}{16 m_e^2 c^2 \omega_0^3}\left(|E_0|^2 + 2|E_1|^2\right)\right]E_0$$

$$= -\mathrm{i}\frac{\omega_{pe}^2}{2\omega_0}N E_1 \mathrm{e}^{-\mathrm{i}\alpha(\omega_0 t - k_0 x)^2}, \quad (6.4)$$

$$\left[\frac{\partial}{\partial t} - v_{g1}\frac{\partial}{\partial x} - \frac{\mathrm{i}}{2}\frac{v_{g1}}{k_1}\frac{\partial^2}{\partial y^2} - \frac{\mathrm{i}}{2}\frac{c^2}{\omega_1^3}\frac{\partial^2}{\partial x^2} - \frac{3\mathrm{i}\omega_{pe}^2 e^2}{16 m_e^2 c^2 \omega_1 \omega_0^2}\left(2|E_0|^2 + |E_1|^2\right)\right]E_1$$

$$= -\mathrm{i}\frac{\omega_{pe}^2}{2\omega_1}N^* E_0 \mathrm{e}^{\mathrm{i}\alpha(\omega_0 t - k_0 x)^2}, \quad (6.5)$$

$$\left[\frac{\partial^2}{\partial t^2} - c_s^2\frac{\partial^2}{\partial x^2} - c_s^2\frac{\partial^2}{\partial y^2}\right]N = -\frac{Ze^2 k_2^2}{4 m_e m_i \omega_0^2}E_0 E_1^* \mathrm{e}^{\mathrm{i}\alpha(\omega_0 t - k_0 x)^2}. \quad (6.6)$$

6.2 Effects on the linear regime

We first focus on the linear regime where we only have energy transmission from the high-energy pump to the low-energy seed and can thus neglect any change in E_0. Furthermore, we at first consider the one-dimensional case which is valid for large beam diameters and additionally neglect relativistic and dispersive effects. Hence Eqs. (6.4)-(6.6) reduce to

$$\left[\frac{\partial}{\partial t} - v_{g1}\frac{\partial}{\partial x}\right] E_1 = -\mathrm{i}\frac{\omega_{pe}^2}{2\omega_1} N^* E_0 e^{\mathrm{i}\alpha(\omega_0 t - k_0 x)^2}, \tag{6.7}$$

$$\frac{\partial^2}{\partial t^2} N = -\frac{Ze^2 k_2^2}{4m_e m_i \omega_0^2} E_0 E_1^* e^{\mathrm{i}\alpha(\omega_0 t - k_0 x)^2}. \tag{6.8}$$

From Eq. (6.1) we find

$$\frac{\partial}{\partial t}\left(\phi_0 + \alpha\phi_0^2\right) = \frac{\partial\phi}{\partial t} = \omega = \omega_0 + 2\alpha\omega_0\left(\omega_0 t - k_0 x\right),$$

$$\frac{\partial\phi}{\partial t} = \omega_0 + \tilde{\omega},$$

$$\rightarrow \tilde{\omega} = 2\alpha\omega_0\left(\omega_0 t - k_0 x\right).$$

When looking for the frequency change over time at a fixed position $x = x_0$ one finds

$$\frac{\Delta\omega}{\omega_0} = 2\alpha\omega_0\Delta t. \tag{6.9}$$

Operating in a low density regime enables the dispersion relation to be close to the one for vacuum. Thus we assume

$$\frac{\Delta k}{k_0} \approx \frac{\Delta\omega}{\omega_0} = 2\alpha\omega_0\Delta t. \tag{6.10}$$

The maximum frequency shift is limited by the (pump) pulse bandwidth $\Delta\omega < \Delta\omega_{\mathrm{bandwidth}}$.

However, we can also draw attention to the bandwidth of the instability which in the following is called Δk_Γ. From investigations of the amplification function $|A|$ in Eq. (5.1), we know that exponential growth of an amplified mode sets in after a duration of $\Delta t_\Gamma \approx 2/\Gamma_0$. Here, Γ_0 is the (exponential) growth rate determined by the amplitude $|E_0|$. A rough estimate from Eq. (6.10) is thus, that the chirp rate should be lower than

$$|\alpha| < \frac{\Delta k_\gamma}{2k_0\omega_0\Delta t_\Gamma}, \tag{6.11}$$

so that the time the pump needs to cover the instability bandwidth Δk_Γ is at least the time necessary for the specific modes to start growing exponentially Δt_Γ and

thus at a later stage entering the non-linear pump depletion regime. If we had a higher chirp-rate $|\alpha|$ than limited via Eq. (6.11) we would detune over Δk_Γ faster than Δt_Γ and thus amplification would be much reduced. Note that the instability bandwidth Δk_Γ grows larger for larger pump amplitudes $|E_0|$.
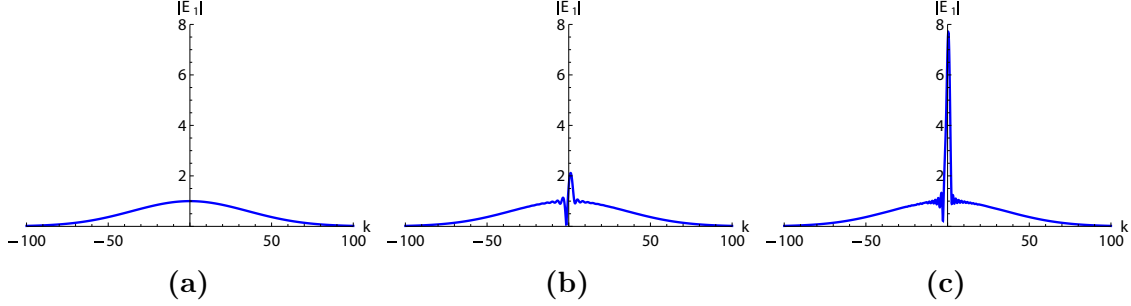

Figure 6.1: Analytic results for seed spectrum amplified in the linear phase. The initial seed (a) is at first asymmetrically altered (b), later the spectrum looks more symmetric (c).
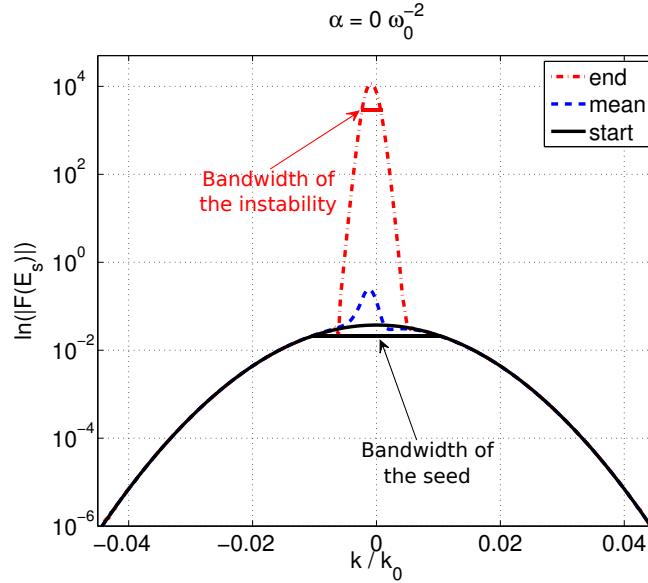
Figure 6.2: Examplary seed envelope spectrum at three different times in the amplification process in the linear regime. Shown is the pulse bandwidth Δk_seed and the instability bandwidth Δk_Γ. Parameters can be found in the text below, behavior is the same as for analytics (see Fig. 6.1).

We consider a seed pulse with a bandwidth of $\Delta \lambda_\mathrm{seed} = 18$ nm ($\Delta k_\mathrm{seed} \approx 2 \cdot 10^{-2} k_0$) which corresponds to a Fourier-limited duration of $\Delta \tau_\mathrm{seed} \approx 100$ fs full width half maximum. Its initial peak intensity is $I_0^s = 10^{12}$ W/cm^2 and the envelope has Gaussian shape. The pump pulse is as well Gaussian and has a peak intensity

of $I_0^p = 10^{16}$ W/cm^2 and a duration of $\Delta\tau_{\mathrm{pump}} \approx 4$ ps full width half maximum with an, at first, arbitrary chirp-rate α and, thus, arbitrary bandwidth $\Delta\lambda_{\mathrm{pump}}$. Since we at first consider one-dimensional simulations which are valid for large beam diameters we note the total pump energy per area to be $\Xi \approx 31.5$ kJ/cm^2. This seems to be a reasonably low number if one considers beam radii on the order of $r \approx 100$ μm. Thus we yield an energy on the order of 1 J. We find $\Delta k_\Gamma \approx 2 \cdot 10^{-3} k_0$ and $\Gamma_0 \approx 4.4 \cdot 10^{12}$ s^{-1}, which is similar to the growth rate calculated for plane waves with the peak intensity of the pump. We operate in a plasma with a density of $n_0 = 0.01 n_c \approx 1.7 \cdot 10^{19}$ cm^{-3} and have a central laser frequency of $\omega_0 \approx 2.35 \cdot 10^{15}$ s^{-1}. Hence from the criterion Eq. (6.11) we find $|\alpha| \lesssim 1 \cdot 10^{-6} \omega_0^{-2} \equiv |\alpha_{\mathrm{crit}}|$.

Fig. 6.3 shows simulation results for parameters as given above for two different scenarios for the linear phase: Each figure consists of four graphs, in solid black one finds the initial seed spectrum, in dashed blue the spectrum during and in dash-dotted red the spectrum after the amplification process. The dotted green line marks the maximum pump amplitude ($E_0^0 \approx 0.068$) which has to be surpassed in order to reach the pump-depletion regime. In Fig. 6.3a we have a chirp-rate of $|\alpha| < |\alpha_{\mathrm{crit}}|$ and thus see that the seed amplitudes grows larger than the pump's (dash-dotted red). On the other hand in Fig. 6.3b we have $|\alpha| > |\alpha_{\mathrm{crit}}|$ and see that the seed does not grow larger than the pump and thus we will not enter the pump-depletion regime.

(a) (b)
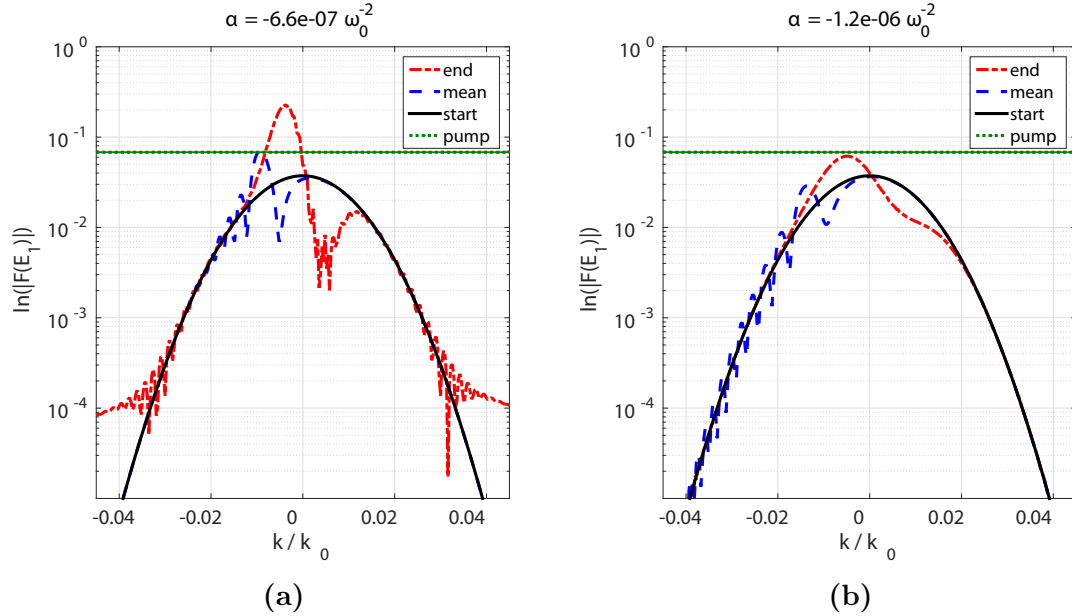
Figure 6.3: Simulation results for parameters as specified in text which results in a criterion $|\alpha| \lesssim 1 \cdot 10^{-6} \omega_0^{-2}$. Fig. (a) has $|\alpha| < |\alpha_{\mathrm{crit}}|$ and thus the seed gets larger than the pump. Fig. (b) has $|\alpha| > |\alpha_{\mathrm{crit}}|$ and hence the seed stays lower in amplitude.

This example is in very good agreement to our derived criterion. The same is true for positive chirps as one finds in Fig. 6.4.
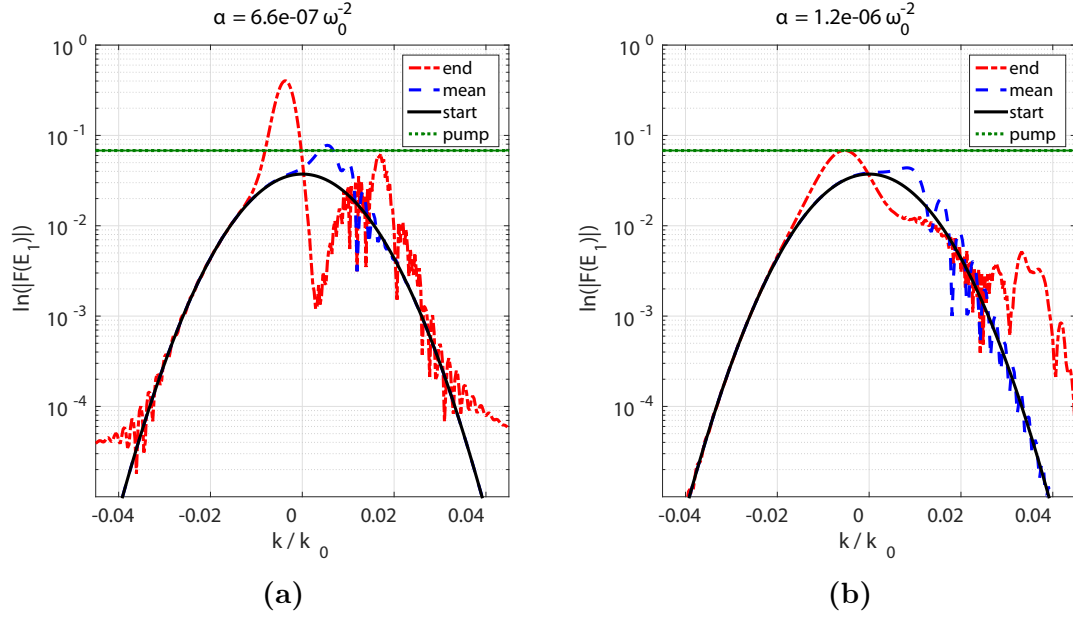

(a)   (b)

Figure 6.4: Simulation results for parameters as specified in text which results in a criterion $|\alpha| \lesssim 1 \cdot 10^{-6}\omega_0^{-2}$. Fig. (a) has $|\alpha| < |\alpha_{\mathrm{crit}}|$ and thus the seed gets larger than the pump. Fig. (b) has $|\alpha| > |\alpha_{\mathrm{crit}}|$ and hence the seed stays lower in amplitude.

Note that in [62] there is also a complete analytic theory found to describe and match growth and envelope change in the linear regime.

6.3 Pump depletion regime

Next, we consider multiple one-dimensional observations again without transverse dependence, dispersion and relativistic mass increase, thus considering the model

$$\left[\frac{\partial}{\partial t} + v_{g0}\frac{\partial}{\partial x}\right]E_0 = -\mathrm{i}\frac{\omega_{pe}^2}{2\omega_0}N E_1 \mathrm{e}^{-\mathrm{i}\alpha(\omega_0 t - k_0 x)^2}, \tag{6.12}$$

$$\left[\frac{\partial}{\partial t} - v_{g1}\frac{\partial}{\partial x}\right]E_1 = -\mathrm{i}\frac{\omega_{pe}^2}{2\omega_1}N^* E_0 \mathrm{e}^{\mathrm{i}\alpha(\omega_0 t - k_0 x)^2}, \tag{6.13}$$

$$\frac{\partial^2}{\partial t^2}N = -\frac{Ze^2 k_2^2}{4m_e m_i \omega_0^2}E_0 E_1^* \mathrm{e}^{\mathrm{i}\alpha(\omega_0 t - k_0 x)^2}. \tag{6.14}$$

We perform simulations modeling Eqs. (6.12)-(6.14) with the same parameters as mentioned in Sec. 6.2, but for a longer pump duration of $\Delta t_{\mathrm{pump}} \approx 6$ ps and thus a higher pump energy per area of $\Xi \approx 47.2$ kJ/cm^2.

Fig. 6.5 shows multiple one-dimensional simulations both spatially and chirp-rate α resolved, where the color scale determines the amplitude of seed or pump, respectively. While the spatial resolution is shown on the x-axis one finds α on the y-axis. The seed on the left is always shown at the same time as the pump on the right. With the aforementioned criterion Eq. (6.11) we estimate reasonable chirp-rates to resolve to be $|\alpha| < 1.5 \cdot 10^{-6}\omega_0^{-2}$. Note that this simulation is performed in a co-moving frame of the seed.

Fig. 6.5a shows the initial seed pulses as a blue bar on the left, in this co-moving frame standing still. The pump gets radiated from the left into the simulation box and the initial scenario is shown in Fig. 6.5b. After roughly 3.8 ps the seed amplification process has reached the end of the linear phase and one finds an amplified tail drawn behind the leading front (Fig. 6.5c). The pump has at this stage (Fig. 6.5d) entered the simulation box but so far has not lost any energy.

After about 7.5 ps for particular chirp-rates around $\alpha \approx 0$ one finds an amplified seed as is shown by the bright color (Fig. 6.5e). At the same moment one sees depletion in the pump's amplitude (and thus energy) in Fig. 6.5f for the same chirp-rates one finds amplification. After 11.3 ps the pump (Fig. 6.5h) has left the simulation box and got filtered, whereas the seed has developed it's final form.

In Fig. 6.5g one finds around $|\alpha| \approx 0$ a high peak in amplitude and after it there are several oscillations following. This is a very characteristic behavior for the amplification process in the pump depletion regime. For lower α one does not find any amplification. For higher chirp-rates one finds only one maximum very far behind the initial seed and almost no trailing oscillations.
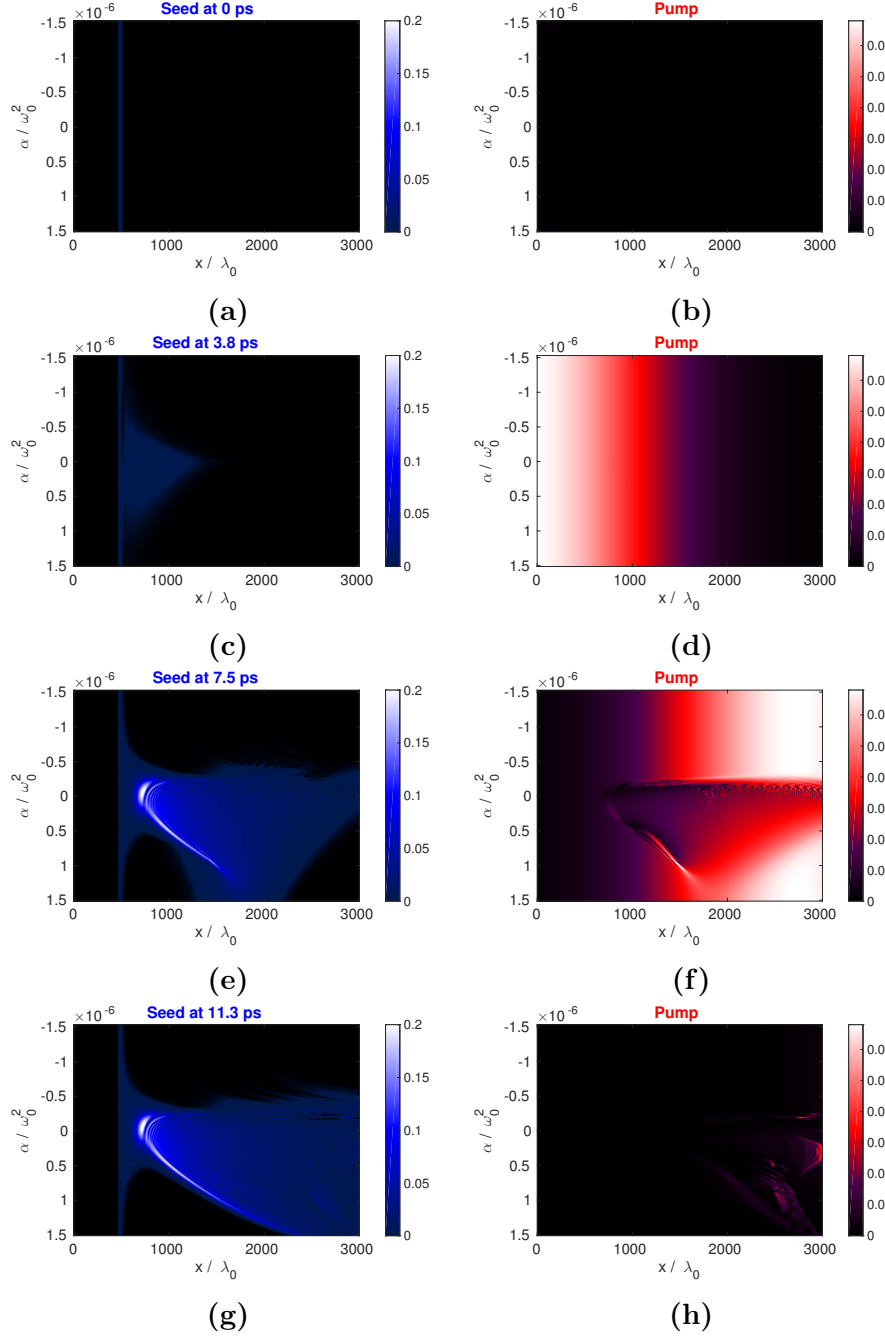
Figure 6.5: Multiple one-dimensional simulation results for parameters as specified in text. Shown are seed (left column) and pump (right column) pulse at different times in the co-moving frame with respect to the seed. On the x-axis there is spatial, on the y-axis there is chirp-rate resolution, color represents the respective amplitude. Fig. (g) shows the seed after the amplification: around $\alpha = 0$ one finds typical behavior with a leading maximum and many oscillations behind. For $\alpha > 0$ one finds one isolated maximum further behind the initial seed.

We focus on three distinct chirp-rates α in order to show the vast amount of tunability chirp introduces. Fig. 6.6 is organized as follows: On top the seed is shown in three different stages, in black it is the initial pulse, in dashed blue after the linear regime and in solid blue after the pump depletion regime. On the bottom there is the spectrum with the same color code as on top.
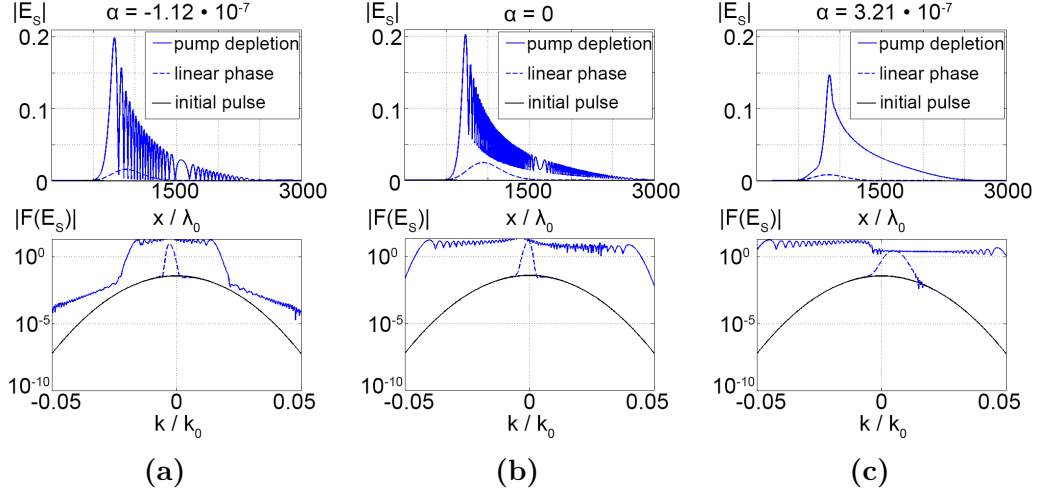
Figure 6.6: Seed in space (top) and k (bottom) for three different chirp-rates α (left to right) in the three different states (initial: black, linear phase: dashed blue, pump depletion regime: solid blue).

In Fig. 6.6b we find the unchirped case $\alpha = 0$. As mentioned in Sec. 3.2 this is a very characteristic solution: In the linear stage the seed draws a tail whose amplitude grows exponentially and can be described analytically. When the seed is in the pump depletion regime one finds self-similar behavior as the leading maximum continues growing, but only polynomially, and it drags oscillations behind. In the spectrum one can again see the bandwidth of the seed (black) and of the instability (dashed blue). After entering the pump depletion regime (solid blue) the spectrum gets broader and is more or less symmetric.

For the negative chirp $\alpha \approx -1.18 \cdot 10^{-7} \omega_0^2$ (Fig. 6.6a) one finds that the oscillations behind the leading maximum that establish in the pump depletion regime at one point go down to the bottom. The spectrum is narrower and more symmetric than without any chirp. For positive chirp $\alpha \approx 3.21 \cdot 10^{-7} \omega_0^2$ we find a very localized pulse without any oscillations in the non-linear stage of the amplification process. The spectrum gets broader and is less symmetric than in the unchirped case.

The asymmetry of the spectrum in the unchirped case was already discussed in Ch. 5, where we discussed the detuning δk. By applying a chirp, we can either increase or decrease this effect, depending on the sign.

The goal of parametric amplification processes is both retaining high energy transmission efficiency and also generation of ultra-high peak power of an amplified laser pulse. Fig. 6.7 shows a chirp-rate resolved graph for the peak amplitude (normalized to 1, dashed red) and transmission efficiency η (blue). The value η is obtained by dividing the difference between final and initial seed energy per area by the total pump energy per area.

We find that for $\alpha \approx -1.18 \cdot 10^{-7} \omega_0^2$ (as presented in Fig. 6.6a) we increase both the final amplitude of the seed and the efficiency in comparison to the unchirped case. For the positive chirp-rate $\alpha \approx 3.21 \cdot 10^{-7} \omega_0^2$ we find a lower final amplitude and efficiency, but as a trade-off we yield a smooth and isolated seed as shown in Fig. 6.6c.

The reason for that increase or decrease, respectively, of the efficiency lies again in the spectrum. By chirping, we either push the resonance away or stay resonant. A mechanism further complicating that process is discussed in the next section, where we introduce the concept of the intrinsic chirp.
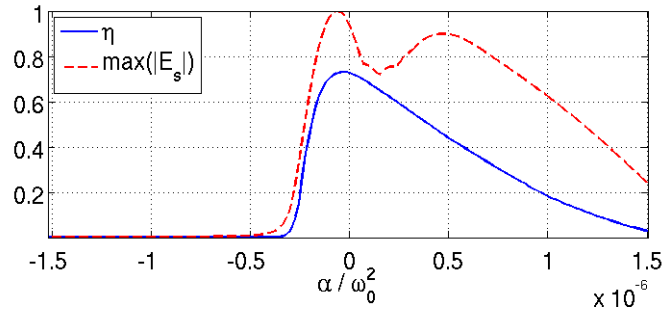
Figure 6.7: Normalized peak amplitude after amplification (dashed red) and energy transmission efficiency from pump to seed (solid blue) for different chirp-rates α.

6.4 Intrinsic chirp developing during strongly coupled amplification

In this section, we take a closer look at the seed in the non-linear stage. We found that the seed resembles a non-linear oscillator and intrinsically experiencing a chirp: The homogeneous solution to Eq. (6.14) for $\alpha = 0$ is

$$N_{\text{hom}} = \beta t, \tag{6.15}$$

with an arbitrary constant β. We focus on plane waves, thus spatial derivatives vanish. Next we state at a certain point in time the two waves are similar $E_0 \approx E_1$, namely when pump depletion sets in. Inserting Eq. (6.15) into Eq. (6.13) yields

$$\frac{\partial}{\partial t} E_1 = -\mathrm{i}\beta \frac{\omega_{pe}^2}{2\omega_1} t E_1, \tag{6.16}$$

which has the solution

$$E_1 = E_1^0 \mathrm{e}^{-\mathrm{i}\beta \frac{\omega_{pe}^2}{4\omega_1} t^2}. \tag{6.17}$$

Apparently we find an intrinsic chirp applied to the seed (and simultaneously to the pump) during amplification in the pump-depletion regime.

In the following we present simulational results for the model (6.12)-(6.13) for the same laser-plasma parameters as specified in Sec. 6.2. Fig. 6.8 shows the seed envelope in the pump-depletion regime (upper panel) for a vanishing chirp-rate of the pump $\alpha = 0$. The lower panel shows the derivative of the seed phase (solid blue), thus the wave-number, spatially resolved. We find a behavior that is characteristic for a non-linear oscillator with fast changes in wave-number (peaks) whenever there is a dip in the seed envelope. Spatially, we find, on average, a linear variation of the wavenumber from head to tail of the seed, as is shown in solid red. This linear decrease in wave-number corresponds to a chirp that gets applied to the seed pulse from front to end in the nonlinear regime.

With this result we immediately understand the asymmetry for positive and negative chirp as shown for instance in Fig. 6.7: An additional chirp applied to the pump pulse can only alter the seed from this "offset"-chirped scenario, intrinsically gained during a regular, non-chirped amplification process. This is also in very good agreement with observations made via analytic self-similarity theory, see e.g. [92, 62].
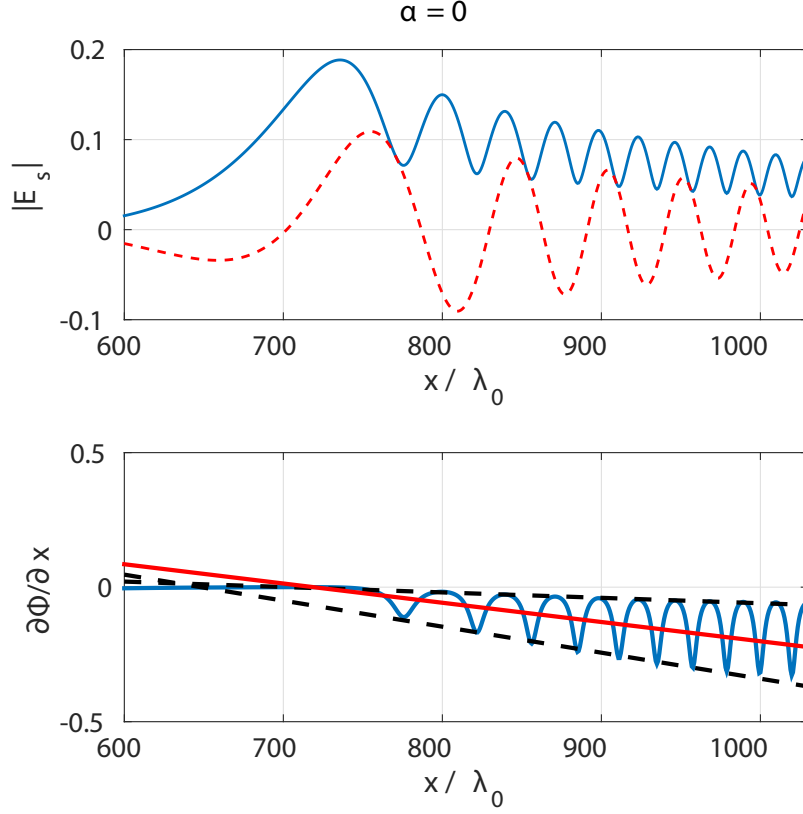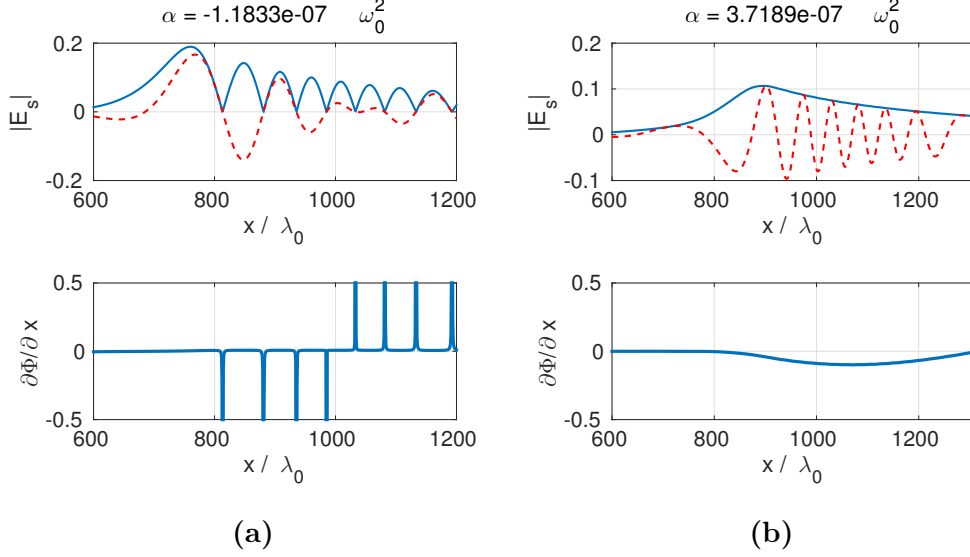
Figure 6.8: Seed envelope $|E_s|$ (blue) and oscillating field $\Re(E_s)$ (dashed red, both
top) over space at a given time and the wave-number over space in
the seed (bottom) for a vanishing pump chirp-rate α. The latter is
enveloped by two lines (dashed black) and results in a weighted average
wave-number (red) which changes linearly from front to end. This can
also be seen in the oscillating field: two neighboring peaks get closer
to each other from front to end. This is a characteristic behavior for a
non-linear oscillator and also in good agreement to self-similar theory
observations and witnesses the intrinsic chirp the seed yields during the
pump-depletion regime.

Now we look a bit more into detail for the chirped (pump) scenarii. Fig. 6.9 is
built up like Fig. 6.8, on top there is the seed envelope, on the bottom there is the
wave-number of the seed, both spatially resolved.

Fig. 6.9a shows the negative chirp-rate, where the resulting seed looks like a
Raman amplified pulse (oscillations going to the bottom). The red line in the
lower panel, which has a vanishing slope, is again the weighted average of the
wave-number over space. It tells us that with this pump chirp-rate we compensated
the intrinsic chirp gained during the pump-depletion regime. In Raman (or weakly
coupled Brillouin) amplification one does not find an intrinsic chirp.
However, when chirping the pump pulse with a positive rate (Fig. 6.9b) we see

that we get rid of the behavior as a non-linear oscillator: No longer are there steep peaks in the spatial wave-number but a very smooth profil (bottom). Therefore we do no longer see oscillations in the envelope but this isolated pulse (top).

(a)

(b)

Figure 6.9: Seed envelope (blue) and oscillating field (dashed red, both top) over space at a given time and the wave-number over space in the seed (bottom) for a negative (a) and positive (b) pump chirp-rate α. In (a) the intrinsic chirp (linear wave-number change, see Fig. 6.8) gets compensated and thus we end up with a Raman-like pulse. In (b) the non-linear oscillations have vanished, thus ending up with an isolated pulse.

6.5 Available parameters in experiments

One should keep in mind that pump duration Δt_{pump}, pump chirp-rate α and pump bandwidth $\Delta\lambda_{\text{pump}}$ cannot be chosen independently, but are connected via the relation

$$\alpha = \frac{\sqrt{\Delta\omega^2 \Delta t_{\text{pump}}^2 - 64\ln(2)^2}}{2\Delta t_{\text{pump}}^2}, \tag{6.18}$$

with $\Delta\omega = 2\pi c\Delta\lambda/\lambda_0^2$. So far, we kept the duration constant and changed the chirp-rate, thus changed the bandwidth from which the pump pulse is created. In experiments, scientists typically use one laser setup to generate two laser pulses for pump-seed amplification, thus both laser pulses have the same bandwidth. The chirp-rates α used for the simulations shown above with a pump duration of Δt_{pump} would correspond to a pump bandwidth of $\Delta\lambda_{\text{pump}} \approx 7.3$ nm (for $\alpha \approx -1.18 \cdot 10^{-7}\omega_0^2$) or $\Delta\lambda_{\text{pump}} \approx 2.7$ nm (for $\alpha \approx 3.21 \cdot 10^{-7}\omega_0^2$), respectively. The seed bandwidth is $\Delta\lambda_{\text{seed}} = 18$ nm and when choosing this also for the pump bandwidth one ends up at $|\alpha| \approx 7.95 \cdot 10^{-7}\omega_0^2$. This would be a chirp rate that is too low for operating in a favorable regime, as can be seen in Fig. 6.7.

In order to find out what we could do when we use the same bandwidth for both pump and seed, and also the same energy per area, but only vary the pump duration, we perform a new parameter scan as is shown in Fig. 6.10. On the left, one finds the seed, again in a co-moving frame and with the same parameters as before. The x-axis is again spatial resolution and the y-axis represents the pump duration with the corresponding (positive) chirp-rate α calculated via Eq. (6.18). On the right one finds the pump, which again gets radiated into the simulation box from the left.

The shortest pump duration is $\Delta t_{\text{pump}} = 10\Delta t_{\text{seed}}$, thus roughly 1 ps, the longest is $\Delta t_{\text{pump}} \approx 180\Delta t_{\text{seed}}$, thus roughly 18 ps.

Fig. 6.11 is constructed the same way as was Fig. 6.10, but here the chirp is set to zero.
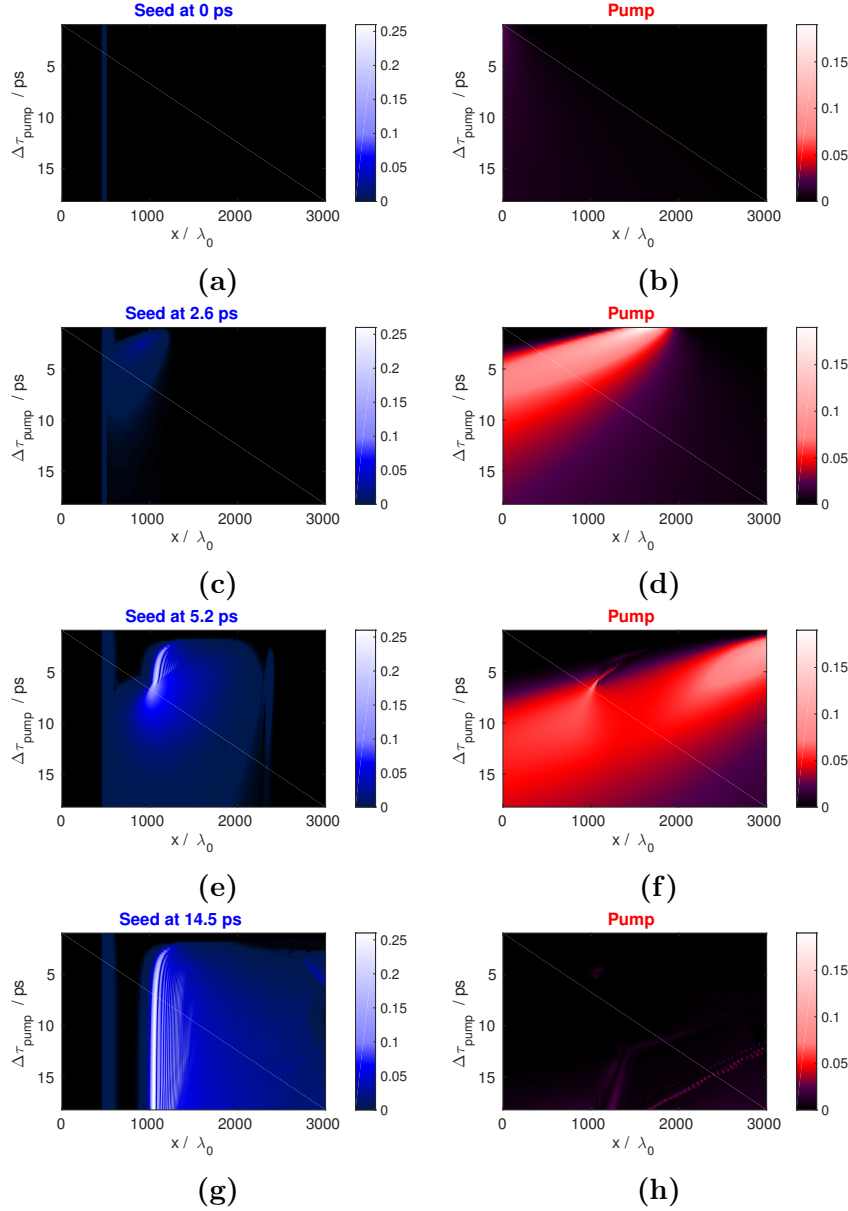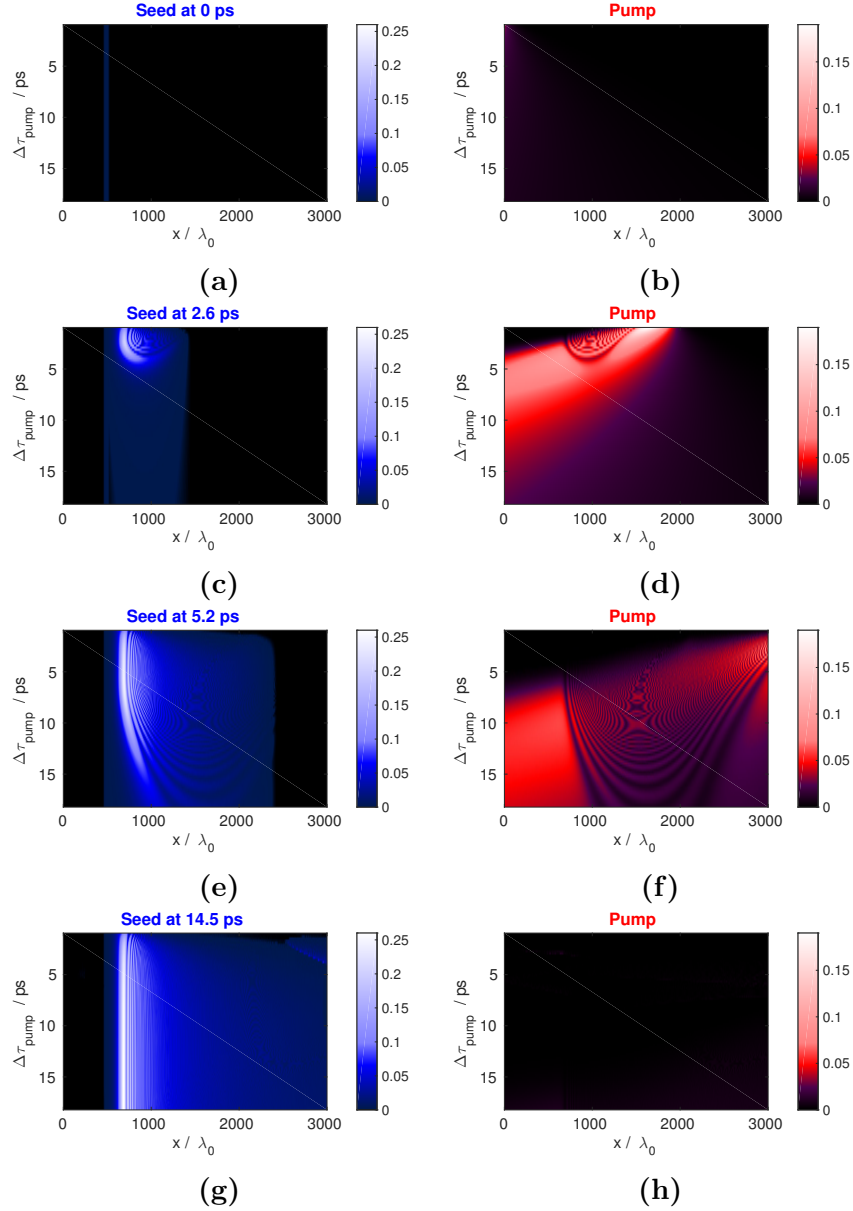
Figure 6.10: Multiple one-dimensional simulation results for positive chirp rate α with parameters as specified in text. Shown are seed (left column) and pump (right column) pulse at different times in the co-moving frame with respect to the seed. On the x-axis there is space, on the y-axis there is the pump duration resolved, color represents the respective amplitude. The pump always carries the same energy (per area) but changes its duration and thus the chirp-rate α according to Eq. (6.18) and its peak intensity

Figure 6.11: Multiple one-dimensional simulation results for vanishing chirp rate α with parameters as specified in text. Shown are seed (left column) and pump (right column) pulse at different times in the co-moving frame with respect to the seed. On the x-axis there is space, on the y-axis there is the pump duration resolved, color represents the respective amplitude. The pump always carries the same energy (per area) but changes its duration and thus the chirp-rate α according to Eq. (6.18) and its peak intensity

Fig. 6.12 summarizes the results obtained from the simulations presented in Figs. 6.10 and 6.11. Here, we show the energy transmission efficiency η depending on the pump duration Δt_{pump}, while the latter was evaluated for an original bandwidth

of 18 nm.

It is readily found, that respecting the influence of the chirp only decreases the energy transmission efficiency η. This was obtained by using the real relationship between pump duration and chirp, assuming the pump originates from the same laser as the seed, which implies both having the same bandwidth. Furthermore, the sign of α is fundamental, as simulations indicate that $\alpha < 0$ decreases the energy transmission to a negligible amount. A negative chirp-rate implies going from blue-to-red wavelengths from front-to-end of the pump.
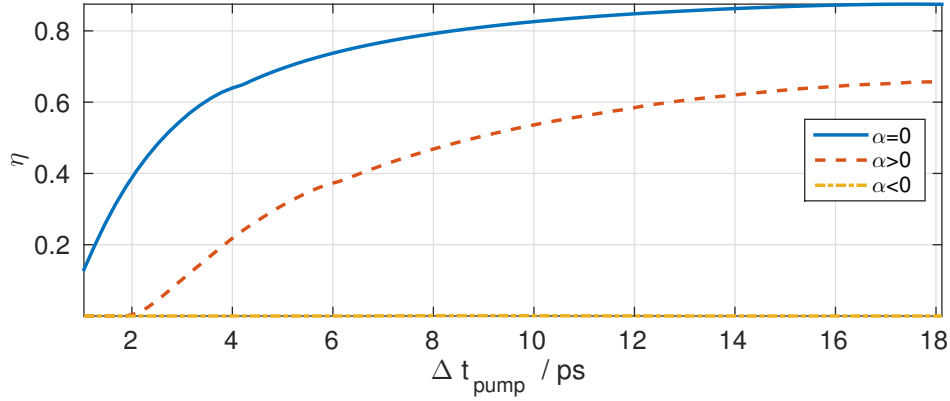
Figure 6.12: Efficiency of energy transmission from pump to seed pulse, pump duration resolved. The pump always carries the same energy (per area) but changes its duration and thus the chirp-rate α according to Eq. (6.18) and its peak intensity. The solid blue line corresponds to the simulations presented in Fig. 6.11 for $\alpha = 0$, the dashed red line to Fig. 6.10 for $\alpha > 0$ and the dash-dotted yellow line to $\alpha < 0$.

6.6 Conclusion

In this chapter we have derived the (multi-dimensional) three-wave-interaction model including chirp for strongly coupled Brillouin amplification in Sec. 6.1. Consecutively in Sec. 6.2, we formulated an analytic estimate, how large the chirp rate α should be to cover the full seed spectrum and entirely amplify it linearly, just like what was done in [61] for weak coupling.

Afterwards, we commented on the pump depletion regime in Sec. 6.3 and presented different resulting amplified seed envelope forms when allowing to choose an arbitrary chirp rate α. Here, we could create envelopes that looked very similar to those obtained from weak coupling or Raman amplification (see Ch. 5 for comparison) and showed that we can increase the energy transmission efficiency η and also the maximum peak amplitude of the seed.

However, in the course of investigation, we found that for strongly coupled Brillouin amplification, there is always an intrinsic chirp getting applied to both seed and pump in the nonlinear regime. We have shown where this intrinsic chirp originates from by investigating the model equations (6.4)-(6.6). We investigated how we can compensate it by applying a negative pump chirp in Sec. 6.4.

Commenting on Brillouin experiments, we summarized what happens if pump and seed are generated from the same laser oscillator with a constant bandwidth $\Delta\lambda$ in Sec. 6.5 via a large parameter scan. We marked strong differences in the energy transmission efficiency η depending on the sign of the chirp and rendered a positive one as favorable. However, overall the efficiency decreases when considering a constant bandwidth for both laser pulses and the chirp necessary for stretching the pump. This is one of the reasons why strong coupling Brillouin amplification experiments have not yet reached efficiencies obtained by numerical simulations.

7 Theory support of experiments

The following chapter consists of calculations and simulations which were performed to optimize experiments.

In Sec. 7.1 post-processing simulations for an sc-SBS experiment performed by T. Gangolf *et al.* in Düsseldorf are presented. The main reasons for low efficiency were identified as spontaneous Raman backscattering of the pump as well as radiation absorption due to inverse bremsstrahlung.

Sec. 7.2 comments on and calculates molecular Hydrogen plasma ionization dynamics, ranging from dissociation to direct laser heating via inverse bremsstrahlung. These investigations were performed to support experiments supposed to take place in Düsseldorf in November 2016 by T. Gangolf *et al.*.

Sec. 7.3 consists of the pursuit of finding the optimal pump pulse duration and according pump chirp, sign included. This one-dimensional parameter scan was performed for J.-R. Marques *et al.* at *LULI*, France in May 2015.

7.1 Spontaneous Raman backscattering

The data about an sc-SBS experiment in Düsseldorf performed by the experimental group around T. Gangolf *et al.* was received and yielded a relatively low energy transmission efficiency. For the reasons were unknown, simulations with the PIC code EPOCH [85, 86] were performed. PIC codes include more physical effects than reduced Maxwell-fluid models, which is why we chose that simulation method. The parameters were $\lambda_0 = 800$ nm for both pump and seed central wavelength, full width half maximum (in intensity) duration of $\sigma_p = 3$ ps and $\sigma_s = 30 - 300$ fs, where the lower case index p and s denotes pump and seed, respectively. As peak intensities we used $I_p^0 = 3 \cdot 10^{15} - 3 \cdot 10^{16}$ W/cm^2 and $I_s^0 = 8 \cdot 10^{13} - 8 \cdot 10^{14}$ W/cm^2. The varying seed intensity constitutes because the total seed energy was conserved throughout the whole experiment, thus the larger intensity corresponds to the shorter duration. The whole measurement yielded only an amplification factor of 2 as maximum over many different shots and pulse delay combinations, hence there was some disambiguity in the actual total energy carried by the pump, which is why we simulated a range of pump intensities. The lower one mentioned above was measured in a transition measurement, where no seed was involved and only the pump propagated through the plasma. However, the initially radiated pump intensity was supposed to be $I_p^0 = 3 \cdot 10^{16}$ W/cm^2.

The plasma was assumed to be ionized Hydrogen with a density of $n_0 \approx 0.09 n_c$, corresponding to $\approx 1.57 \cdot 10^{20}$ cm^{-3} at maximum, consisting of a Gaussian slab with full width half maximum broadness of $\sigma_n \approx 625\lambda_0 \approx 500~\mu$m.

A first simulation, testing just the single pump or seed pulse, respectively, passing through the plasma yielded that the pump (here: $I_p^0 = 3 \cdot 10^{15}$ W/cm^2) will backscatter spontaneously via the Raman instability. Fig. 7.1 shows two snapshots of the pump intensity (upper frame) and the density (lower frame) (Fig. 7.1a). Travelling from left to right, the pump will reflect off the density wave that gets amplified by the pump front due to plasma inhomogenities (Fig. 7.1b).

From the observations made in Fig. 7.1 we note that the experiment is very sensitive to the pulse delay, i.e. where and when in the plasma the two pulses overlap. For optimal energy transmission efficiency, we want the seed to start interfering with the pump roughly at the snapshot presented in Fig. 7.1a, as here there has not happened any spontaneous backscattering.

Fig. 7.2 shows two simulations for $I_p^0 = 3 \cdot 10^{15}$ W/cm^2 (Fig. 7.2a) and $I_p^0 = 3 \cdot 10^{16}$ W/cm^2 (Fig. 7.2b), where the delay is set to match the optimal conditions mentioned above. The seed intensity is in both cases $I_s^0 = 8 \cdot 10^{14}$ W/cm^2 and the duration is $\sigma_s = 30$ fs. The result does not change significantly as the seed either enters the nonlinear phase and gets amplified by a large factor as can be seen in Fig. 7.2a. Or the pump triggers spontaneous backscattering this early in the interaction such that there is no seed amplification observable as can be seen in Fig. 7.2b.
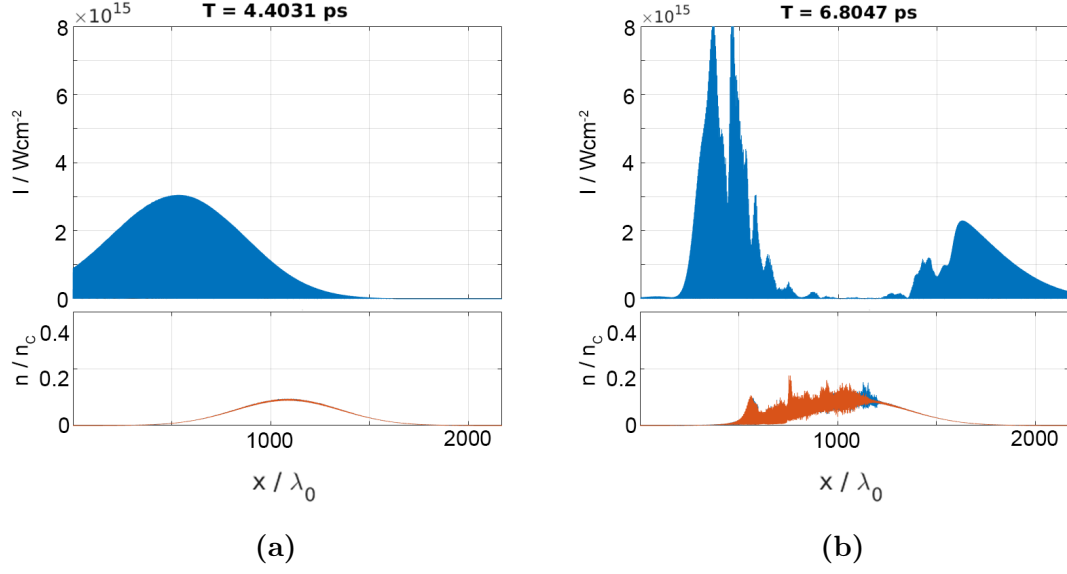
Figure 7.1: Simulation of a pump passing through plasma from left to right. After some time (b) spontaneous backscattering happens.
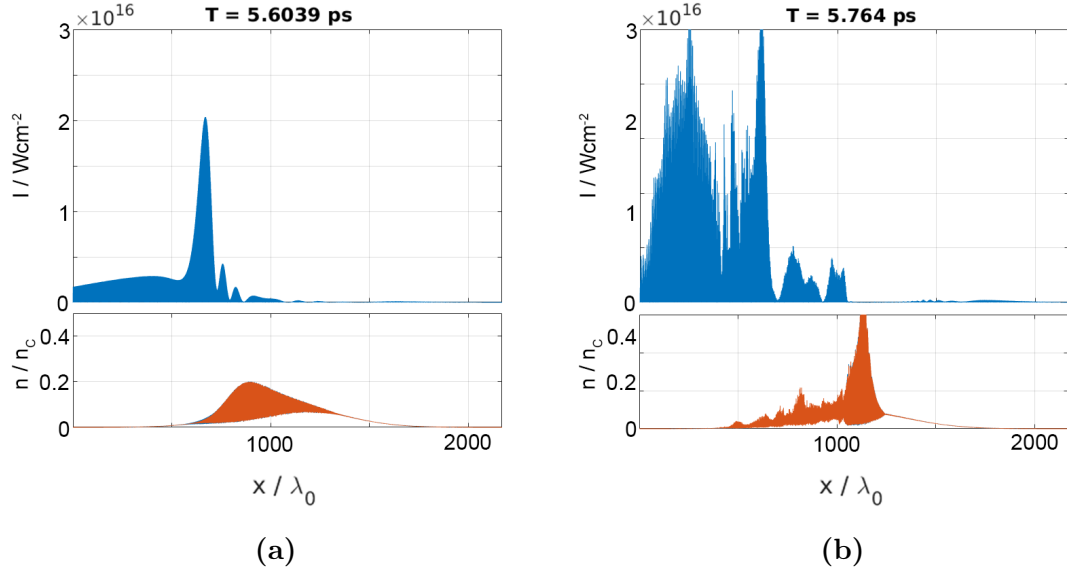

Figure 7.2: Seed-pump interaction for low (a) and high (b) pump strength. We find seed amplification in case of (a) and essentially spontaneous Raman backscattering in case of (b).

In our post-experiment analysis we found out that presumably the majority of the pump intensity got backscattered via spontaneous Raman scattering right at the plasma front. This leaves only a fraction of the pump to propagate through the plasma, a possible explanation why the pump peak intensity measured in the transmission experiment was about 10 times less than the initial intensity.

If the initial intensity would have been $\propto 10^{15}$ instead of $\propto 10^{16}$ W/cm^2, seed amplification by several orders of magnitude would have been predicted by our PIC simulations.

7.2 Plasma ionization

In this section we discuss the topic of ionization of a gas jet in experiments. In the previous section, one of the reasons given for a lack of visible seed amplification was spontaneous Raman scattering. Here, we bring in another effect, namely, collisional absorption of radiation, i.e. inverse bremsstrahlung, as a major loss effect if the plasma is not heated up to a certain temperature.

Usually, in Brillouin amplification experiments, there is a third laser pulse involved, that should ionize a gas jet and heat the target to reduce collisional damping of the pump and seed laser to a minimum. We focus on a molecular Hydrogen, i.e. H_2, gas jet with 10 % critical density, as depicted in Fig. 7.3.
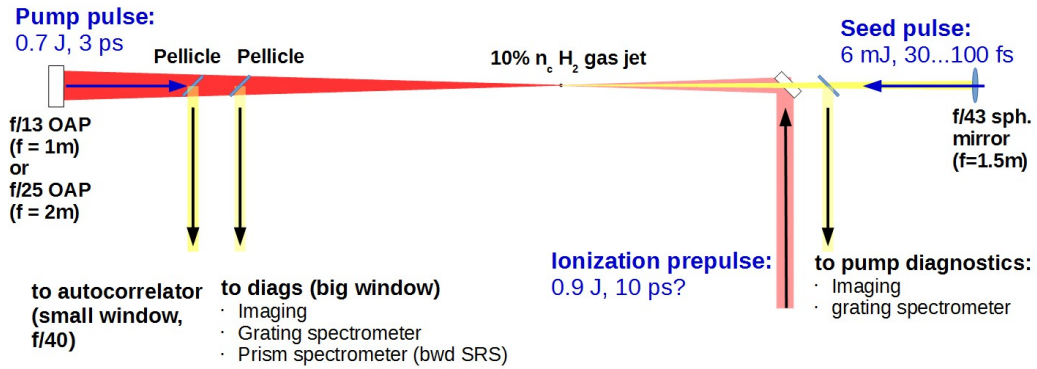
Figure 7.3: Schematic experimental setup for the Brillouin amplification experiment planned in November 2016 in Düsseldorf. By courtesy of T. Gangolf.

One of the problems investigating both dissociation of molecular Hydrogen and collisional absorption of laser light is that none of these can be investigated using PIC codes as they simply do not include these effects.

However, for dissociation it can be found [94, 95] that a laser intensity of $I \approx 5 \cdot 10^{13}$ W/cm^2 should be sufficient to dissociate the molecules and yield atomic Hydrogen, i.e. this is a problem already solved by sufficiently intense radiation.

The search for an optimal ionization and heating beam such that pump and seed pulses are not affected by inverse bremsstrahlung losses is more complicated or, respectively, needs easier analytic models. From [37, 41, 80, 82] we find the formula

$$f_A = 1 - \exp\left(-\frac{8\nu_{ei}L}{3c}\right), \tag{7.1}$$

that defines the fractional absorption of light in a linear density profile. Although a linear density profile is not a good approximation for the rather Gaussian or

Lorentzian shaped profile obtained from a gas nozzle described in Fig. 7.3, it is valid to get a first idea. The value L depicts the length of the plasma slab, c is the speed of light and ν_{ei} is the collision frequency between electrons and ions, given by Eq. (2.16), also known as the Spitzer formula [88]. The Coulomb-logarithm was evaluated with the Debye length v_{the}/ω_{pe} or with v_{the}/ω_0, respectively, and the classical minimum distance $Ze^2/k_B T_e$ for $T_e = 100$ eV, as was the goal in this experiment. The value therefore ranged from $\log \Lambda \approx 6.2 - 7.3$.

However, this evaluation would result in a fractional absorption of $f_A = 1$, i.e. the whole pump pulse would be absorbed if it would pass such a 100 eV plasma. Our analytics have shown that a plasma temperature of $T_e \approx 1$ keV would be favorable, however difficult it may be to achieve.

A more detailed analytic look into the heating mechanism of the plasma by the pump laser depicted in Fig. 7.3 follows the scheme mentioned in [96, 97] for a stationary, pre-ionized, homogeneous and initially cold plasma and shown in Eqs. (7.2)-(7.4) with Fig. 7.4.
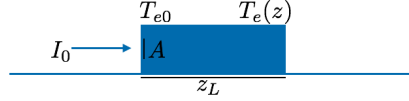
Figure 7.4: Schematic laser heating of a cold plasma as described in [96, 97].

$$T_{e0}\left(t_{end}\right) = \left(\frac{5}{3}\frac{\kappa}{n_e k_B}\Phi\left(t_{end}\right)\right)^{2/5}, \tag{7.2}$$

$$T_e\left(z, t_{end}\right) = \left(T_{e0}\left(t_{end}\right)^{3/2} - \frac{3}{2}\kappa z\right)^{2/3}, \tag{7.3}$$

$$\kappa = 10^{-16} Z \frac{n_e^2}{n_c} \log \Lambda. \tag{7.4}$$

In Fig. 7.4 we schematically describe an incident laser with intensity I_0 shining on a target of surface A, where the target has the length z_L and the temperatures T_{e0} and $T_e(z)$ at the radiated site or in the target, respectively. With the formulas (7.2)-(7.4), the temperatures in the target can be calculated, while $\Phi(t_{end})$ denotes the total flux, i.e. the energy per area, that is radiated through the target. With the parameters given in Fig. 7.3, we assume the ionization and heating prepulse to carry 0.9 J of energy and the area of incidence to be $A \approx 0.3 - 1.3 \cdot 10^{-4}$ cm^2. With these values we calculate the total energy flux to be $\Phi\left(t_{end}\right) = 0.7 - 3$ kJ/cm^2 and finally the temperature at the radiated front to be $T_{e0} \approx 200 - 350$ eV and at the rear to be $T_e(z_L) \approx 130 - 300$ eV. The actual value depends on which area of incidence A and which definition of the Coulomb logarithm $\log \Lambda$ we choose.

This means that the goal of an electron temperature of roughly 100 eV is achieved. However, according to Eq. (7.1) it would still be much too low and consequently result in a completely absorbed pump pulse. In order to properly simulate heating and collisional absorption, usage of codes like LASNEX [98] is required. LASNEX was also used in [96], but unfortunately, this code is not publicly available. We tried to use the code MULTI [99], which is often used for simulations concerning laser fusion, but it is only applicable for overdense plasmas. Thus, we could not find any computational setup to properly simulate the heating of the plasma by the ionizing prepulse and the absorption via inverse bremsstrahlung of the pump pulse. However, since we evaluated the fractional absorption with Eq. (7.1), we strongly recommend to use a higher plasma temperature, achievable with a prepulse carrying more energy.

7.3 Chirp and duration of pump pulse

We were asked by the group around J.-R. Marques to find the optimal pump pulse duration with respect to chirp for a Brillouin amplification experiment at *LULI* in France.

We simulate the one-dimensional three-wave interaction model

$$\left[\frac{\partial}{\partial t} + \frac{\partial}{\partial x}\right] E_p = -\mathrm{i} N E_s \mathrm{e}^{-\mathrm{i}\alpha(\omega_0 t - k_0 x)^2}, \tag{7.5}$$

$$\left[\frac{\partial}{\partial t} - \frac{\partial}{\partial x}\right] E_s = -\mathrm{i} N^* E_p \mathrm{e}^{\mathrm{i}\alpha(\omega_0 t - k_0 x)^2}, \tag{7.6}$$

$$\frac{\partial^2}{\partial t^2} N = -\delta E_p E_s^* \mathrm{e}^{\mathrm{i}\alpha(\omega_0 t - k_0 x)^2}, \tag{7.7}$$

with $E_{p,s}$ denoting the pump's and seed's amplitude, respectively, N the density variation with respect to the unperturbed background density n_0, α the quadratic chirp, ω_0 and k_0 central laser frequency and wavenumber, respectively and the coupling parameter δ. This is basically the one-dimensional version of our envelope model including chirp (6.4)-(6.6) but with a density dependent coupling parameter δ. We find

$$\delta = 4\frac{Z m_e}{m_i} \frac{\sqrt{\omega_{pe}\omega_0}}{ck_0}, \tag{7.8}$$

with Z being the ion charge state, $m_{e,i}$ the electron and ion mass, respectively, c the vacuum speed of light and ω_{pe} the electron plasma frequency. We note $\omega_{pe} = \sqrt{4\pi e^2 n_0/m_e}$ and thus for a density profile we have a dependency $\delta \propto \tilde{n}^{1/4}$ if $n_0(x) = n_0^0 \tilde{n}(x)$.

We assume large transverse diameters thus at first stick to the one-dimensional case. Both pump and seed laser have a a central wavelength of $\lambda_0 = 1054$ nm and a bandwidth of $\Delta\lambda \approx 6.55$ nm and have a Gaussian profile in longitudinal direction. The seed is bandwidth-limited and thus has a FWHM duration of $\Delta\tau_{\mathrm{seed}} \approx 500$ fs. The seed's peak intensity is $I_0^s = 10^9$ W/cm^2. For the pump intensity, duration and chirp-rate we perform parameter scans, holding the pump energy-per-area Ξ constant at $\Xi \approx 22.55$ kJ/cm^2. We vary the pump duration τ_{pump} between $1 - 6$ ps and thus the peak intensity from $3 \cdot 10^{16} - 5 \cdot 10^{15}$ W/cm^2 in order to hold Ξ constant. Since the pump has the same bandwidth as the seed we have to take into account the chirp-rate α which is calculated via

$$|\alpha| = \frac{\sqrt{\Delta\omega^2 \tau_{\mathrm{pump}}^2 - 64\log(2)^2}}{2\tau_{\mathrm{pump}}^2 \omega_0^2}, \tag{7.9}$$

with the frequency bandwidth $\Delta\omega = 2\pi c\Delta\lambda/\lambda_0^2$. In Fig. 7.5, which shows $\alpha(\tau_{\mathrm{pump}})$, one finds that for longer pump durations one needs lower chirp α. In the following we always talk about pump durations since via Eq. (7.9) we can translate it into the chirp-rate α.
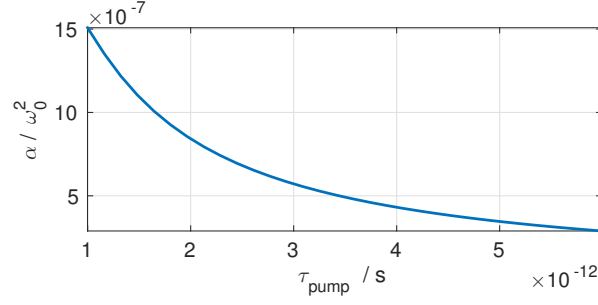
Figure 7.5: Chirp-rate α vs. pump duration τ_{pump} according to Eq. (7.9) for a constant bandwidth of $\Delta\lambda \approx 6.55$ nm around $\lambda_0 = 1054$ nm. Note that for large durations a low chirp-rate is necessary.

For the density we assume a Gaussian slab with a FWHM length of $d \approx 948\lambda_0 \approx 1$ mm. Both the seed and the pump pulse start in a distance of d from the density peak in opposite directions. In its peak the density is $n_0^0 = 0.1n_c \approx 10^{20}$ cm^{-3}. Simulations are performed in a co-moving frame with respect to the seed.
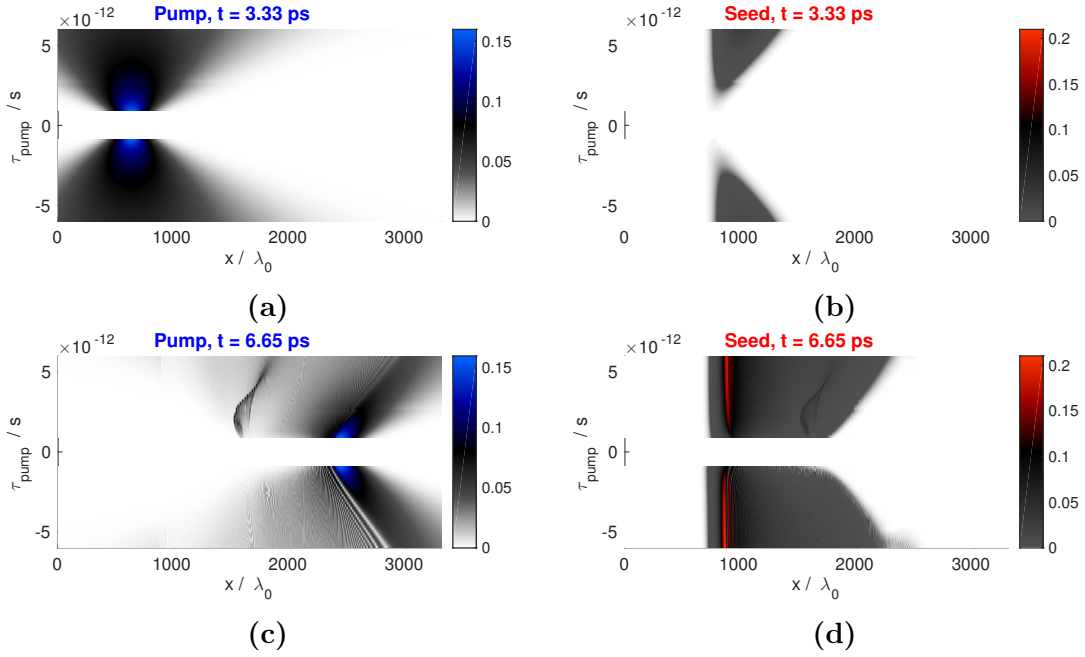
Figure 7.6: Multiple one-dimensional simulation results for parameters as specified in text. Shown are pump $|E_p|$ (left column) and seed $|E_s|$ (right column) pulse at different times. On the x-axis there is space, on the y-axis there is the pump duration resolved, color represents the respective amplitude. The pump always carries the same energy (per area, 1d simulations) but changes its duration and thus the chirp-rate α according to Eq. (7.9) and its peak intensity

Fig. 7.6 shows multiple one-dimensional simulations with parameters as depicted above. Negative pump duration $\tau_{\text{pump}} < 0$ stands for negative sign of the chirp α. Fig. 7.6a shows the pump at the end of the linear stage where no depletion is visible. It has already propagated into the simulation box.
The seed is located at $x = 800\lambda_0$ and stays there since the simulation box moves with its group velocity. Fig. 7.6b shows the seed at the end of the linear stage and the drawn tail is visible.

Fig. 7.6c shows the pump after the interaction. For every duration one observes depletion after the leading intensity front. The lower the maximum amplitude is, the earlier depletion sets in. Additionally, one finds that for negative chirp-rates the oscillations behind the leading front go down close to zero while for positive α it looks more like a steady slope almost without any oscillations.

Fig. 7.6d shows the according seed after the amplification and thus after pump depletion. The same tendency is visible: for negative chirp the oscillations go to zero, for positive chirps one gets one large plateau as a result. One can also see that longer pump pulse durations seem favorable, since the final amplitude of the seed is higher.
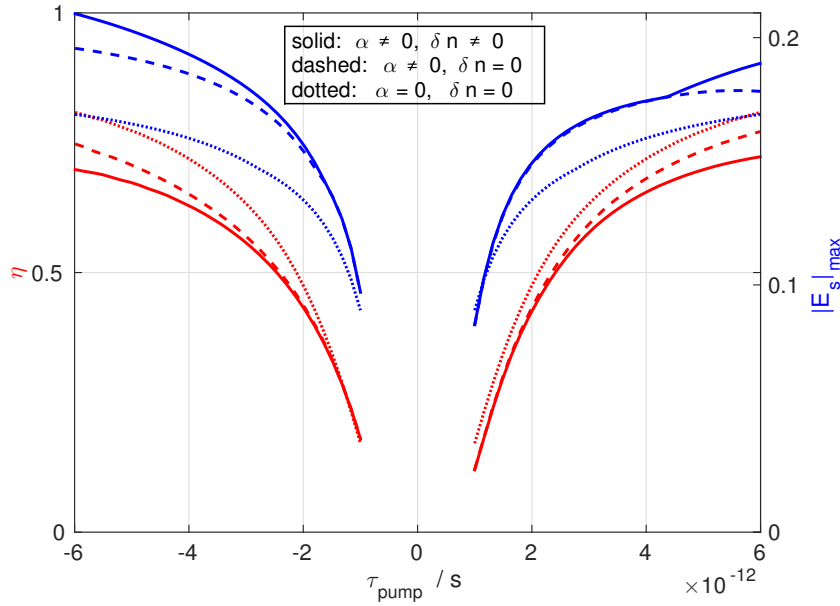
Figure 7.7: Energy transmission efficiency η (red, left-hand y-axis) and maximum peak amplitude (blue, right-hand y-axis), respectively, vs. pump duration. Each for the same radiated pump energy (per area, 1D simulations). Depicted are three different cases: solid lines for parameters as specified above, dashed for a flat density profile at $n_0 = 0.1n_c$ and dotted for neglect of both, the chirp and the density shape.

Fig. 7.7 depicts the efficiency (red) and maximum peak amplitude (blue) after the amplification. The solid line represents the values for parameters as specified above. The dashed line stands for a flat density profile at $n_0 = 0.1n_c$ and in order to obtain the dotted line, we neglected both the density profile and the influence of the chirp ($\alpha = 0$).

One finds that for longer pump durations the energy transmission efficiency as well as the maximum peak amplitude grows (up to $\eta \approx 70\%$, $|E_s|_{\max} \approx 0.21$). As in Fig. 7.6 we spot an asymmetry in the results with respect to the sign of the chirp. For positive sign (upchirp) we see a slightly larger efficiency and lower peak intensity, for negative sign (downchirp) vice versa.

The dotted line is symmetric around zero since here the influence of the chirp is neglected and the results to the left are the same as the ones to the right. When chirp is considered (dashed), we see that we increase the maximum peak intensity and simultaneously decrease the efficiency. When we even respect the density profile we have an increase in this effect: The efficiency is decreased and the maximum amplitude increased further.

However, for negative chirp-rates, we find a lower growth of the sc-SBS plasma mode (not shown) which is appreciated since this is one criterion for the validity of our model.

Fig. 7.8 shows the seed for a pump duration of 6 ps. In Fig. 7.8a the chirp has negative sign, in Fig. 7.8b positive. Shown are again three plots each, dotted with neglect of chirp and density, dashed with neglect of the density profile and solid with all parameters as specified above. For the black dashed line one sees the typical π-pulse-like oscillations often depicted in literature. We see that the chirp highly modulates these oscillations. For downchirp ($\alpha < 0$) we see the oscillations going down to zero, for upchirp ($\alpha > 0$) we see the oscillations vanish and a huge pulse plateau is obtained.

Fig. 7.9 shows the seed after the amplification for different chirp-rates α and is thus analog to Fig. 7.6. Fig. 7.9a is for negative, Fig. 7.9b for positive chirp. This stresses that for downchirp the oscillations behind the leading maximum go further down and for upchirp eventually vanish. This also stresses that for lower chirp rate (longer pump duration) the maximum peak intensity obtained increases.
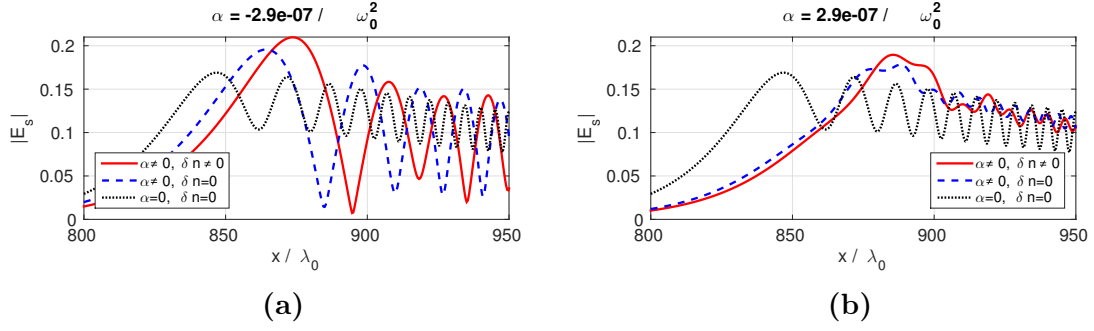
Figure 7.8: Pump duration is 6 ps, the chirp has either negative (a) or positive (b) sign. The black dotted line represents neglect of chirp and the density profile, the dashed blue only neglect of the density profile and the solid red one is obtained via all parameters specified as above.
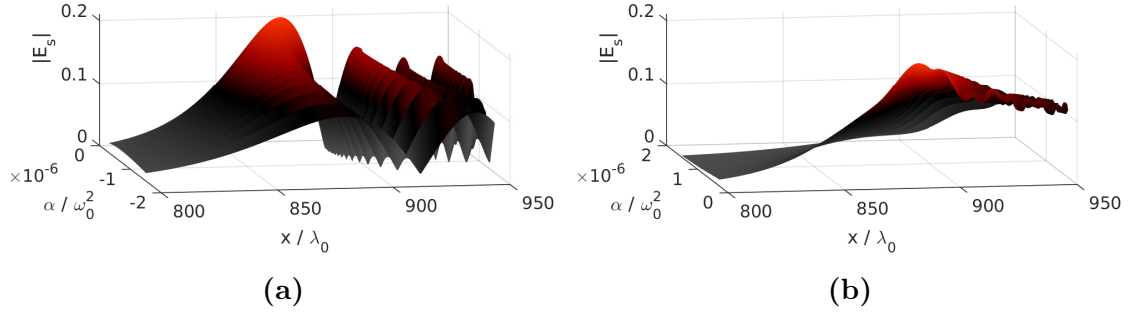

Figure 7.9: Pump duration varies as α does, negative (a) or positive (b) sign. On the x-axis the pulses are spatially resolved.

Considering the actual chirp-rate α and density variation δn we were able to deliver a parameter scan for both efficiency and seed peak amplitude in Fig. 7.7. Subsequently, our results were taken into consideration for the actual experiment.

8 Summary and prospects

In this chapter we summarize the findings of the work at hand. Early ideas of harnessing Brillouin scattering as a potential amplification mechanism date back to the 1980s, however, only the more recent advance in both computer technology and scientific understanding of the process opened up the possibility for further insight.

After summarizing the thesis in Sec. 8.1 we give a short mention to earlier attempts carried out during the past years in Sec. 8.2. Of these attempts, not all were successful, yet relevant enough to be mentioned here, if only as a signpost for coming generations of researchers.

8.1 Summary

The contributions made towards establishing a Brillouin amplification setup as a feasible method for further increase in maximum peak intensity laser generation are crucial, as, among other points, is made evident by the manuscripts submitted to a high impact factor journal.

Having established the physical background including basic analytic models and equations ready for simulations in Chs. 2 and 3, we began by discussing the weakly relativistic kinetic treatment of Brillouin amplification for an arbitrary ion species in homogeneous charge state in Ch. 4. This is a necessity for discussing electron-positron plasmas as here, plasma waves might be heavily damped. This is the first time we present this dispersion relation in writing. The discovery that the fluid model delivers the same results as the kinetic model for Hydrogen is a further highly relevant point that supports several previous findings.

In Ch. 5 we discussed significant observations covering the transition between weak and strong coupling Brillouin amplification. We derived a unified model, valid in both limit regimes and in the intermediate case. Here, we were able to distinguish between three important phenomena: When the interaction starts in strong coupling, the pump will eventually be depleted and thus its amplitude will drop below the threshold for strong coupling. As a consequence, the tail trailing the leading maximum of the seed will experience weakly coupled amplification. Second, typical laser pulses in experiments are Gaussian shaped. Therefore, even if the threshold for strong coupling is surpassed at the pulses peak, this may not be the case for its wings, resulting in a considerable drop in energy transmission

efficiency. Third, an experiment starting in weak coupling will always end in a strong coupling scenario as the seed gets amplified and eventually surpasses the required intensity. We investigated the time necessary for an arbitrary interaction setup to reach strong coupling and explained the characteristic density oscillations.

Hereafter we presented the results regarding the pump pulse chirp in Ch. 6. We found that, other than in weak coupling Brillouin or Raman amplification scenarios, the sign of the chirp plays an important role in strong coupling Brillouin . We then identified the intrinsic chirp in the nonlinear regime of the amplification as responsible for this asymmetry and discussed the influence of the pump chirp on the resulting seed shape and energy. Furthermore, we explained the chirp intrinsic to strong coupling Brillouin amplification by analyzing the homogeneous solution to the density equation. As laser pulses in labs are typically affected by a chirp, this work was also extremely relevant to previous and future experiments.

In Ch. 7 we summarized the simulations and investigations performed for the experiments, i.e. spontaneous Raman backscatter, ionization or collisional absorption and chirp.

The goal of this thesis, as already mentioned in the introduction, is to search for optimal adjustments of laser and plasma settings in the wide parameter-space. In consideration of the full model that combines weak and strong coupling, we made out several possible loss mechanisms that at least partially explain the discrepancy of energy transmission efficiencies predicted by theory and yielded by experiments. These are the influence of real chirp rates including their sign, the possibility of spontaneous Raman backscattering, and collisional damping of laser light. Furthermore, we were able to deepen the general understanding of the amplification process by formulating and analyzing the kinetic dispersion relation, the transition between weak and strong coupling Brillouin, and the influence of chirp.

The contributions made are fundamental, but there is still a long way to go before we will be able to include Brillouin amplification units in labs as a regular component of high intensity laser systems. At this point we would like to point out that, although on the process is theoretically well understood, the experimental setup is tremendously difficult. One needs a majorly ionized and homogeneous plasma of about 1 mm length with a high density on the order of 10^{20} cm^{-3} and two almost perfectly aligned laser pulses. Through meetings with experimental physicists and through experience collected during the work presented in Ch. 7, the author noticed that there is still a variety of different problems theoreticians and experimentalists face in their pursuit of making Brillouin amplification feasible.

The work at hand offers a base upon which further research can build. If both theoreticians and experimentalists work together closely, there is a good chance

that Brillouin amplification will reach a state where it is a feasible, robust and reliable application. This could be realized within the next decades, opening many doors from fundamental research to tabletop laser accelerators for hospitals.

8.2 Other attempts

In the following we list four different attempts from our work on strongly coupled Brillouin amplification, that were either not further investigated or failed to achieve good results, but may still be useful for coming generations.

One important feature of parametric instabilities covers the analytic self-similarity theory. In appendix A.2 we explain in detail how we conducted such an attempt at Brillouin amplification covering weak and strong coupling. However, although qualitatively the results nicely fit the simulated envelopes, our theory failed to give scaling laws predicting the growth of the leading seed spike like former theories did [50, 55, 92].

Another idea to omit both pump pulse absorption by the plasma via inverse bremsstrahlung and the need of a third laser, pre-heating and ionizing the plasma, was to use a neutral gas target and ionize it with a strong seed pulse. As the seed pulse would only ionize the target at its front, there would be almost no room for collisional damping since there are neither free electrons nor ions at the front. However, because this simultaneously reduced the effective plasma length, we were not able to observe sufficient amplification in order to recommend this scheme.

The taking into account of the kinetic scattering mechanism of superradiant amplification mentioned in Sec. 2.3.2 and mainly investigated by Dreher *et al.* [100] could give further interesting leads. Neither the transition from weakly or strongly coupled Brillouin into superradiant amplification, nor wave breaking for the plasma quasi-mode responsible for strong coupling Brillouin has been investigated so far.

Further research on self-focusing, seed pulse broadening and curvature in two dimensions, filamentation, and superluminal motion were made throughout recent years and, for example, investigated in the author's master thesis. It may be worthwhile to pursue these subjects in further detail.

Bibliography

[1] A. Einstein, Annalen der Physik **322**, 132 (1905).

[2] A. Einstein, Annalen der Physik **322**, 891 (1905).

[3] T. H. Maiman, in *Press Conference at the Hotel Delmonico*, 1960.

[4] A. Schawlow and C. Townes, (1960), US Patent 2,929,922.

[5] D. Strickland and G. Mourou, Opt. Commun. **56**, 219 (1985).

[6] A. Dubietis, G. Jonuoauskas, and A. Piskarskas, Opt. Comm. **88**, 437 (1992).

[7] http://www.popsci.com/researchers-japan-fired-worlds-most-powerful laser, retrieved on 25th Oct 2016.

[8] https://www.llnl.gov/news/lawrence-livermore-deploys-worldarrays, retrieved on 21st Oct 2016.

[9] www.iea.org, Key world energy statistics 2015, retrieved on 28th Oct 2016, 2015, pp. 8, 37.

[10] http://www.eli beams.eu/science/lasers/, retrieved on 28th Oct 2016.

[11] A. Caruso and R. Gratton, Plasma Phys. **11**, 839 (1969).

[12] A. Pukhov and J. Meyer-ter Vehn, Applied Physics B **74**, 355 (2002).

[13] A. Pukhov and J. Meyer-ter Vehn, Phys. Rev. Lett. **76**, 3975 (1996).

[14] A. Pukhov and J. Meyer-ter Vehn, Phys. Rev. Lett. **79**, 2686 (1997).

[15] W. P. Leemans, A. J. Gonsalves, H.-S. Mao, K. Nakamura, C. Benedetti, C. B. Schroeder, C. Tóth, J. Daniels, D. E. Mittelberger, S. S. Bulanov, J.-L. Vay, C. G. R. Geddes, and E. Esarey, Phys. Rev. Lett. **113**, 245002 (2014).

[16] M. Litos, E. Adli, J. M. Allen, W. An, C. I. Clarke, S. Corde, C. E. Clayton, J. Frederico, S. J. Gessner, S. Z. Green, M. J. Hogan, C. Joshi, W. Lu, K. A. Marsh, W. B. Mori, M. Schmeltz, N. Vafaei-Najafabadi, and V. Yakimenko, Plasma Phys. Cont. Fusion **58**, 034017 (2016).

[17] B. Hegelich, D. Jung, B. Albright, M. Cheung, B. Dromey, D. Gautier, C. Hamilton, S. Letzring, R. Munchhausen, S. Palaniyappan, R. Shah, H.-C. Wu, L. Yin, and J. Fernandez, ArXiv e-prints , arXiv:1310.8650 (2013).

[18] A. Novo, M. Kaluza, R. Fonseca, and L. Silva, Sci. Rep. **6**, 29402 (2016).

[19] M. Nicolai, A. Sävert, M. Reuter, M. Schnell, J. Polz, O. Jäckel, L. Karsch, M. Schürer, M. Oppelt, J. Pawelke, and M. C. Kaluza, Appl. Phys. B **116**, 643 (2014).

[20] https://home.cern/about/opinion/2015/11/new-energy-frontier-heavy ions, A new energy frontier for heavy ions, retrieved on 3rd Nov 2016, 2015.

[21] R. Lichters, J. Meyer-ter Vehn, and A. Pukhov, Phys. Plasmas **3**, 3425 (1996).

[22] L. Ji, B. Shen, X. Zhang, W. Wang, Y. Yu, X. Wang, L. Yi, and Y. Shi, Plasma Sci. Tech. **14**, 859 (2012).

[23] Z.-Y. Chen, Appl. Phys. Lett. **102** (2013).

[24] Z.-Y. Chen and A. Pukhov, Phys. Plasmas **22** (2015).

[25] B. C. Stuart, M. D. Feit, S. Herman, A. M. Rubenchik, B. W. Shore, and M. D. Perry, J. Opt. Soc. Am. B **13**, 459 (1996).

[26] O. Uteza, B. Bussiere, F. Canova, J.-P. Chambaret, P. Delaporte, T. Itina, and M. Sentis, Appl. Surf. Sci. **254**, 799 (2007).

[27] M. Maier, W. Kaiser, and J. A. Giordmaine, Phys. Rev. Lett. **17**, 1275 (1966).

[28] R. D. Milroy, C. E. Capjack, and C. R. James, Phys. Fluids **22**, 1922 (1979).

[29] B. I. Cohen and C. E. Max, Phys. Fluids **22**, 1115 (1979).

[30] C. E. Capjack, C. R. James, and J. N. McMullin, J. App. Phys. **53**, 4046 (1982).

[31] S. Hüller, P. Mulser, and A. M. Rubenchik, Phys. Fluids B **3**, 3339 (1991).

[32] V. M. Malkin, G. Shvets, and N. J. Fisch, Phys. Rev. Lett. **82**, 4448 (1999).

[33] N. J. Fisch and V. M. Malkin, Phys. Plasmas **10**, 2056 (2003).

[34] G. Mourou, N. Fisch, V. Malkin, Z. Toroker, E. Khazanov, A. Sergeev, T. Tajima, and B. L. Garrec, Opt. Comm. **285**, 720 (2012).

[35] J. Ren, W. Cheng, S. Li, and S. Suckewer, Nature Phys. **3**, 732 (2007).

[36] G. Mourou and T. Tajima, Science **331**, 41 (2011).

[37] P. Gibbon, *Short Pulse Laser Iinteractions with Mafter*, Imperial College Press, 2007.

[38] Z. Toroker, V. M. Malkin, A. A. Balakin, G. M. Fraiman, and N. J. Fisch, Phys. Plasmas **19**, 083110 (2012).

[39] P. Alves, R. Trines, K. Humphrey, R. Bingham, A. Cairns, F. Fiuza, R. Fonseca, L. Silva, and P. Norreys, ArXiv e-prints , arXiv:1311.2034 (2013).

[40] D. W. Forslund, J. M. Kindel, and E. L. Lindman, Phys. Fluids **18**, 1002 (1975).

[41] W. L. Kruer, *Physics Of Laser Plasma Interactions*, Westview Press, 2003.

[42] V. M. Malkin, G. Shvets, and N. J. Fisch, Phys. Plasmas **7**, 2232 (2000).

[43] V. M. Malkin and N. J. Fisch, Phys. Plasmas **12**, 044507 (2005).

[44] P. Mounaix, D. Pesme, W. Rozmus, and M. Casanova, Phys. Fluids B **5**, 3304 (1993).

[45] G. Shvets, J. S. Wurtele, and B. A. Shadwick, Phys. Plasmas **4**, 1872 (1997).

[46] W. Cheng, Y. Avitzour, Y. Ping, S. Suckewer, N. J. Fisch, M. S. Hur, and J. S. Wurtele, Phys. Rev. Lett. **94**, 045003 (2005).

[47] G. Vieux, A. Lyachev, X. Yang, B. Ersfeld, J. P. Farmer, E. Brunetti, R. C. Issac, G. Raj, G. H. Welsh, S. M. Wiggins, and D. A. Jaroszynski, New J. Phys. **13**, 063042 (2011).

[48] R. M. G. M. Trines, F. Fiúza, R. Bingham, R. A. Fonseca, L. O. Silva, R. A. Cairns, and P. A. Norreys, Phys. Rev. Lett. **107**, 105002 (2011).

[49] B. Landgraf, B. Aurand, G. Lehmann, T. Gangolf, M. Schnell, T. Kühl, and C. Spielmann, N. J. Phys. **18**, 073048 (2016).

[50] G. Lehmann and K. H. Spatschek, Phys. Plasmas **20**, 073112 (2013).

[51] M. Shoucri, J.-P. Matte, and F. Vidal, Phys. Plasmas **22**, 053101 (2015).

[52] N. A. Yampolsky, N. J. Fisch, V. M. Malkin, E. J. Valeo, R. Lindberg, J. Wurtele, J. Ren, S. Li, A. Morozov, and S. Suckewer, Phys. Plasmas **15**, 113104 (2008).

[53] N. A. Yampolsky and N. J. Fisch, Phys. Plasmas **18**, 056711 (2011).

[54] P. N. Guzdar, C. S. Liu, and R. H. Lehmberg, Phys. Plasmas **3**, 3414 (1996).

[55] A. A. Andreev, C. Riconda, V. T. Tikhonchuk, and S. Weber, Phys. Plasmas **13**, 053110 (2006).

[56] C. Riconda, S. Weber, L. Lancia, J.-R. Marquès, G. A. Mourou, and J. Fuchs, Phys. Plasmas **20**, 083115 (2013).

[57] C. Riconda, S. Weber, L. Lancia, J.-R. Marquès, G. Mourou, and J. Fuchs, Plasma Phys. Cont. Fusion **57**, 014002 (2015).

[58] F. Schluck, G. Lehmann, C. Müller, and K. H. Spatschek, Phys. Plasmas **23** (2016).

[59] B. Ersfeld and D. A. Jaroszynski, Phys. Rev. Lett. **95**, 165002 (2005).

[60] R. Nuter and V. Tikhonchuk, Phys. Rev. E **87**, 043109 (2013).

[61] G. Lehmann and K. H. Spatschek, Phys. Plasmas **22**, 043105 (2015).

[62] F. Schluck, G. Lehmann, and K. H. Spatschek, Phys. Plasmas **22**, 093104 (2015).

[63] S. Weber, C. Riconda, L. Lancia, J.-R. Marquès, G. A. Mourou, and J. Fuchs, Phys. Rev. Lett. **111**, 055004 (2013).

[64] R. M. G. M. Trines, E. P. Alves, K. A. Humphrey, R. Bingham, R. A. Cairns, F. Fiuza, R. A. Fonseca, L. O. Silva, and P. A. Norreys, ArXiv e-prints , arXiv:1406.5424 (2014).

[65] A. Frank, J. Fuchs, L. Lancia, G. Lehmann, J.-R. Marquès, G. Mourou, C. Riconda, K. Spatschek, T. Toncian, L. Vassura, and S. Weber, EPJ Special Topics **223**, 1153 (2014).

[66] D. Turnbull, S. Li, A. Morozov, and S. Suckewer, Phys. Plasmas **19**, 083109 (2012).

[67] A. Pukhov, Rep. Prog. Phys. **66**, 47 (2003).

[68] G. A. Mourou, T. Tajima, and S. V. Bulanov, Rev. Mod. Phys. **78**, 309 (2006).

[69] G. Lehmann, F. Schluck, and K. H. Spatschek, Phys. Plasmas **19**, 093120 (2012).

[70] P. K. Shukla and L. Stenflo, Phys. Plasmas **7**, 2728 (2000).

[71] V. Muñoz and L. Gomberoff, Phys. Plasmas **9**, 2534 (2002).

[72] M. R. Edwards, N. J. Fisch, and J. M. Mikhailova, Phys. Rev. Lett. **116**, 015004 (2016).

[73] F. Schluck, G. Lehmann, and K. H. Spatschek, in preparation (2016).

[74] L. Lancia, J.-R. Marquès, M. Nakatsutsumi, C. Riconda, S. Weber, S. Hüller, A. Mančić, P. Antici, V. T. Tikhonchuk, A. Héron, P. Audebert, and J. Fuchs, Phys. Rev. Lett. **104**, 025001 (2010).

[75] L. Lancia, A. Giribono, L. Vassura, M. Chiaramello, C. Riconda, S. Weber, A. Castan, A. Chatelain, A. Frank, T. Gangolf, M. N. Quinn, J. Fuchs, and J.-R. Marquès, Phys. Rev. Lett. **116**, 075001 (2016).

[76] E. Guillaume, K. Humphrey, H. Nakamura, R. M. G. M. Trines, R. Heathcote, M. Galimberti, Y. Amano, D. Doria, G. Hicks, E. Higson, S. Kar, G. Sarri, M. Skramic, J. Swain, K. Tang, J. Weston, P. Zak, E. P. Alves, R. A. Fonseca, F. Fiùza, H. Habara, K. A. Tanaka, R. Bingham, M. Borghesi, Z. Najmudin, L. O. Silva, and P. A. Norreys, H. Pow. Laser Sci. Eng. **2**, e33 (2014).

[77] M. Chiaramello, C. Riconda, F. Amiranoff, J. Fuchs, M. Grech, L. Lancia, J.-R. Marquès, T. Vinci, and S. Weber, Phys. Plasmas **23** (2016).

[78] S. Eliezer, *The Interaction of High-Power Lasers with Plasmas*, Institute of Physics Publishing Bristol and Philadelphia, 2002.

[79] J. Diels and W. Rudolph, *Ultrashort Laser Pulse phenomena*, New York Academic Press, 2006.

[80] S. Pfalzner, *An Introduction to Inertial Confinement Fusion*, Taylor & Francis, 2006.

[81] K. H. Spatschek, *High Temperature Plasmas*, Wiley-VCH, 2012.

[82] P. McKenna, D. Neely, R. Bingham, and D. Jaroszynski, *Laser-Plasma Interactions and Applications*, Springer, 2013.

[83] S. Balay, W. D. Gropp, L. C. McInnes, and B. F. Smith, p. 163 (1997).

[84] S. Balay, S. Abhyankar, M. F. Adams, J. Brown, P. Brune, K. Buschelman, L. Dalcin, V. Eijkhout, W. D. Gropp, D. Kaushik, M. G. Knepley, L. C. McInnes, K. Rupp, B. F. Smith, S. Zampini, H. Zhang, and H. Zhang, (2016).

[85] C. S. Brady and T. D. Arber, Plasma Phys. Cont. Fusion **53**, 015001 (2011).

[86] C. S. Brady, A. Lawrence-Douglas, and T. D. Arber, Phys. Plasmas **19** (2012).

[87] L. Landau and E. Lifshitz, *Quantum Mechanics*, Pergamon Press, 1965.

[88] L. Spitzer, *Physics of fully ionized gases*, Interscience Publishers, 1962.

[89] D. L. Book, NRL plasma formulary (1983).

[90] R. Grella, J. Optics **13**, 367 (1982).

[91] G. Shvets, N. J. Fisch, A. Pukhov, and J. Meyer-ter Vehn, Phys. Rev. Lett. **81**, 4879 (1998).

[92] G. Lehmann, K. H. Spatschek, and G. Sewell, Phys. Rev. E **87**, 063107 (2013).

[93] G. Sarri, K. Poder, J. Cole, W. Schumaker, A. Di Piazza, B. Reville, T. Dzelzainis, D. Doria, L. Gizzi, G. Grittani, S. Kar, C. Keitel, K. Krushelnick, S. Kuschel, S. Mangles, Z. Najmudin, N. Shukla, L. Silva, D. Symes, A. Thomas, M. Vargas, J. Vieira, and M. Zepf, Nature Comm. **6**, 6747 (2015).

[94] P. H. Bucksbaum, A. Zavriyev, H. G. Muller, and D. W. Schumacher, Phys. Rev. Lett. **64**, 1883 (1990).

[95] J. H. Posthumus, Rep. Prog. Phys. **67**, 623 (2004).

[96] J. Denavit and D. W. Phillion, Phys. Plasmas **1**, 1971 (1994).

[97] V. Malka, J. Faure, and F. Amiranoff, Phys. Plasmas **8**, 3467 (2001).

[98] G. Zimmerman, D. Kershaw, D. Bailey, and J. Harte, (1977), LASNEX code for inertial confinement fusion.

[99] R. Ramis, R. Schmalz, and J. Meyer-Ter-Vehn, Comp. Phys. Comm. **49**, 475 (1988).

[100] M. Dreher, E. Takahashi, J. Meyer-ter Vehn, and K.-J. Witte, Phys. Rev. Lett. **93**, 095001 (2004).

A

A.1 Derivation of a weakly relativistic kinetic dispersion relation

We present the full derivation of Eq. (4.12).

Similar to [71] we start with Maxwell's equations and the Vlasov equation

$$\left(\nabla^2 - \frac{1}{c^2}\frac{\partial^2}{\partial t^2}\right)\mathbf{A} = -\frac{4\pi}{c}\mathbf{j}_\perp, \tag{A.1}$$

$$\nabla^2\phi = -4\pi e\left(n_i - n_e\right), \tag{A.2}$$

$$0 = \frac{\partial}{\partial t}f_k + \mathbf{v}\cdot\nabla_\mathbf{r}f_k + q_k\left(\mathbf{E} + \frac{1}{c}\mathbf{v}\times\mathbf{B}\right)\cdot\nabla_\mathbf{p}f_k, \tag{A.3}$$

with the vector potential $\mathbf{A}$, the electrostatic potential ϕ, the distribution function f_k, speed of light c, perpendicular current $\mathbf{j}_\perp$, elementary charge e and particle charge q_k, density n_k, velocity $\mathbf{v}$, electric field $\mathbf{E}$ and magnetic field $\mathbf{B}$. The index k denotes the species $k = e, i$, hence electron or ion, and $\mathbf{B} = \nabla\times\mathbf{A}$.

We assume the distribution function f_k only depending on the laser propagation direction z and find

$$f_k\left(z, \mathbf{p}, t\right) = n_{k0}g_k\left(z, p_z, t\right)\delta\left(p_x + \frac{q_k A_x}{c}\right)\delta\left(p_y + \frac{q_k A_y}{c}\right), \tag{A.4}$$

where δ denotes the δ distribution. We assume $n_{i0} = n_{e0} \equiv n_0$ and write

$$n_k\left(z, t\right) = n_0\int_{-\infty}^{+\infty}dp_z\left[g_k\left(z, p_z, t\right)\right], \tag{A.5}$$

$$\mathbf{j}_\perp\left(z, t\right) = -\frac{e^2 n_0}{c}\mathbf{A}\left(z, t\right)\int_{-\infty}^{+\infty}dp_z\left[\frac{g_i}{m_i\gamma_i} + \frac{g_e}{m_e\gamma_e}\right],$$

$$= -\frac{e^2 n_0}{m_e c}\mathbf{A}\left(z, t\right)\int_{-\infty}^{+\infty}dp_z\left[\beta\frac{g_i}{\gamma_i} + \frac{g_e}{\gamma_e}\right], \tag{A.6}$$

where $\beta = m_e/m_i$ denotes the mass ratio. The Lorentz factor γ_k is given as

$$\gamma_e = \sqrt{1 + \left(\frac{p_z}{m_e c}\right)^2 + \left(\frac{e\mathbf{A}\left(z, t\right)}{m_e c^2}\right)^2}, \tag{A.7}$$

$$\gamma_i = \sqrt{1 + \beta^2\left(\frac{p_z}{m_e c}\right)^2 + \beta^2\left(\frac{e\mathbf{A}\left(z, t\right)}{m_e c^2}\right)^2}, \tag{A.8}$$

A.1. DERIVATION OF A WEAKLY RELATIVISTIC KINETIC DISPERSION RELATION

Inserting Eqs. (A.4)-(A.8) into the initial system (A.1)-(A.3) we find

$$\left(\frac{\partial^2}{\partial z^2} - \frac{1}{c^2}\frac{\partial^2}{\partial t^2}\right)\mathbf{A} = \frac{\omega_{pe}^2}{c^2}\mathbf{A}\int_{-\infty}^{+\infty} dp_z \left[\beta\frac{g_i}{\gamma_i} + \frac{g_e}{\gamma_e}\right], \tag{A.9}$$

$$\frac{\partial^2}{\partial z^2}\phi = -4\pi e n_0 \int_{-\infty}^{+\infty} dp_z \left[g_i - g_e\right], \tag{A.10}$$

$$0 = \frac{\partial}{\partial t}g_k + v_z\frac{\partial}{\partial z}g_k + \left[-q_k\frac{\partial}{\partial z}\phi - \frac{m_k}{2}\left(\frac{e}{m_k c}\right)^2\frac{1}{\gamma_k}\frac{\partial}{\partial z}\mathbf{A}^2\right]\frac{\partial}{\partial p_z}g_k. \tag{A.11}$$

Perturbing the system (A.9)-(A.11) via

$$\phi = \phi_0 + \epsilon\phi_1, \quad \mathbf{A} = \mathbf{A}_0 + \epsilon\mathbf{A}_1, \quad g_k = g_{k0} + \epsilon g_{k1},$$

$$\phi_0 = 0, \quad \mathbf{A}_0 = A_{0\perp} = A_{0x} + \mathrm{i}A_{0y} = A\exp\left(\mathrm{i}(k_0 z - \omega_0 t)\right), A \in \mathfrak{R},$$

the 0th order terms deliver

$$\omega_0^2 = c^2 k_0^2 + \omega_{pe}^2 \int_{-\infty}^{+\infty} dp_z \left[\beta\frac{g_{i0}}{\gamma_{i0}} + \frac{g_{e0}}{\gamma_{e0}}\right]. \tag{A.12}$$

introducing $a = eA_\perp/mc^2$, we find via Taylor expansion

$$\frac{1}{\gamma_k} \simeq \frac{1}{\gamma_{k0}} - \left(\frac{m_e}{m_k}\right)^3\frac{a_{0\perp}a_1}{\gamma_{k0}^3}\epsilon + \mathcal{O}\left(\epsilon^2\right). \tag{A.13}$$

With Eq. (A.13) we rewrite the system (A.9)-(A.11), selecting only contributions proportional to ϵ and $\partial|a_0|^2/\partial z = 0$,

$$\frac{c^2}{\omega_{pe}^2}\left(\frac{\partial^2}{\partial z^2} - \frac{1}{c^2}\frac{\partial^2}{\partial t^2}\right)a_1 =$$

$$\int_{-\infty}^{+\infty} dp_z \left[a_0\left(\beta\frac{g_{i1}}{\gamma_{i0}} + \frac{g_{e1}}{\gamma_{e0}}\right) + a_1\left(\beta\frac{g_{i0}}{\gamma_{i0}} + \frac{g_{e0}}{\gamma_{e0}}\right) - a_0\left(a_0 a_1^* + a_0^* a_1\right)\left(\frac{\beta^3}{2}\frac{g_{i0}}{\gamma_{i0}^3} + \frac{1}{2}\frac{g_{e0}}{\gamma_{e0}^3}\right)\right], \tag{A.14}$$

$$\frac{\partial^2}{\partial z^2}\phi_1 = -4\pi e n_0 \int_{-\infty}^{+\infty} dp_z \left[g_{i1} - g_{e1}\right], \tag{A.15}$$

$$0 = \left(\frac{\partial}{\partial t} + v_z\frac{\partial}{\partial z}\right)g_{e1} + \left(e\frac{\partial}{\partial z}\phi_1 - \frac{m_e c^2}{2\gamma_{e0}}\frac{\partial\left(a_0 a_1^* + a_0^* a_1\right)}{\partial z}\right)\frac{\partial g_{e0}}{\partial z}, \tag{A.16}$$

$$0 = \left(\frac{\partial}{\partial t} + v_z\frac{\partial}{\partial z}\right)g_{i1} - \left(e\frac{\partial}{\partial z}\phi_1 + \beta\frac{m_e c^2}{2\gamma_{i0}}\frac{\partial\left(a_0 a_1^* + a_0^* a_1\right)}{\partial z}\right)\frac{\partial g_{e0}}{\partial z}, \tag{A.17}$$

since $q_e = -e$ and $q_i = e$. We make the ansatz

$$\phi_1 = \tilde{\phi}\exp\left(\mathrm{i}(kz - \omega t)\right) + \tilde{\phi}^*\exp\left(-\mathrm{i}(k^*z - \omega^*t)\right),$$
$$g_{k1} = \tilde{g}_k\exp\left(\mathrm{i}(kz - \omega t)\right) + \tilde{g}_k^*\exp\left(\mathrm{i}(k^*z - \omega^*t)\right),$$
$$a_{1\perp} = a_+\exp\left(\mathrm{i}(k_+z - \omega_+t)\right) + a_-\exp\left(\mathrm{i}(k_-z - \omega_-t)\right),$$

with $k_+ = k_0 + k$, $k_- = k_0 - k^*$. With Eqs. (A.16) and (A.17) we construct, selecting resonant terms,

$$\beta\frac{\tilde{g}_i}{\gamma_{i0}} + \frac{\tilde{g}_e}{\gamma_{e0}} = \frac{ek\tilde{\phi}\left(\beta\frac{\partial g_{i0}/\partial p_z}{\gamma_{i0}} - \frac{\partial g_{e0}/\partial p_z}{\gamma_{e0}}\right) + \frac{m_ec^2}{2}ka\left(a_-^* + a_+\right)\left(\beta^2\frac{\partial g_{i0}/\partial p_z}{\gamma_{i0}^2} + \frac{\partial g_{e0}/\partial p_z}{\gamma_{e0}^2}\right)}{-\omega + v_zk},$$
$$(A.18)$$

$$\tilde{g}_i - \tilde{g}_e = \frac{ek\tilde{\phi}\left(\partial g_{i0}/\partial p_z + \partial g_{e0}/\partial p_z\right) + \frac{m_ec^2}{2}ka\left(a_-^* + a_+\right)\left(\beta\frac{\partial g_{i0}/\partial p_z}{\gamma_{i0}} - \frac{\partial g_{e0}/\partial p_z}{\gamma_{e0}}\right)}{-\omega + v_zk},$$
$$(A.19)$$

as well as the other resonant terms from Eqs. (A.15) and (A.14)

$$\omega_{pe}^2\left(\omega_+^2 - c^2k_+^2\right)a_+ =$$
$$\int_{-\infty}^{+\infty}dp_z\left[-\frac{a}{2}\left(aa_-^* + aa_+\right)\left(\beta^3\frac{g_{i0}}{\gamma_{i0}^3} + \frac{g_{e0}}{\gamma_{e0}^3}\right) + a\left(\beta\frac{\tilde{g}_i}{\gamma_{i0}} + \frac{\tilde{g}_e}{\gamma_{e0}}\right) + a_+\left(\beta\frac{g_{i0}}{\gamma_{i0}} + \frac{g_{e0}}{\gamma_{e0}}\right)\right],$$
$$(A.20)$$

$$\omega_{pe}^2\left(\omega_-^2 - c^2k_-^2\right)a_- =$$
$$\int_{-\infty}^{+\infty}dp_z\left[-\frac{a}{2}\left(aa_- + aa_+^*\right)\left(\beta^3\frac{g_{i0}}{\gamma_{i0}^3} + \frac{g_{e0}}{\gamma_{e0}^3}\right) + a\left(\beta\frac{\tilde{g}_i}{\gamma_{i0}} + \frac{\tilde{g}_e}{\gamma_{e0}}\right) + a_-\left(\beta\frac{g_{i0}}{\gamma_{i0}} + \frac{g_{e0}}{\gamma_{e0}}\right)\right],$$
$$(A.21)$$

$$-k^2\tilde{\phi} = -4\pi en_0\int_{-\infty}^{+\infty}dp_z\left[\tilde{g}_i - \tilde{g}_e\right].$$
$$(A.22)$$

We introduce the notation

$$I_n = \beta^{n-1}I_{in} + I_{en},$$
$$I_{kn} = \int_{-\infty}^{+\infty}dp_z\left[\frac{1}{\gamma_{k0}^{n-1}}\frac{\partial g_{k0}/\partial p_z}{v_zk - \omega}\right],\quad n = 1, 2, 3,$$
$$I_{k4} = \int_{-\infty}^{+\infty}dp_z\left[\frac{g_{k0}}{\gamma_{k0}^3}\right],$$
$$D_+ = -\omega_+^2 + c^2k_+^2 + \omega_{pe}^2\int_{-\infty}^{+\infty}dp_z\left[\frac{\beta}{\gamma_{i0}}g_{i0} + \frac{1}{\gamma_{e0}}g_{e0}\right],$$
$$D_- = -\omega_-^{*\,2} + c^2k_-^{*\,2} + \omega_{pe}^2\int_{-\infty}^{+\infty}dp_z\left[\frac{\beta}{\gamma_{i0}}g_{i0} + \frac{1}{\gamma_{e0}}g_{e0}\right],$$
$$F = \frac{4\pi e^2n_0I_2^2}{k - 4\pi e^2n_0I_1}.$$

Integrating Eqs. (A.18) and (A.19) over longitudinal momentum allows replacement
of the according integrals in Eqs. (A.20)-(A.22) and elimination of $\tilde{\phi}$, hence finding

$$a_+ = \frac{\omega_{pe}^2 a^2}{2} \frac{m_e c^2 k \left(a_-^* + a_+\right)(F + I_3) - a_-^* I_4}{-D_+ + \omega_{pe}^2 a^2 I_4/2}, \tag{A.23}$$

$$a_-^* = \frac{\omega_{pe}^2 a^2}{2} \frac{m_e c^2 k \left(a_-^* + a_+\right)(F + I_3) - a_+ I_4}{-D_- + \omega_{pe}^2 a^2 I_4/2}. \tag{A.24}$$

Solving the linear set of Eqs. (A.23)-(A.24) gives us the weakly relativistic disper-
sion relation for arbitrary ion species with charge state $Z = 1$

$$D_+ D_- = \frac{\omega_{pe}^2 a^2}{4} \left(D_+ + D_-\right) \left[I_4 - m_e c^2 k \left(F + I_3\right)\right]. \tag{A.25}$$

A.2 Self-similar solution in transition from weak to strong coupling

In this appendix we derive a self-similar solution for both weak and strong coupling Brillouin amplification, covering the transition regime.

One differentiates between two different behaviors depending on the pump strength, the so-called weak and strong coupling regimes. These two domains differ fundamentally in both linear and non-linear stage of amplification in terms of growth rate and spectral broadening. Especially the transition regime deserves special interest as it was introduced and investigated in Ch. 5.

Starting from Ampere's and Faraday's laws in combination with continuity and momentum balance we can derive the so-called $\delta N\mathbf{A}$-model consisting of

$$\frac{\partial^2 A}{\partial t^2} = \frac{\partial^2 A}{\partial x^2} - (1 + \delta N)\, A, \tag{A.26}$$

$$\frac{\partial^2 \delta N}{\partial t^2} = c_s^2 \frac{\partial^2 \delta N}{\partial x^2} + \epsilon \frac{\partial^2 |A|^2}{\partial x^2}, \tag{A.27}$$

the same as Eqs. (3.4)-(3.5), with A being the vector potential, δN the change from the background density, $c_s \propto \sqrt{T_e}$ the ion speed of sound proportional to the square root of the electron temperature and $\epsilon = m_e/m_i$ the electron to ion mass ratio, while $[t]$ is the chosen time unit. After application of the slowly varying envelope approximation we can describe the two laser fields plus density wave in a much simpler model. From Eqs. (A.26) and (A.27) we can derive the three wave interaction model

$$\left(\frac{\partial}{\partial t} + \frac{\partial}{\partial x}\right) E_p = -\mathrm{i} N E_s, \tag{A.28}$$

$$\left(\frac{\partial}{\partial t} - \frac{\partial}{\partial x}\right) E_s = -\mathrm{i} N^* E_p, \tag{A.29}$$

$$\left(\frac{\partial^2}{\partial t^2} - 2\mathrm{i}\tilde{\omega}_N \frac{\partial}{\partial t} - 2\mathrm{i}\tilde{c}_s\tilde{\omega}_N \frac{\partial}{\partial x} - \tilde{c}_s^{\,2}\frac{\partial^2}{\partial x^2}\right) N = -\nu E_s^* E_p, \tag{A.30}$$

with $E_{p,s}$ being the normalized electric field and N the change from the background density (all complex envelopes). $\tilde{\omega}_N = (\omega_p - \omega_s)\,[t]$ is the frequency mismatch between pump and seed, $\tilde{c}_s = c_s/v_g$ the ion speed of sound normalized to pump's group velocity and $\nu = Z m_e c k_N^2 \omega_{pe}\,[t]^2 \sqrt{\omega_{pe}/\omega_p}/\,(2m_i k_0)$. See the model (3.12)-(3.14) for comparison.

Our goal is to derive a self-similar solution analog to [55, 50, 92, 62], but our solution should cover the transition regime from weakly to strongly coupled stimulated Brillouin scattering. From previous investigations we know that the

A.2. SELF-SIMILAR SOLUTION IN TRANSITION FROM WEAK TO STRONG COUPLING

$\partial^2/\partial x^2$ term in Eq. (A.30) can be neglected as it has no influence. Next we transform into the co-moving frame of the density wave via introduction of the variables $\zeta = x - \tilde{c}_s t$, $\tau' = -x$ and end up with the system

$$\left[(1 - \tilde{c}_s) \frac{\partial}{\partial \zeta} - \frac{\partial}{\partial \tau'} \right] E_p = -\mathrm{i}N E_s, \tag{A.31}$$

$$\left[-(1 + \tilde{c}_s) \frac{\partial}{\partial \zeta} + \frac{\partial}{\partial \tau'} \right] E_s = -\mathrm{i}N^* E_p, \tag{A.32}$$

$$\left[\tilde{c}_s^{\,2} \frac{\partial^2}{\partial \zeta^2} + 2\mathrm{i}\tilde{\omega}_N \tilde{c}_s \frac{\partial}{\partial \tau'} \right] N = -\nu E_s^* E_p. \tag{A.33}$$

We remark that we *have* to choose this transformation. Else, we end up with second and first order derivatives with respect to the same variable in the density equation. These derivatives would, later on, contradict the self-similarity ansatz. In the transformed equations (A.31)-(A.33) we neglect the τ' derivatives with respect to the ζ derivatives as the amplification length is much larger than the pulse durations. Now we postulate the self-similarity ansatz $\xi = \zeta^\alpha \tau'^\beta$, $\tau = \tau'$ and find for the derivatives

$$\frac{\partial}{\partial \tau'} = \frac{\partial}{\partial \tau} + \beta \zeta^\alpha \tau^{\beta-1} \frac{\partial}{\partial \xi}, \quad \frac{\partial}{\partial \zeta} = \alpha \zeta^{\alpha-1} \tau^\beta \frac{\partial}{\partial \xi},$$

$$\frac{\partial^2}{\partial \zeta^2} = \alpha(\alpha-1) \zeta^{\alpha-2} \tau^\beta \frac{\partial}{\partial \xi} + \alpha^2 \zeta^{2\alpha-2} \tau^{2\beta} \frac{\partial^2}{\partial \xi^2}.$$

With these rules we find the set of Eqs.

$$(1 - \tilde{c}_s) \alpha \xi^{1-1/\alpha} \tau^{\beta/\alpha} \frac{\partial}{\partial \xi} E_p = -\mathrm{i}N E_s, \tag{A.34}$$

$$-(1 + \tilde{c}_s) \alpha \xi^{1-1/\alpha} \tau^{\beta/\alpha} \frac{\partial}{\partial \xi} E_s = -\mathrm{i}N^* E_p, \tag{A.35}$$

$$\left[\alpha(\alpha-1) \tilde{c}_s^{\,2} \xi^{1-2/\alpha} \tau^{2\beta/\alpha} \frac{\partial}{\partial \xi} + \alpha^2 \tilde{c}_s^{\,2} \xi^{2-2/\alpha} \tau^{2\beta/\alpha} \frac{\partial^2}{\partial \xi^2} + \right.$$
$$\left. 2\mathrm{i}\tilde{\omega}_N \tilde{c}_s \frac{\partial}{\partial \tau} + 2\mathrm{i}\tilde{\omega}_N \tilde{c}_s \beta \tau^{-1} \xi \frac{\partial}{\partial \xi} \right] N = -\nu E_s^* E_p. \tag{A.36}$$

Next, we postulate

$$E_p = \tau^\gamma A_p(\xi), \qquad E_s = \tau^\delta A_s(\xi), \qquad N = \tau^\lambda B(\xi). \tag{A.37}$$

vi

Inserting the ansatz (A.37) into the three equations (A.34)-(A.36) we find

$$(1 - \tilde{c}_s)\, \alpha \xi^{1-1/\alpha} \tau^{\gamma+\beta/\alpha} \frac{\partial}{\partial \xi} A_p = -\, \mathrm{i}\tau^{\delta+\lambda} B A_s, \quad \text{(A.38)}$$

$$-(1 + \tilde{c}_s)\, \alpha \xi^{1-1/\alpha} \tau^{\delta+\beta/\alpha} \frac{\partial}{\partial \xi} A_s = -\, \mathrm{i}\tau^{\gamma+\lambda} B^* A_p, \quad \text{(A.39)}$$

$$\left[\alpha(\alpha-1)\, \tilde{c}_s{}^2 \xi^{1-2/\alpha} \tau^{\lambda+2\beta/\alpha} \frac{\partial}{\partial \xi} + \alpha^2 \tilde{c}_s{}^2 \xi^{2-2/\alpha} \tau^{\lambda+2\beta/\alpha} \frac{\partial^2}{\partial \xi^2} + \right.$$
$$\left. 2\mathrm{i}\tilde{\omega}_N \tilde{c}_s \lambda \tau^{\lambda-1} + 2\mathrm{i}\tilde{\omega}_N \tilde{c}_s \beta \tau^{\lambda-1} \xi \frac{\partial}{\partial \xi} \right] B = -\, \nu \tau^{\gamma+\delta} A_s^* A_p. \quad \text{(A.40)}$$

Since we want the τ dependence to vanish the exponents of τ all have to be the same, hence

$$\gamma + \frac{\beta}{\alpha} = \delta + \lambda, \quad \delta + \frac{\beta}{\alpha} = \gamma + \lambda, \quad \lambda + \frac{2\beta}{\alpha} = \lambda - 1, \quad \lambda + \frac{2\beta}{\alpha} = \gamma + \delta, \quad \text{(A.41)}$$

which has the solution $\gamma = \delta = -3/4$, $\lambda = -1/2$ and $\beta/\alpha = -1/2$. Without loss of generality we pick $\alpha = 1$ and therefore find $\beta = -1/2$. In summary, we find the system

$$(1 - \tilde{c}_s)\, \frac{\partial}{\partial \xi} A_p = -\mathrm{i}A_s B, \quad \text{(A.42)}$$

$$-(1 + \tilde{c}_s)\, \frac{\partial}{\partial \xi} A_s = -\mathrm{i}A_p B^*, \quad \text{(A.43)}$$

$$\left[\tilde{c}_s{}^2 \frac{\partial^2}{\partial \xi^2} - \mathrm{i}\tilde{\omega}_N \tilde{c}_s \left(1 + \xi \frac{\partial}{\partial \xi} \right) \right] B = -\nu A_s^* A_p, \quad \text{(A.44)}$$

in the variables $\xi = \zeta/\sqrt{\tau'}$ and $\tau = \tau'$.

(a) (b) (c)

(d) (e) (f)
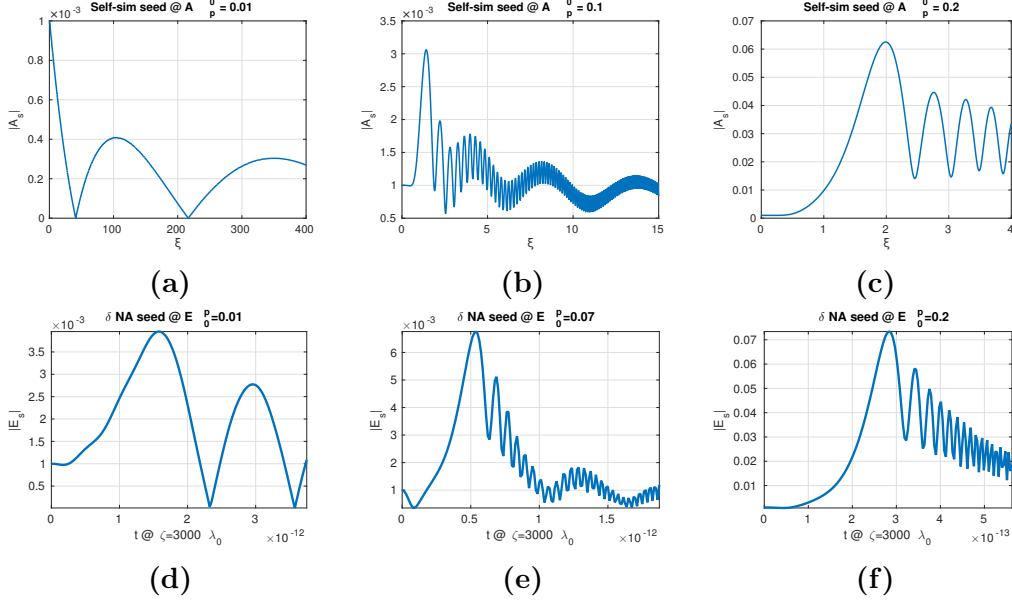
Figure A.1: Comparison between self-similar results (upper row) at given pump amplitude via solving Eqs. (A.42)-(A.44) to full $\delta N\mathbf{A}$ simulations (lower row) at corresponding pump strengths via solving the model (A.26)-(A.27). Note that the presented simulation results are obtained at a fixed $\zeta = 3000\lambda_0$, which is the seed's starting position, thus in the frame propagating with $\tilde{c}_s$ to the right. We mainly distinguish three different regimes: pure wc (A.1a and A.1d), mixed wc and sc (A.1b and A.1e) and pure sc (A.1c and A.1f). Parameters are $n = 0.3n_c$, $\tilde{c}_s \approx 1.5 \cdot 10^{-3}$, which corresponds to $T_e = 2$ keV and a detuning $\tilde{\omega}_N = 0.67\%\tilde{\omega}_p$, where $\tilde{\omega}_p$ is the dimensionless pump frequency.

Fig. A.1 stresses the capability of our self-similar model (A.42)-(A.44). We find the three different non-linear amplification regimes also found via simulating the $\delta N\mathbf{A}$ model (A.26)-(A.27) as explained in the figure.

However, so far we have chosen a rather arbitrary detuning of $\tilde{\omega}_N = 0.67\%\tilde{\omega}_p$ and notice heavy influence on the outcome. Additionally, the final seed amplitudes for both different approaches do not agree (see Fig. A.1). In conclusion we can say that we found qualitatively good agreement between the self-similar model and non-linear simulations. Results at least look very promising but of course demand further investigation.

Especially in comparison to other self-similarity models [55, 50, 92, 62], our result fails to predict growth of the seed peak amplitude over time. The attempts focusing on solely weak or strong coupling Brillouin amplification usually perform transformations into the co-moving frame of the seed. This way, δ directly depicts the maximum growth rate over time in the nonlinear regime. In case of strong coupling one finds $\delta = 3/4$, in case of weak coupling it is $\delta = 1$. However, since we

transform into the co-moving frame with the density wave, no such scaling can be found. This implies that our self-similar solution presented in this appendix lacks the predictive power of former solutions.

Danksagung

Hiermit möchte ich mich bei allen Personen bedanken, die mich auf meinem Weg hierher begleitet und unterstützt haben.

Historisch beginnen möchte ich mit meinem großen Bruder Jakob Schluck, ohne den ich vermutlich niemals Physik studiert, geschweige denn in der Oberstufe belegt hätte. Ich erinnere mich noch sehr gut, wie er in der Nacht vor der Abgabe meines Wahlzettels in mein Zimmer kam und mich beinah schon nötigte, der Physik nach einer leidvollen Erfahrung in der Mittelstufe noch eine Chance zu geben. Danke dafür, es wäre sonst wirklich schade gewesen! Aber nicht nur hier, sondern auch während des gesamten Abiturs, Studiums und schließlich der Promotion war er mir stets Ansprechpartner, Hinweisgeber, Freund und Bruder.

Weiterhin danke ich meinem kleinen Bruder Jonathan Schluck, der mich immer wieder hat erfahren lassen, was es heißt, Physik zu erklären, Stichwort Hebelgesetz. Vorallem neben der Arbeit, die so eine Promotion selbstverständlich mit sich bringt, hast Du mich in Deiner jugendlichen Leichtigkeit immer daran erinnert, dass das Leben ja meistens doch schön ist.

Schließlich danke ich meinen Eltern Ilse und Johannes Schluck, die mich während der gesamten Zeit sehr unterstützt haben. Zwar gilt das Physikstudium in unserer Familie immer noch eher als mysteriöser Fauxpas, aber sie haben trotzdem nie aufgehört, sich nach unserem Fortschritt zu erkundigen und uns zu helfen, wo es ihnen nur möglich war. Ohne euren Rückhalt wäre ich niemals so schnell so weit gekommen.

An dieser Stelle erinnere ich an meinen Großvater Willi Pohlmann, dem ich den Wunsch gern erfüllt hätte, dass er erlebt wie eins seiner Enkelkinder promoviert, doch dafür war ich leider zu langsam.

Ferner danke ich allen meinen mich unterstützenden Freunden rund um Lennart Caspers, aber insbesondere meiner Theatergruppe bestehend aus Maike Fickert, Maike Katthöfer, Isabel Egerland, Leonie Sieben-Prinz und Manuel Schulze. Ihr habt mir in meiner privat bisher schwersten Zeit neuen Mut gegeben, sodass ich die Promotion unbeschadet zu Ende führen konnte. Durch euch habe ich meine Liebe zum Schreiben und Spielen entdeckt, vielen Dank und auf viele gute Jahre.

Zur Universität Düsseldorf kommend danke ich zunächst Herrn Prof. Dr. Dr. Carsten Müller dafür, dass er mir ermöglicht hat, bei ihm zu promovieren. Aber nicht nur dafür, sondern auch für seinen steten Einsatz für Gerechtigkeit, sein Interesse an außeruniversitären Veranstaltungen und insbesondere seinen Vorschlag von mir bei der Studienstiftung des deutschen Volkes möchte ich mich herzlich bedanken. Ferner danke ich Herrn Prof. Dr. Karl-Heinz Spatschek für meine Betreuung im Institut für Theoretische Physik I seit der Bachelorarbeit, also

Eidesstattliche Versicherung

Ich versichere an Eides Statt, dass die Dissertation von mir selbständig und ohne unzulässige fremde Hilfe unter Beachtung der "Grundsätze zur Sicherung guter wissenschaftlicher Praxis an der Heinrich-Heine-Universität Düsseldorf" erstellt worden ist.

_____

Düsseldorf, den 20. Dezember 2016